# The Impact of B Site Disorder in the Manganites

By

**Kalpataru Pradhan**

**Harish-Chandra Research Institute, Allahabad**

A Thesis submitted to the
Board of Studies in Physical Science Discipline
In partial fulfilment of requirements
for the degree of
**DOCTOR OF PHILOSOPHY**
**of**
**Homi Bhabha National Institute**

July, 2009

# Certificate

This is to certify that the Ph.D. thesis titled "The Impact of B Site Disorder in the Manganites" submitted by Kalpataru Pradhan is a record of bona fide research work done under my supervision. It is further certified that the thesis represents independent work by the candidate and collaboration was necessitated by the nature and scope of the problems dealt with.

**Professor Pinaki Majumdar**
Thesis Advisor
Date:

# Declaration

This thesis is a presentation of my original research work. Whenever contributions of others are involved, every effort is made to indicate this clearly, with due reference to the literature and acknowledgment of collaborative research and discussions.

The work is original and has not been submitted earlier as a whole or in part for a degree or diploma at this or any other Institution or University.

This work was done under guidance of Professor Pinaki Majumdar, at Harish-Chandra Research Institute, Allahabad.

**Kalpataru Pradhan**
Ph.D. Candidate
Date:

**To My Friends...**

# Acknowledgments

I would like to thank my supervisor Prof. Pinaki Majumdar for his able guidance and support during my PhD at Harish-Chandra Research Institute. I have learnt immensely from him about physics as well as life.

I am very grateful to Prof. Prasenjit Sen for all that he taught me. Our collaboration was indeed a great opportunity and pleasure for me.

I would also like to acknowledge the insightful discussions I had with Prof. Sumathi Rao and Prof. Tribhuvan Prasad Pareek. I would like to thank the entire HRI community for making my stay enjoyble and memorable during my PhD.

I would like to acknowledge the use of the High Performance Scientific Computing facility at Harish-Chandra Research Institute.

I want to thank my parents and all my teachers who taught me during different stages of my education. I also thank to all my hostel mates during last 18 years of my hostel life and I learnt a lot from them.

I wish to thank my parents and siblings who has always encouraged me to continue my studies. Specially I would like to thank my younger brother Gyana Ranjan Pradhan.

Finally, I dedicate this work to all my friends around the world.

# Synopsis

In uncorrelated electron systems one requires substantial disorder, comparable to the Fermi energy, for nontrivial effects to emerge. For a dense electron system, with roughly one carrier per formula unit, this implies that the strength of the disorder needs to be $\mathcal{O}$(eV) for localisation effects, *etc*, to emerge. More physically, one would need a large 'impurity' concentration and a large mismatch between the host and impurity atoms for disorder to be relevant.

In correlated systems, however, the (bare) Fermi energy is not the only relevant scale in the problem. In heavy fermions, for example, the Kondo temperature sets the reference scale, while in polaronic systems the disorder needs to be comparable only to the (small) bandwidth of the heavy quasiparticles.

Disorder is recognised as a key player in the manganites. In the doped manganites, $A_{1-x}A'_xMnO_3$, 'A site' disorder seems to affect the physical properties through several mechanisms: (i) In a regime of possible phase separation, disorder, along with Coulomb interaction, promotes a cluster coexistence state. If the A site disorder is large the resulting state is just a nanoscale correlated glass. (ii) In the low bandwidth manganites, with large electron-phonon (EP) interaction, disorder promotes polaron formation, strongly enhancing the resistivity in the metallic state, and suppresses the ordering temperature.

While the effects above are interesting and 'large', they are not very surprising. They all involve suppression of the underlying ordered state. The impact of 'B site' (Mn site) dopants, *i.e*, materials of the form $A_{1-x}A'_xMn_{1-\eta}B_\eta O_3$, however, present several puzzles. For example, a low density of B dopants (a few %) can convert an insulator to a metal, or a metal to an insulator, simultaneously affecting the underlying magnetic state.

There are a variety of striking but apparently unconnected results on B doping in the manganites. For example, magnetic dopants like Cr, Co or Ni (but not Fe) on the Mn site in a $x = 0.5$ charge ordered insulating (CO-I) manganite promote a percolative ferromagnetic metal (FM-M), while non magnetic dopants of the same valence do not. The orbital ordered A type antiferromagnet (AF) at $x = 0$ is destabilised in favour of a ferromagnetic state by *both* magnetic and non magnetic dopants. In contrast to the cases above, where charge-orbital order is *suppressed*, doping Fe on a ferromagnetic metal at $x \sim 0.4$ *promotes* a charge ordered insulating state! This promotion of a competing ordered phase has no equivalent in the case of A site disorder. On spatial imaging most of these systems reveal phase separation (PS) and many of them also exhibit enormous magnetoresistance. The work in this thesis aims to uncover the organising principle behind these diverse effects, and suggest how B site disorder could be exploited as a tool for electronic phase control.

The thesis starts with an introduction to correlated electron systems and moves on to a detailed discussion of the experimental results on the effect of disorder in the manganites. We discuss both A and B site disorder, but the focus is mainly on B site doping, classifying the wide variety of results in terms of the reference manganite state and the valence and magnetic character of the dopant.

This is followed by a discussion of our results on the impact of weak homogeneous (A site) disorder and strong dilute (B site) scattering on the $x = 0.5$ CE charge ordered manganites. This requires a suitable 'reference' model for the clean manganite - involving $e_g$ electron hopping, Hunds and Jahn-Teller coupling, and weak antiferromagnetic superexchange between the Mn $t_{2g}$ spins. The modelling of B site disorder in this effort is crude, incorporating only a strong repulsive potential, but leads to results which capture (one family of) key experimental effects, including the percolative metallisation of the CE insulator.

The next chapter introduces a more 'realistic' but still minimal model of B dopants in the manganites. The impurities are modelled in terms of their valence in the manganite, the position of the impurity level with respect to the manganese $e_g$ levels, and the exchange and hopping interactions between the dopant and neighbouring Mn atoms. The principal parameters in the problem are hole doping $(x)$, the manganite bandwidth (mimicked by the ratio of hopping and Jahn-Teller coupling in our theory), and the impurity valence $(\alpha)$ and concentration $(\eta)$. The impurity potential $(V)$ and exchange coupling $(J')$ to Mn (for magnetic dopants) are also relevant in some cases.

The problem above includes multiple strong couplings in the reference manganite model, to capture the phase competition, and the presence of dilute strong scatterers on some Mn sites. The clean phases at $T = 0$ can be approximately captured by variational calculations but the impact of disorder, and thermal fluctuations, can only be accessed numerically. We use the 'travelling cluster' (TCA) variant of exact diagonalisation based Monte Carlo to solve this problem.

Our results are described in two chapters, the first focusing on situations where valence change on Mn due to B impurities is the key effect, while the second studies the impact of magnetic dopants. Our principal results are the following: **(i)** We discover that the following hierarchy of effects arise in all B doping cases: (a) change of the effective valence on the Mn sites, (b) percolation of the metallic phase through impurity free regions, and (c) 'reconstruction' of the background magnetism and charge order by magnetic dopants. **(ii)** By exploring the prominent manganite states, and different B dopants, we are able to explain most of the outstanding experimental results. **(iii)** Since the remarkable effect of B dopants arise from phase competition in the underlying magnetic model, we are able to suggest new experiments to test out unexplored insulator-metal transitions driven by B dopants. **(iv)** We also demonstrate how B impurity locations determine the percolation pattern and may allow atomic level control of current paths in a material.

The final chapter of the thesis is not related to manganites but concerns another family of metallic magnets. We studied the Kondo lattice model, with large S spins, across the whole coupling range - from the perturbative RKKY end to the strong coupling double exchange limit. It allows us to trace the evolution of magnetic order from spiral states at weak coupling, dictated by the free electron susceptibility $\chi_0(\mathbf{q})$, to the double exchange ferromagnet. In addition to solving this model completely, using a combination of variational and Monte Carlo techniques, we wanted to revisit the classic problem of $4f$ magnetism. These have been traditionally interpreted within a RKKY scheme, with small variations in electronic structure held responsible for the wide variation in magnetic order across the family. We demonstrated how *both* electronic structure and coupling effects *beyond RKKY*, arising from the increasing exchange scale across the $4f$ family, control the magnetism in these materials.

# Publications and preprints

1. Distinct Effects of Homogeneous Weak Disorder and Dilute Strong Scatterers on Phase Competition in the Manganites (*).
   K. Pradhan, A. Mukherjee, and P. Majumdar,
   Phys. Rev. Lett. **99**, 147206 (2007).

2. Exploiting B Site Disorder for Electronic Phase Control in the Manganites (*).
   K. Pradhan, A. Mukherjee and P. Majumdar,
   Europhys. Lett. **84**, 37007 (2008).

3. Magnetic order Beyond RKKY in the Classical Kondo Lattice (*).
   K. Pradhan and P. Majumdar,
   Europhys. Lett. **85**, 37007 (2009).

4. The Effects of B site Doping on the Manganites (*).
   K. Pradhan and P. Majumdar,
   Preprint (2009)

5. Conductance Switching and Inhomogeneous Field Melting in the Charge Ordered Manganites.
   A. Mukherjee, K. Pradhan and P. Majumdar,
   Europhys. Lett. **85**, 27003 (2009).

6. First Principles Study of Sc, Ti and V Doped $\mathrm{Na}_n$(n =4, 5, 6) Clusters: Enhanced Magnetic Moments.
   K. Pradhan, P. Sen, J. U. Reveles, S. N. Khanna,
   Phys. Rev. **B 77**, 045408 (2008).

7. First-Principles Study of $\mathrm{TMNa}_n$(TM= Cr, Mn, Fe, Co, Ni; n = 4-7) Clusters.
   K. Pradhan, P. Sen, J. U. Reveles, S. N. Khanna,
   J. Phys. Condens. Matter **20**, 255243 (2008).

8. Designer Magnetic Superatoms.
   J. U. Reveles, P. A. Clayborne, A. C. Reber, S. N. Khanna, K. Pradhan, P. Sen, and M. R. Pederson,
   Nature Chemistry **1**, 310 (2009).

9. $Si_xC_{1-x}O_2$ *alloys*: A possible route to stabilize carbon-based silica-like solids?
   A. Aravindh *et al.*(JNCASR Summer School, India, 2006),
   Solid State Comm. **144**, 273 (2007).

Some of the material related to the starred (*) papers is discussed in the thesis.

# Contents

# Chapter 1

# Introduction

The investigation of strongly correlated electron systems, involving 3d or 4f elements, is one of the most challenging branches of solid state physics. The interaction between electrons, or between electrons and phonons, or electrons and local moments, leads to a 'correlated' state. Electronic correlations can cause striking many body effects like localisation via the Mott transition, the formation of a heavy electron state, charge and orbital ordering, *etc*. Many of the most interesting condensed matter systems, *e.g*, the cuprate superconductors, the colossal magnetoresistance manganites, the cobaltates, and other oxides fall in this category.

While there are several issues of interest in the context of correlated systems, *e.g*, the Mott transition, or the emergence of non Fermi liquid behaviour, we will focus mainly on 'phase competition' in this thesis. Broadly, this relates to the presence of several ordered phases in proximity in the phase diagram of a material, and one can tune from one phase to another via small changes in doping, or application of pressure, or an external field. The phase competition often creates phase separation tendencies in the material and can lead to the formation of nanoscale clusters of competing phases in the presence of disorder. Since there are excellent reviews [1, 2, 3, 4] of the general properties of correlated systems, let us specialize to the manganese based transition metal oxides (TMO) [5, 6, 7].

TMO's having perovskite ($ABO_3$) structure are important both in terms of fundamental physics and possible technological applications. Mn forms a perovskite with a rare earth element A (and/or an alkaline earth element A') along with oxygen. These materials, of the form $A_{1-x}A'_xMnO_3$, are called manganites. In the $ABO_3$ structure both A and A′ are present in the 'A site' and Mn is in the 'B site'. The A site ions in our discussion will be rare earths (RE) or alkaline earths (AE), while the B site will be Mn or its substitutions.

The manganites were re-discovered in the 90's based on the observation of 'colossal magnetoresistance' (CMR), *i.e*, a large response $[\rho(0) - \rho(h)]/\rho(0)$, where $\rho(h)$ is the resistivity in a magnetic field $h$ [8]. Manganites have not quite realised their promise as CMR based data storage materials and that field is dominated by the giant magnetoresistance (GMR) materials [9, 10], which have a more modest but practically useful field response. While there is continuing effort in developing device applications based on the manganites, our focus here will be on a basic physics issue: the manipulation of the electronic phases in the manganites using B site disorder as a tool.

## 1.1 Introduction to the manganites

The history of the manganites goes back to 1950 [11, 12] when Jonker and van Santen carried out early work on the compound $La_{1-x}A'_xMnO_3$ with A′=Ca, Sr, and Ba. They found the material to be an antiferromagnetic insulator at both the endpoints, $x = 0$ and $x = 1$. However, for a wide range of intermediate $x$ the material was ferromagnetic. Around $x = 0.3$, they found that the onset of ferromagnetism is associated with a sharp decrease in resistivity. A 'double exchange' (DE) model [13] was proposed by Zener to explain the link between the resistivity and the ferromagnetic ordering in $La_{1-x}A'_xMnO_3$. The magnetoresistance was reported by Volger [14] in 1954. He observed a notable decrease of resistivity in $La_{0.8}A'_{0.2}MnO_3$ in the ferromagnetic state in presence external applied field. In 1994, the CMR effect was discovered [8] in $La_{1-x}Ca_xMnO_3$ at $x$ = 0.33 by Jin and coworkers, just a year after large MR was reported in $La_{1-x}Ba_xMnO_3$ [15]. Jin *et al.* reported MR $(\rho(0) - \rho(h))/\rho(0)$ close to 94% at 200K and over 99.9% at 77K for thin films of $La_{0.67}Ca_{0.33}MnO_3$. One year later Xiong *et al.* [16] reported MR of over 99.9% using thin films of $Nd_{0.7}Sr_{0.3}MnO_3$ near 60K in a magnetic field of 8 Tesla. These results involving huge changes in resistivity, shown in Fig-1.1, suggested that the manganites were a potential alternative to GMR systems.

The initial results were in qualitative agreement with Zener's original double exchange model, but the transition temperatures ($T_c$) seen were an order of magnitude

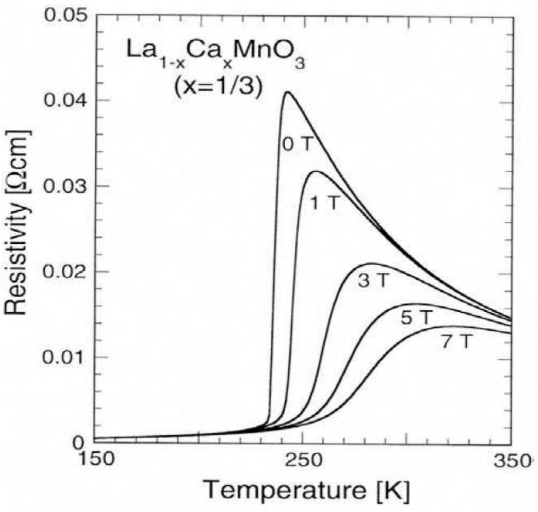

Figure 1.1: Colossal magnetoresistance (CMR) behaviour for the $La_{0.67}Ca_{0.33}MnO_3$ single crystal. From Y. Tokura, Rep. Prog. Phys., **69**, 797 (2006).

below the theoretical estimate by Millis *et al.* [17]. The $T_c$ of $La_{1-x}Sr_xMnO_3$ at $x = 0.175$ is $\sim$ 250K [18], whereas the theoretical estimate of $T_c$ by Millis *et al.* using double exchange exceeds 1000 K. In addition, the DE model also fails to explain the resistivity in the more insulating manganites, as well as the wide variety of observed phases [7, 17].

### 1.1.1 Crystal structure

The structure of $AMnO_3$ (A = RE ions) is almost a cubic perovskite. The arrangement of atoms in the perovskite structure of manganites is shown in Fig-1.2. The space lattice is simple cubic. The basis consists of one A ion at (0,0,0), Mn ion at (1/2,1/2,1/2), and three O ions at (0,1/2,1/2), (1/2,0,1/2), and (1/2,1/2,0). The structure is stabilized by the 12-fold and 6-fold oxygen coordination of the A ions and Mn ions respectively. A is of fixed valence $3+$ and O is of valence $2-$. So the charge neutrality condition forces Mn to be in a $3+$ valence state. When an A′ ion (A′=AE) in a $2+$ valence state is doped in place of A, the charge neutrality condition leads to a mixed valent state of Mn, *i.e.* an ionic configuration of the form $A^{3+}_{1-x}A'^{2+}_{x}Mn^{3+}_{1-x}Mn^{4+}_{x}O^{2-}_{3}$. We should of course not imagine individual Mn to be in fixed $3+$ or $4+$ valence states but rather in a valence fluctuating state.

The structure can also be visualized as stacking of two planes, namely the AO and $MnO_2$, one over the other. For an ideal cubic structure the face diagonal, A-O-A, equals

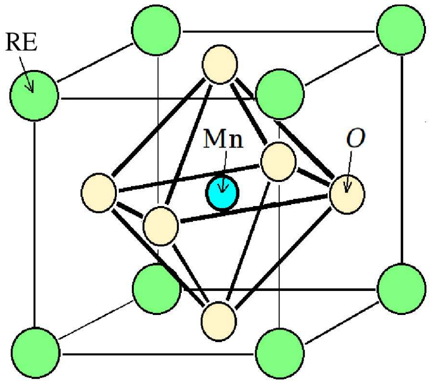

Figure 1.2: The perovskite structure of $AMnO_3$ where A are RE ions.

$\sqrt{2}$ times the cube edge, O-B-O, i.e. $2r_A + 2r_O = \sqrt{2}(2r_{Mn} + 2r_O)$ where $r_A$ denotes the radius of the A ion, $r_{Mn}$ and $r_O$ are the radii of Mn and O ions respectively. However in the doped case $r_A$ denotes the (weighted) average radius of A and A′. The tolerance factor $t_f$, which is 1 for ideal cubic structure, is defined as [19]

$$t_f = \frac{d_{A-O}}{\sqrt{2}d_{Mn-O}} = \frac{r_A + r_O}{\sqrt{2}(r_{Mn} + r_O)}$$

Here $r_A$ is the average radius of A and A′ ions. The shortest distance between A-O ($d_{A-O}$) and Mn-O ($d_{Mn-O}$) are calculated from the sum of the ionic radii for 12 coordinated A site cations and 6 coordinated Mn ions [20]. The tolerance factor $t_f$ governs the manganites structure and is affected by the ionic radius of A and A′. The cubic structure is stable for $0.89 < t_f < 1.02$. Large deviations from unity result in completely different crystal structures like hexagonal, orthorhombic, etc. The perfect cubic structure occurs if the average radius at the A site is 1.48Å. In practice, the A site ions are smaller (see Table-1.1), leading to a rotation of the $MnO_6$ octahedra. The value of $r_A$ in the $La_{1-x}Ca_xMnO_3$ (LCMO) is less then the ideal value 1.48Å, and the $MnO_6$ octahedra rotate or distort to improve the packing. The true unit cell is an orthorhombic Pnma cell [21]. The change in structure, either by lengthening or bending the Mn-O-Mn bond, affects the electronic properties and we will discuss this later.

In the perovskite structure, the Mn atom is at the center of an octahedron defined by 6 neighbouring oxygen atoms. The different Mn orbitals have different shapes, and thus interact with the surrounding oxygen atoms differently. The five fold degenerate 3d-orbitals of the (free) Mn atom splits into two sets due to the crystal field. The level with lower energy includes the $d_{xy}$, $d_{yz}$, and $d_{zx}$ orbitals, while the higher one includes

| **RE ions** | **Radius** | **AE ions** | **Radius** |
|---|---|---|---|
| $La^{3+}$ | 1.36 | $Ca^{2+}$ | 1.34 |
| $Pr^{3+}$ | 1.29 | $Sr^{2+}$ | 1.44 |
| $Nd^{3+}$ | 1.27 | $Ba^{2+}$ | 1.61 |
| $Sm^{3+}$ | 1.24 | **Mn ions** | |
| $Eu^{3+}$ | 1.23 | $Mn^{3+}$ | 0.645 |
| $Gd^{3+}$ | 1.21 | $Mn^{4+}$ | 0.530 |
| $Tb^{3+}$ | 1.20 | **O ion** | |
| $Dy^{3+}$ | 1.18 | $O^{2-}$ | 1.40 |
| $Y^{3+}$ | 1.18 | | |

Table 1.1: Ionic radii (in Angstroms) for elements involved in the perovskite structure of manganites (From Y. Tokura, Rep. Prog. Phys., **69**, 797 (2006).

the $d_{x^2-y^2}$ and $d_{3z^2-r^2}$ orbitals. The triplet is referred as the $t_{2g}$ and the doublet as $e_g$. The $t_{2g}$ levels are about 1eV lower than the $e_g$ orbitals [5, 7]. The schematic in Fig-1.3 shows the spin and charge degrees of freedom of the Mn atom in the crystalline environment. Let us discuss these one by one.

**(i) Charge**

Atomic Mn is in a $3d^5 4s^2$ state, so Mn$^{3+}$ is $3d^4$ while Mn$^{4+}$ is $3d^3$. The large crystal field splitting favours the population of the $t_{2g}$ levels with three electrons forming an electrically inactive spin $S$ of magnitude 3/2, and electron occupancy in each $e_g$ level is either 0 or 1. The electronic structure of the Mn$^{3+}$ ion is thus $t_{2g}^3 e_g^1$, and for the Mn$^{4+}$ ion it is $t_{2g}^3 e_g^0$. We will consider that Mn$^{3+}$ ion has 'charge' 1 and Mn$^{4+}$ ion has 'charge' 0. The ratio of Mn$^{3+}$ to Mn$^{4+}$ decides the conduction electron density in the manganites.

In the parent manganites A$^{3+}$Mn$^{3+}$O$_3^{2-}$, all Mn ions are in 3+ state and the electron density is 1. When AE ions are doped in place of RE we have $\mathrm{A}^{3+}_{1-x}\mathrm{A}'^{2+}_x\mathrm{Mn}^{3+}_{1-x}\mathrm{Mn}^{4+}_x\mathrm{O}^{2-}_3$, *i.e*, the density of Mn$^{4+}$ increases, and the electron density decreases (the hole density increases). Doping AE ions in place of RE will control the hole density, and also introduce some disorder.

**(ii) Spin**

The large spin, $S = 3/2$, arises from the electrons in the $t_{2g}$ level. It is reasonable to treat the three spin-polarized $t_{2g}$ electrons as a localised core spin, since the overlap integral between $t_{2g}$ and oxygen $p\sigma$ orbital is small compared to that between $e_g$ and $p\sigma$ orbitals. Due to the large value of the total spin $S$, the localised spin is usually approx-

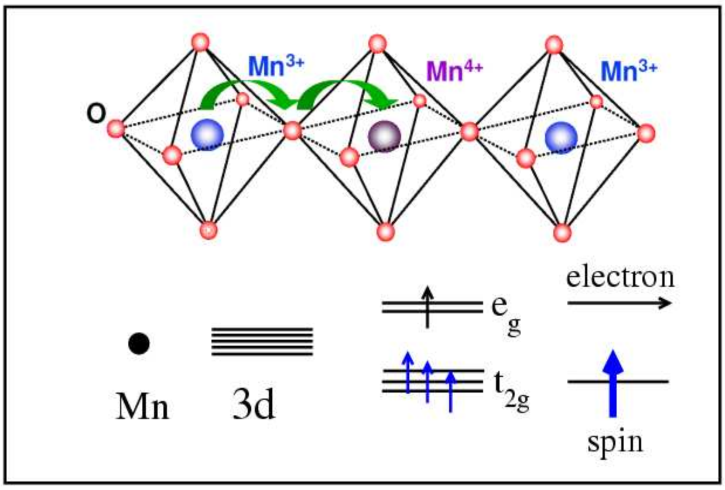

Figure 1.3: A schematic showing the relative energies of the Mn 3d orbitals (i) Mn ion (ii) 3d orbital of Mn ion in isolation, (iii) splitting due to the presence $O_6$ octahedral environment, and (iv) $e_g$ electron as mobile electron and $t_{2g}$ electrons as spin.

imated by a classical vector. The ordering of these spins leads to different magnetic structures found in the manganites. The charge sector ($e_g$ electron) is strongly coupled to the core spin due to the large Hunds coupling, and the spin of the $e_g$ electron is always parallel to the orientation of the local core spin.

Neighbouring core spins interact with each other via double exchange (DE), mediated by the $e_g$ electrons, and an antiferromagnetic superexchange (SE). Both the DE and SE interaction between localised spins is via the bridging oxygen atom. We will discuss the DE and SE interaction in detail in the next section.

**(iii) Orbital**

The degeneracy of the $e_g$ state (or $t_{2g}$) is likely to lift when the $MnO_6$ octahedron undergoes a Jahn-Teller distortion. The Jahn-Teller [22] distortion is energetically favourable if the $e_g$ (or $t_{2g}$) level is partially filled. The $e_g$ state in $Mn^{3+}$ is singly occupied and splits into two due to Jahn-Teller distortion as shown in Fig-1.4. The distorted oxygen configuration energetically prefers one $e_g$ combination compared to the other. The $e_g$ state of $Mn^{4+}$ is empty and free from any distortion. The triplet $t_{2g}$ state also splits into two levels due to the distortion. However, as long as the crystal field splitting is large, the degeneracy lifting in $t_{2g}$ is not important and we can continue to treat them as $S = 3/2$ core spins.

Overall, the Mn ion which has five $3d$ orbitals gives rise to charge, spin, and orbital

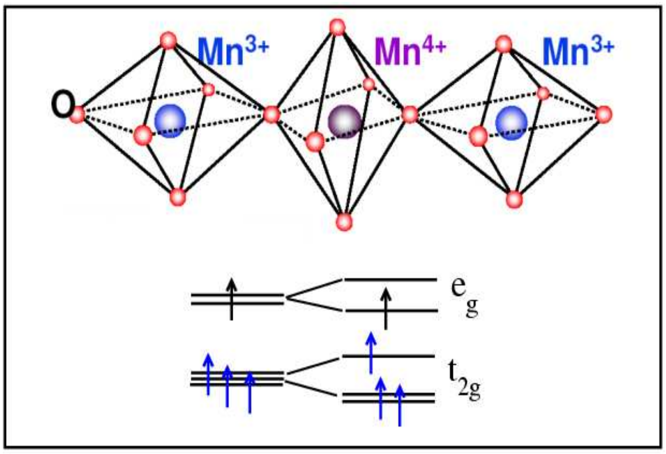

Figure 1.4: A schematic diagram showing the relative energies of the Mn 3d orbitals without and with Jahn-Teller distortion.

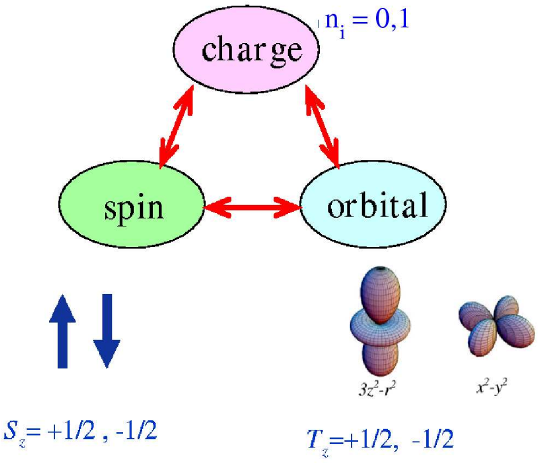

Figure 1.5: The interconnected charge, spin, and orbital degrees of freedom in the manganites.

degrees of freedom because of crystal field effects, Hunds coupling, and Jahn-Teller distortion. A schematic summarizing the interconnection is shown in Fig-1.5.

### 1.1.2 Magnetic interactions

The direct overlap between the atomic Mn orbitals is small and the magnetic interaction is mediated by intervening oxygen 2p electrons. The magnetic properties of the manganites are largely determined by the transfer of electrons between manganese and oxygen orbitals that point towards each other. There are two important interactions, namely double exchange and superexchange.

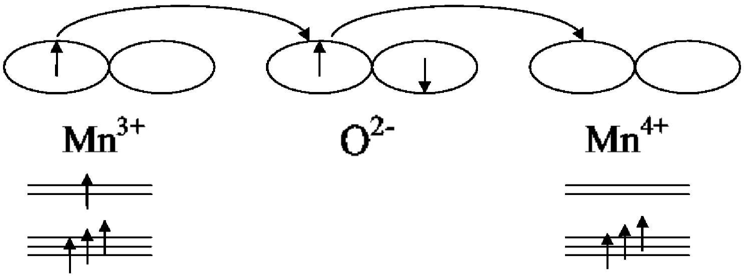

Figure 1.6: A schematic of the double exchange mechanism showing the simultaneous transfer of electrons between the adjacent Mn ions in the presence of an oxygen ion.

### (i) Double exchange

The double exchange mechanism was first postulated by Zener [13] to explain the simultaneous change in electrical resistivity and magnetic ordering in LCMO at $x = 0.30$. According to the Zener model, $e_g$ electron of the Mn ion transfer to one of the 2p orbitals of oxygen and simultaneously the same 2p orbital transfers its electron to the adjacent Mn ion. In this way the 2p occupancy is unchanged, one electron is just replaced by another, but an $e_g$ electron is able to move from one Mn to another. This process depends on the orientation of two neighbouring Mn core spins and their $e_g$ occupancy. If the $e_g$ orbitals in both the Mn ions are occupied then electron transfer is not possible due to Pauli exclusion principle. There is effective interaction between two Mn ions if and only if one of the Mn sites participating in the process has no $e_g$ electron.

Originally, Zener considered the explicit movement of electrons schematically as shown in Fig-1.6 and written as $\mathrm{Mn}^{3+}_{1\uparrow}\mathrm{O}_{2\uparrow,3\downarrow}\mathrm{Mn}^{4+} \rightarrow \mathrm{Mn}^{4+}\mathrm{O}_{1\uparrow,3\downarrow}\mathrm{Mn}^{3+}_{2\uparrow}$ where 1, 2, and 3 label electrons that belong either to the oxygen, or to the $e_g$ level of the Mn ions. In this case there is 'simultaneous' motion involving electron 2 moving from the oxygen to the right Mn ion, and electron 1 from the left Mn ion to the oxygen. This oxygen mediated simultaneous process was called "double exchange".

Further work was performed by Anderson and Hasegawa [23] and de Gennes [24] to visualize the DE processes and it was presented as a second-order process rather than simultaneous process. In this case the two states described above go from one to the other using an intermediate state $\mathrm{Mn}^{3+}_{1\uparrow}\mathrm{O}_{3\downarrow}\ \mathrm{Mn}^{3+}_{2\uparrow}$. In this context the effective hopping for the electron to move from one Mn site to the next is proportional to the square of the

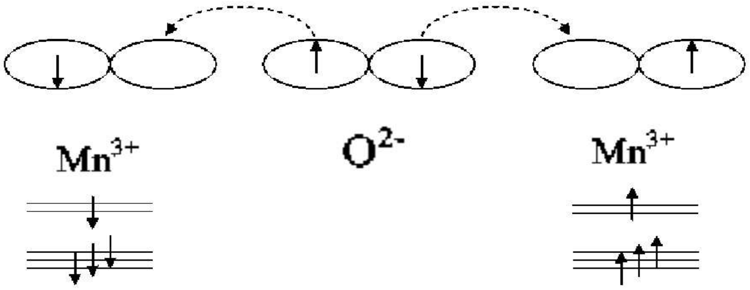

Figure 1.7: A schematic diagram of the superexchange mechanism showing the virtual transfer of electrons between the adjacent Mn ions in presence of oxygen ion. The dashed arrows represent the virtual transfer of the electron between these orbitals. This means that the electron is located on the oxygen ion for the majority of the time, but can be found in the manganese orbital indicated by the arrow.

hopping involving the $p$-oxygen and $d$-manganese orbitals. The effective hopping ($t_{ij}$) is proportional to $cos(\theta_{ij}/2)$, as shown by Anderson and Hasegawa when the localised spins are considered classical. Here $\theta_{ij}$ is angle between the nearest neighbour spins. The hopping, $t_{ij}$ is the largest when $\theta_{ij} = 0$ and vanishes for antiparallel spins. Ferromagnetic alignment maximizes the hopping term, facilitating electron motion from site to site to gain kinetic energy.

The gain in the kinetic energy is related to the decrease in resistivity. Therefore, ferromagnetism and metallicity are linked as seen in experiments and simple DE is able to explain the trend. However, DE overestimates the $T_c$ [17] and fails to explain the large change in resistivity near the $T_c$ in La$_{1-x}$Sr$_x$MnO$_3$.

**(ii) Superexchange**

The superexchange (SE) interaction between Mn ions is also mediated by an intermediate oxygen ion. The detailed mechanism, however, is quite different. One electron of the full filled 2p orbital of O ion virtually hops to the neighbouring Mn. It spends part of the time in Mn ion as shown in Fig-1.7 and constitute SE interaction between Mn spins. Antiferromagnetic superexchange interaction between the Mn spins are essential to explain the antiferromagnetic phase in highly doped manganites like CaMnO$_3$ where double exchange is absent due to the absence of carriers.

### 1.1.3 Electron-phonon interaction

The inability of the double exchange model to explain the magnitude of CMR and the transition temperature [17] was the main reason to investigate the importance of electron-phonon coupling in the manganites. Millis *et al.* suggested lattice polaron effects due to a strong electron-phonon interaction as a necessary ingredient of manganites physics [25]. Later it was experimentally shown that in the prototype $La_{0.7}Ca_{0.3}MnO_3$ (LCMO) system, there is formation of static nanoscale lattice polarons above transition temperature [26].

We have stated that the double degeneracy of the $e_g$ orbitals is lifted by the Jahn-Teller (JT) distortion of the $MnO_6$ octahedron [22]. Let us clarify this key effect. The basic formalism for the study of electrons coupled to Jahn-Teller modes was set up by Kanamori during 1960 [27]. The electronic orbitals are degenerate in the undistorted crystal structure, as Mn is in an octahedron of oxygens. This structure is generally unstable and the Jahn-Teller effect creates a distortion towards a lower symmetry ionic arrangement.

The distortion of the $MnO_6$ octahedron is cooperative. Once it occurs in a particular octahedron, it will affect the neighbours. The large JT effect in presence of the $e_g$ electron lowers the electronic energy and helps in 'binding' the mobile electron to an Mn ion. The distortion of the Mn octahedron is largest at $x = 0$, but is visible as a structural distortion almost upto $x = 0.20$ [28].

## 1.2 Typical phases in the manganites

The manganites have a rich variety of phases which show up on increasing the doping on the parent $x = 0$ state. The main phases we are interested in are the CE charge-orbital ordered insulator (CE-CO-OO-I), and the ferromagnetic metal (FM-M). Several magnetic configurations that occur in the manganites are shown in Fig-1.8.

**(i) The CE charge ordered phase**

The CE-CO-OO-I phase is found at half filling, $x = 0.50$. CE stands for 'charge-exchange' and involves zigzag ferromagnetic chains that we show later. For this doping, there are as many $Mn^{3+}$ as $Mn^{4+}$ ions, and the charge order is in the form of a checkerboard of (nominally) $Mn^{3+}$ and $Mn^{4+}$. The CE phase found in all manganites

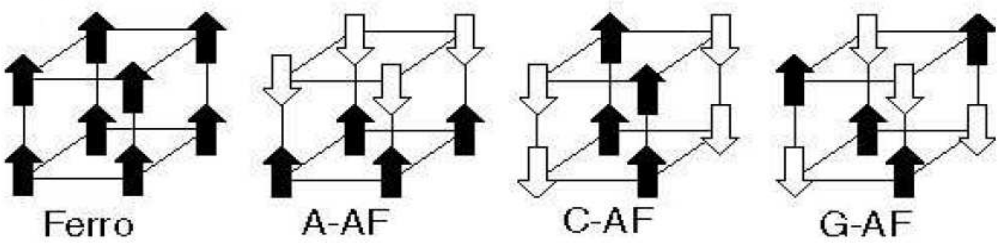

Figure 1.8: Four types of spin arrangement in the manganites. The other important phase introduced later is the CE phase.

are charge ordered but occurrence of CE magnetic order does not necessarily require charge order.

$Mn^{3+}$ sites have orbital order due to large electron occupancy while the orbital degree of freedom is inactive in $Mn^{4+}$. Orbitals of $Mn^{3+}$ are directed toward $Mn^{4+}$ when the two ions are ferromagnetically coupled, and they are directed away from $Mn^{4+}$ when the two ions are antiferromagnetically coupled. As a result, the $d_{3x^2-r^2}$ and $d_{3y^2-r^2}$ orbitals order in CE type antiferromagnetic structure, composed of ferromagnetic zig-zag chains, antiferromagnetically coupled to each other within the (a,b) planes. A two dimensional schematic of the CE-CO-OO-I phase is shown in Fig-1.9. Between the planes, not shown in the figure, the spins are coupled antiferromagnetically. Electrons can hop along the zigzag chains as spins are coupled ferromagnetically. Although the electrons can delocalise on the zigzag chains, the overall system is insulating.

**(ii) Ferromagnetic metal**

For a certain range of doping, like in $La_{1-x}Sr_xMnO_3$ (LSMO), the manganites show a large decrease in resistivity upon cooling, associated with the paramagnetic (PM) to ferromagnetic (FM) transition. Close to $T_c$ the resistivity can be further strongly reduced by applying a magnetic field - the phenomenon of colossal magnetoresistance. The temperature dependent resistivity in the FM phase has been qualitatively explained by the double exchange (DE) mechanism. The DE explanation is discussed as follows: the FM phase, for example in LSMO, involves mixed valence $Mn^{3+}$ and $Mn^{4+}$. There are $(1-x)$ $e_g$ electrons per unit cell, which are free to move through the crystal, subject to a strong Hunds coupling to the localised spins. The kinetic energy

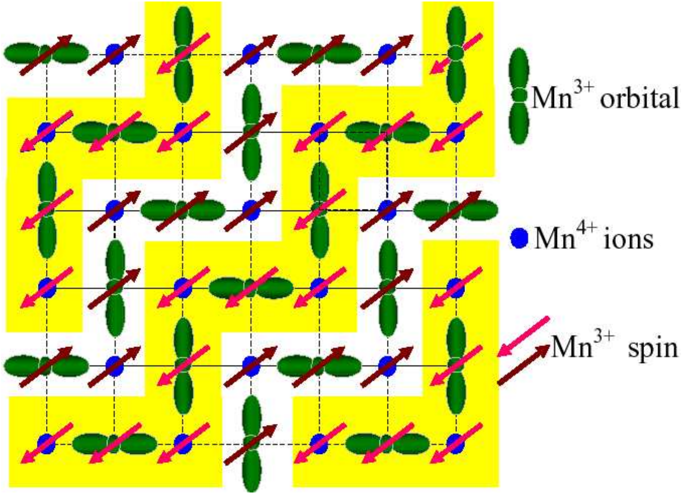

Figure 1.9: Schematic diagram of CE-CO-OO-I phase in half doped manganites. The lobes indicate the direction of e$_g$ orbitals while the spin directions of Mn site are denoted by arrows. Spins are ferromagnetic on the zigzag path indicated by colour contrast.

is minimized by making all the spins parallel. The largest $T_c$ in the double exchange model is around 0.1t, where $t$ is the hopping amplitude, and occurs at half-doping. DE ferromagnetism vanishes for an empty lattice as well as a full band. The temperature dependent resistivity shows metallic behaviour at both low and high ($T > T_c$) temperature. There is no metal-insulator transition associated with $T_c$.

To complete the discussion on the various phases found in manganites we have shown a $x$-T phase diagram for $Nd_{1-x}Sr_xMnO_3$ in Fig-1.10. Below we quickly discuss some other phases that appear in the phase digram. Orbital orders for different configurations of Mn spins are also shown schematically in the same figure and we refer to those orbital order while discussing various phases.

*Insulating A-type antiferromagnet*: For $x = 0$, all manganese ions are $Mn^{3+}$, and the structure is distorted by cooperative Jahn-Teller effects. The $d_{3x^2-r^2}$ and $d_{3y^2-r^2}$ orbitals order in the (x,y) plane, yielding a ferromagnetic coupling in this plane, while they are directed away from each other in the z direction, yielding an antiferromagnetic coupling. This results in a layered antiferromagnetic state, denoted as A type. The electrons are localised on the $Mn^{3+}$ sites, and the phase is insulating.

*Canted Antiferromagnet Insulator*: When some $Mn^{4+}$ replace $Mn^{3+}$ ions in a small fraction ($0 < x < 0.1$), the orbital ordering is not seriously perturbed and the state

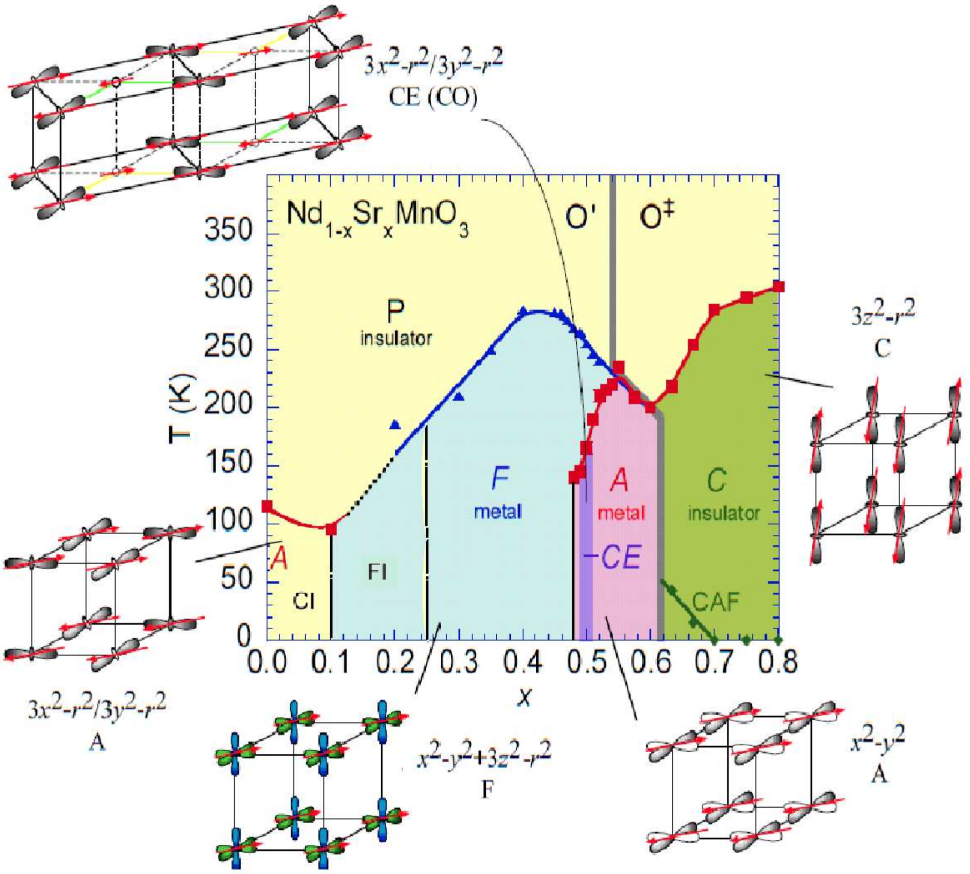

Figure 1.10: Phase diagram of $Nd_{1-x}Sr_xMnO_3$. F denotes a ferromagnetic state. A, CE, C and G denote A-type, CE-type, C-type and G-type antiferromagnetic states, respectively. FI and CI denote ferromagnetic insulator and canted antiferromagnetic insulator. Schematic views of the orbital and spin configurations on Mn sites for the respective phases also shown. The arrows represent the direction of spin, and the lobes show the $e_g$ orbital. From Y. Tokura, Rep. Prog. Phys. **69**, 797 (2006).

remains insulating. However, the spin angle between the ferromagnetic planes (of A-type phase) decreases from $\pi$ and we get a canted A-type antiferromagnetic.

*Ferromagnetic insulator*: When $x$ increases from 0.1, a ferromagnetic insulator (FI) phase appears. As $x$ increases, the percentage of $Mn^{4+}$ ions increases and leads to some empty $e_g$ orbitals which allows the electrons to have some degree of mobility. A-type AFM is layered FM planes coupled antiferromagnetically and due to finite electron hopping regions of these ferromagnetic planes start aligning in the same direction to gain kinetic energy from the DE interaction.

The charge and/or orbital ordered state in $La_{1-x}Sr_xMnO_3$ has been observed by (resonant) x-ray scattering [29] and neutron scattering [30]. To explain the insulating state it is important to take lattice distortions, which are present up to some finite doping [28], into account. These distortions localise electrons leading to an insulating phase although it is ferromagnetic in nature.

*Metallic A-type antiferromagnet*: With further reduction in the electron count (in the range $0.5 < x < 0.625$), the ferromagnetic interaction is weakened. In this case, the c axis (along z) is compressed and becomes smaller than a and b (x,y), and the $d_{x^2-y^2}$ orbitals order is favorable. The hopping of electrons is still possible within each (x,y) plane, but not perpendicular to the plane, due to the shape of $d_{x^2-y^2}$ orbitals, which lack overlap along the z direction. The state is thus metallic, but highly anisotropic and quasi two dimensional.

*Insulating C-type antiferromagnet*: As $x$ is increased beyond 0.625, C-type antiferromagnetic ordering appears, in which the $d_{3z^2-r^2}$ order. It corresponds to an elongation of the orbital in the z-axis. The hopping of electrons in z-axis is possible and ferromagnetic in the z direction while antiferromagnetic in x and y direction. The resulting state is insulating.

*Insulating G-type antiferromagnet*: Beyond the C-type AFM (not shown in the figure), the orbital ordering is disappearing with the $Mn^{3+}$ ions, and the $Mn^{4+}$ are antiferromagnetically coupled to their $Mn^{4+}$ neighbours, in a so-called G-type antiferromagnetic arrangement. The remaining $Mn^{3+}$ couple ferromagnetically to the $Mn^{4+}$, but the associated electrons can not migrate freely through the lattice, and the state is insulating. In the $x = 1$ limit, all $Mn^{4+}$ are antiferromagnetically coupled to their neighbouring $Mn^{4+}$.

## 1.3 Bandwidth variation

Various complex phases are visible in the manganites when we vary the hole density from $0 - 1$. In Fig-1.10 we have shown different phases for $Nd_{1-x}Sr_xMnO_3$. Let us examine what happen when we dope Ba or Sr in place of La. The bandwidth (BW) varies when we dope different A′ ions in the parent material. The BW dependence of the manganites phases can be roughly predicted based on our knowledge of the interactions at play. The tolerance factor $t_f$, related to $r_A$, is a measure of the bandwidth in these materials. The tolerance factor (defined in section 1.1) and the bandwidth, BW are defined as

$$\begin{aligned} t_f &= \frac{r_A + r_O}{\sqrt{2}(d_{Mn-O})}, \\ \text{BW} &\propto \frac{cos\left[\frac{1}{2}(\pi - \beta)\right]}{d_{Mn-O}}. \end{aligned}$$

Here $\beta$ is the Mn-O-Mn bond angle, $r_A$ is the average radius of A ions and $r_O$ is that of oxygen. $d_{Mn-O}$ is the Mn-O bond length. The tolerance factor is directly proportional to the $r_A$. $\beta$ in the above BW expression depends on the A site radius and larger the $r_A$, smaller the $\beta$ which implies larger the $r_A$ larger is the BW.

Larger BW promotes a ferromagnetic state through the double exchange mechanism. With reduction of the BW, the JT coupling begins to be relevant and charge/orbital ordered phases appear, particularly near commensurate hole doping. The bandwidth is controlled by the mean A site radius ($\beta$ in the above BW expression depend on the A site radius), and along with hole concentration, is a key control parameter in these materials.

While the large BW materials are mainly ferromagnetic metals in the a large part of doping window, and the small BW materials are insulating, there is a wide variety of phases that show up at intermediate BW.

The manganites are classified into low, high, and intermediate bandwidth cases. For example doping $LaMnO_3$ with different AE elements like Ca, Sr, and Ba changes the average radius, $r_A$ of the A site. Doping Ba in place of La leads to larger $r_A$ while doping Ca leads to lower $r_A$. In that sense one can arrange $La_{0.5}Ca_{0.5}MnO_3$, $La_{0.5}Sr_{0.5}MnO_3$, and $La_{0.5}Ba_{0.5}MnO_3$ in increasing order of bandwidth.

One would expect that increasing BW would strengthen the ferromagnetic tendency and that is what happens in this series of materials. $La_{0.5}Ca_{0.5}MnO_3$ (LCMO) is a 'CE' type antiferromagnet with charge ordering while $La_{0.5}Sr_{0.5}MnO_3$ (LSMO) is an A type of AFM without any charge ordering [31], while $La_{0.5}Ba_{0.5}MnO_3$ (LBMO) is found to be a ferromagnetic metal [6].

Experiments have also been done with a combination of AE ions, Ca and Sr, or Ca and Ba, to explore the effect of increasing BW. The charge ordered CE type AFM ex-

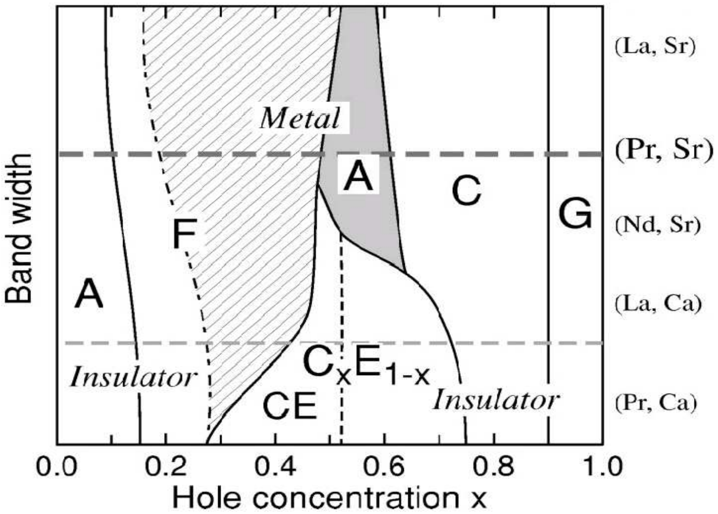

Figure 1.11: Schematic phase diagram of $A_{1-x}A'_xMnO_3$ . F denotes FM state. A, CE, C, and G denote A-type, CE-type, C-type, and G-type AFM states, respectively. $C_xE_{1-x}$ represents an incommensurate charge/orbital ordered state. From R. Kajimoto, *et al.*, Phys. Rev. **B 66**, 180402 (2002).

ist for $La_{0.5}Ca_{0.5-y}Sr_yMnO_3$ when $y \sim 0 - 0.3$ [32]. For $y > 0.3$ the charge-ordered state vanishes due to the competing double exchange interaction dominating over superexchange + electron-phonon coupling and the magnetic order changes from CE to A type AFM. The substitution of larger Ba ions in place of Ca in $La_{0.5}Ca_{0.5-y}Ba_yMnO_3$ results in a non monotonic variation of the Curie temperature [33]. The system evolves from a charge-ordered insulating state for $y = 0$ to a ferromagnet metal for $y = 0.5$. Fig-1.11 [31] organises a 'ground state phase diagram' in terms of hole doping and BW variation. There is a clear change in the ground state with BW variation at fixed hole density.

## 1.4 Effects of disorder

When we discussed the bandwidth variation due to hole doping (AE doped in place of RE ions) we neglected another important aspect associated with doping. Because the radius of AE and RE ions are different, their size mismatch leads to disorder. Apart from size mismatch, there is the difference in the ionic charge of A and A' ions. Usually the quenched disorder suppresses ordering tendencies and leads to an inhomogeneous phase, but, as we discuss in detail in the next chapter, some dopants on the Mn site can

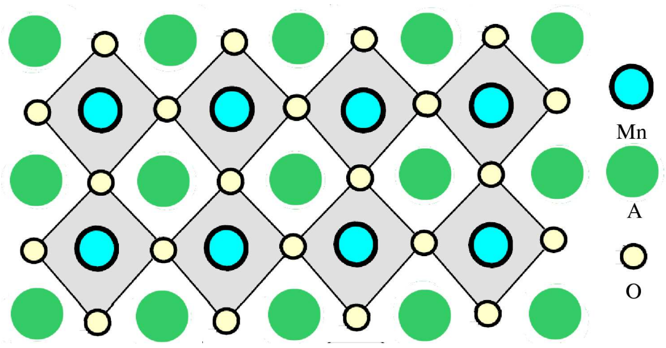

Figure 1.12: A schematic for perovskite $AMnO_3$ in 2 dimension. A is a RE ion.

actually promote (competing) long range order.

The manganites are involve different ions in cubic or distorted perovskite. Let us take the original undoped manganites $AMnO_3$ to be the reference perovskite structure. A schematic figure for perovskite structure $AMnO_3$ in 2 dimension shown in Fig-1.12. For hole doping, A′ ions (AE ions) replace the A ions (RE ions). The difference in the radius between the randomly located A and A′ creates 'quenched' disorder, while the *mean* radius $r_A$ of the A site ion controls the bandwidth.

The Mn-O-Mn bond angle changes from 180 degrees with increasing doping of A′ in place of the A and leads to a distribution of bond angles arising from the randomly located dopants. With different A and A′ concentration in the sample, the disorder is always present and the strength of disorder depends on the radii of A and A′ ions. For example Ca replacing La creates little disorder, but Sr and Ba create successively greater disorder. (See the ionic radius for different ions in Table-1.1). In the manganites, the average radius ($r_A$) controls the bandwidth while variance $\sigma_A$ of the A site radii control the magnitude of disorder.

A site disorder is unavoidable except in few cases of specific $x$ and special growth technique [6]. What about doping on the *Mn site*?! Although Mn site doping is not required for control of the hole concentration, several remarkable effects emerge from this exercise. Since the entire next chapter is devoted to a discussion of disorder we do not expand on this theme here.

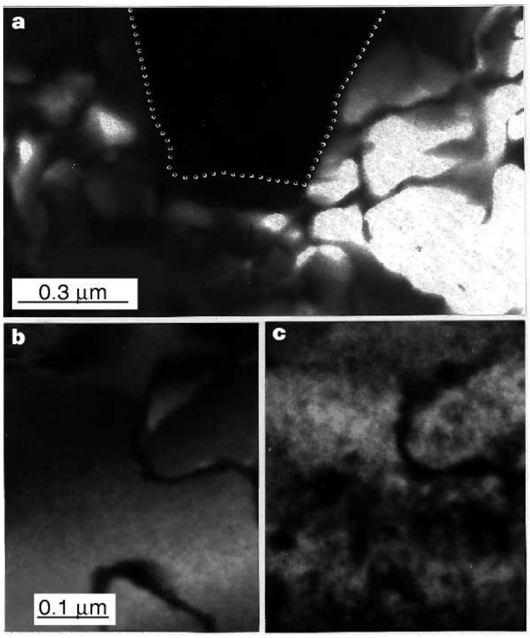

Figure 1.13: Panel (a) shows the coexistence of charge-ordered (insulating) and charge-disordered (FM metallic) domains at 20 K for y = 0.375. The charge-disordered domain (dark area) is highlighted with dotted lines for clarity (dark-field image). Panels (b)and (c), obtained from the same area for y = 0.4 at 17 K and 120 K, respectively, show the development of nanoscale charge-disordered domains at temperature greater than transition temperature. From M. Uehara, *et al.*, Nature **399**, 560 (1999).

## 1.5 Phase coexistence

There are several phases that occur over a relatively narrow density window in some manganites. Tuning the bandwidth or doping level near a phase boundary leads to drastic change in the physical properties. The competition between phases can lead to cluster coexistence of competing phases in the presence of disorder. The length scale of these inhomogeneities range from nanometers to a few micrometers.

The earliest report of phase coexistence in manganites goes back to mid 1950′s when Wollan and Koehler [34] reported neutron diffraction peaks corresponding to FM and AFM regions simultaneously in $La_{1-x}Ca_xMnO_3$. In later 1990′s experimental results showed the presence of mixed phase tendency in $La_{5/8-y}Pr_yCa_{3/8}MnO_3$ by using dark-field images [35]. Coexistence of charge ordered insulator and charge disordered metal domains is observed below 20K as shown in Fig-1.13. Bulk transport data suggested the presence of insulating and metallic domains while magnetic data suggested mixed

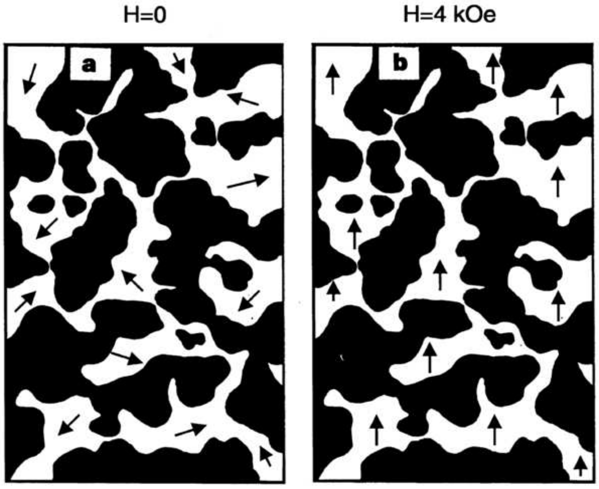

Figure 1.14: The typical size of domains is approx 0.5 micrometer. In zero field, the magnetisations of FM domains are random, but all magnetisations of FM domains can be aligned by applying field of about 4 kOe. From M. Uehara, *et al.*, Nature **399**, 560 (1999).

ferro/anti-ferro character. Later, the spatial nature of these domains have actually been determined using scanning tunneling spectroscopy [37] and magnetic force microscopy [36].

As shown in panel (b) and (c) of Fig-1.13, the development of nanoscale charge-disordered (CD) domains starts at temperature greater than transition temperature. These nanoscale CD regions have ferromagnetic correlations present at a temperature higher than the real transition temperature.

In the small micro domains all the spins are aligned parallel to each other and the domains act like large magnetic moments. These 'moments' are randomly oriented at zero field. A small applied field aligns them, promoting a ferromagnetic state and percolative conduction. A schematic of the process, reproduced from the original paper, is shown in Fig-1.14.

Neutron diffraction studies on $(La_{0.25}Pr_{0.75})_{0.7}Ca_{0.3}MnO_3$ showed peaks corresponding to both ferromagnetic (FM) and antiferromagnetic (AF) phases at low temperatures [38]. Since one requires a 'coherence length' of a few $100\text{Å}$, a lower limit on the size of the domains can be inferred. So both FM and AF peaks at low temperature indicates the existence of a mixed phase. Further work by Balagurov *et al.* [39] indicated that the FM and AF regions in this compound were roughly 100nm in size.

These last three techniques (TEM, STS and neutron diffraction) have all suggested that phase coexistence occurs over hundreds of nanometers. Neutron diffraction studies of $\mathrm{Nd_{0.5}Sr_{0.5}MnO_3}$ shows mesoscopic phase coexistence at low temperatures [40]. Three phases coexist in this case and the CE phase is dominant with more than 60% of the volume in the sample. Other two phases are FM and A type AFM. On application of magnetic field the ferromagnetic phase grows at the expense of antiferromagnetic phases [41].

## 1.6 Model Hamiltonian

As we discussed in the earlier part of the chapter the DE models fails to explain the ferromagnetic transition scale as well as the magnitude of change in resistivity near the transition temperature. While the one orbital DE model has interesting physics content, as we will see in Chapter.6, to approach the phenomena in the manganites one needs to build in the orbital degree of freedom and the Jahn-Teller coupling.

In order to write down a Hamiltonian for the manganites let us go back to the atomic problem we discussed earlier in the chapter. We had described the charge, spin and orbital degrees of freedom to motivate their importance in the manganites. Fig-1.15 summarises the crystal field splitting of the five-fold degenerate atomic 3d levels into $\mathrm{t}_{2g}$ and $\mathrm{e}_g$ levels. The Jahn-Teller distortion of the $\mathrm{MnO_6}$ octahedron further lifts the degeneracy. The crystal field splitting is $\sim$ 1eV and the Hunds coupling $J_H \sim$ 2eV as we discuss later.

It is assumed that the $t_{2g}$ electrons are localised to form core spins, and the $e_g$ electrons can delocalise via the oxygen $2p$ orbital. The hopping motion of $e_g$ electrons via oxygen $2p$ orbital is expressed as

$$H_{\mathrm{k}} = -\sum_{\mathbf{ij}\alpha\beta\sigma} t^{\mathbf{a}}_{\alpha\beta} d^{\dagger}_{\mathbf{i}\alpha\sigma} d_{\mathbf{j}\beta\sigma}, \tag{1.1}$$

where $\mathbf{i}$ and $\mathbf{j}$ are nearest-neighbour sites and $t^{\mathbf{a}}_{\alpha\beta}$ is the nearest-neighbour hopping amplitude between $\alpha$ and $\beta$ orbitals in one direction. The hopping amplitudes, $t^{\mathbf{x}}_{\alpha\beta}$ is explicitly given by $t^{\mathbf{x}}_{\mathrm{aa}} = -\sqrt{3}t^{\mathbf{x}}_{\mathrm{ab}} = -\sqrt{3}t^{\mathbf{x}}_{\mathrm{ba}} = 3t^{\mathbf{x}}_{\mathrm{bb}} = t$, where $t$ is defined by $t = (pd\sigma)^2/|\varepsilon_{\mathrm{d}} - \varepsilon_{\mathrm{p}}|$. Here $\varepsilon_{\mathrm{d}}$ and $\varepsilon_{\mathrm{p}}$ are the energy level for $3d$ and $2p$ orbitals of Mn and O respectively and $pd\sigma$ is the overlap between $d_{x^2-y^2}$ and $p_x$ orbitals. The hopping

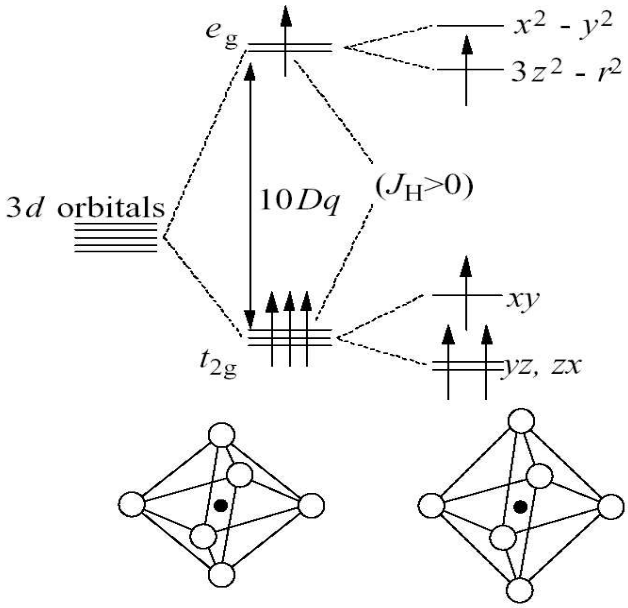

Figure 1.15: Crystal field splitting of the five-fold degenerate atomic 3d levels into lower $t_{2g}$ and higher $e_g$ levels. The Jahn-Teller distortion of the $MnO_6$ octahedron further lifts the degeneracy. The crystal field splitting is $\sim$ 1eV and $J_H \sim$ 2eV.

amplitude along the $y$ and $z$ axis are given by $t^{\mathbf{y}}_{\mathrm{aa}} = \sqrt{3}t^{\mathbf{y}}_{\mathrm{ab}} = \sqrt{3}t^{\mathbf{y}}_{\mathrm{ba}} = 3t^{\mathbf{y}}_{\mathrm{bb}} = t$, and $t^{\mathbf{z}}_{\mathrm{bb}} = 4t/3, t^{\mathbf{z}}_{\mathrm{aa}} = t^{\mathbf{z}}_{\mathrm{ab}} = t^{\mathbf{z}}_{\mathrm{ba}} = 0$, respectively.

The strong Hunds coupling between the localised $t_{2g}$ spins and mobile $e_g$ electrons is included via:

$$H_{\mathrm{H}} = -J_{\mathrm{H}} \sum_{\mathbf{i}} \mathbf{S}_i \cdot \sigma_i, \tag{1.2}$$

where $\sigma_i$= $\sum_{\gamma\alpha\beta} d^{\dagger}_{\mathbf{i}\gamma\alpha} \Gamma_{\alpha\beta} d_{\mathbf{i}\gamma\beta}$, and $J_H \gg t$ is the Hunds coupling between localised $t_{2g}$ spin and mobile $e_g$-electron, and $\Gamma$'s are the Pauli matrices. We treat $\mathbf{S}_i$ as a unit classical vector, absorbing the magnitude of $S$ in the coupling $J_H$. The direction of the classical spin at site **i** is defined as

$$\mathbf{S}_i = (\sin\theta_i \cos\phi_i, \sin\theta_i \sin\phi_i, \cos\theta_i),$$

where the polar angle $\theta_i$ and the azimuthal angle $\phi_i$ define the orientation.

The weak antiferromagnetic superexchange among neighbouring Mn arise due to the fully filled $t_{2g}$ manifold in each. The interaction can be modelled by a Heisenberg coupling between the localised $t_{2g}$ spins:

$$H_{\mathrm{AF}} = J \sum_{\langle \mathbf{i},\mathbf{j} \rangle} \mathbf{S}_i \cdot \mathbf{S}_j, \tag{1.3}$$

where $J$ is the AFM coupling between nearest neighbour $t_{2g}$ spins.

Another important ingredient is the lattice distortion coupled to the $e_g$ electrons due to the JT interaction. The coupling between electrons and Jahn-Teller modes was written by Kanamori and is of the form:

$$H_{\mathbf{i}}^{\mathrm{JT}} = g(Q_{x\mathbf{i}}\tau_{\mathbf{i}}^{x} + Q_{z\mathbf{i}}\tau_{\mathbf{i}}^{z}) + (k_{\mathrm{JT}}/2)(Q_{x\mathbf{i}}^{2} + Q_{z\mathbf{i}}^{2}).$$

Here $g$ is the coupling constant between the $e_g$ electrons and distortions of the MnO$_6$ octahedron, $Q_{x\mathbf{i}}$ and $Q_{z\mathbf{i}}$ are normal modes of vibration of the oxygen octahedron that remove the degeneracy between the electronic levels, and $k_{JT}$ is the spring constant for the Jahn-Teller mode distortions. $\tau_{\mathbf{i}}^{y}$ is absent in the above expression due to symmetry reasons. The pseudospin operators are defined as

$$\tau_{\mathbf{i}}^{x} = \sum_{\sigma}(d_{\mathbf{i}a\sigma}^{\dagger}d_{\mathbf{i}b\sigma} + d_{\mathbf{i}b\sigma}^{\dagger}d_{\mathbf{i}a\sigma}), \quad \tau_{\mathbf{i}}^{z} = \sum_{\sigma}(d_{\mathbf{i}a\sigma}^{\dagger}d_{\mathbf{i}a\sigma} - d_{\mathbf{i}b\sigma}^{\dagger}d_{\mathbf{i}b\sigma}).$$

To complete the electron-phonon coupling term, it is necessary to consider the breathing mode distortion, coupled to the local electron density as

$$H_{\mathbf{i}}^{\mathrm{br}} = g_B Q_{y\mathbf{i}}\rho_{\mathbf{i}} + (1/2)k_{\mathrm{br}}Q_{y\mathbf{i}}^{2}.$$

The Jahn-Teller and breathing modes compete with each other in the manganites. The energy gain due to the Jahn-Teller distortion is maximized when *one electron* exists per site and the breathing mode distortion energy is proportional to the total number of $e_g$ electrons per site.

In principle we should add phonon dynamics to the Hamiltonian, but we neglect the phonon dynamics and work in the adiabatic approximation. Adiabatic approximation is in principle valid when time scales for the motion of electron is smaller than the ions. This time scale is determined by the inverse of kinetic energy scale (t) $\&$ the inverse of phonon frequency for electron and ions respectively. The specific value for phonon frequency, $\sim 0.06$eV, and the electronic bandwidth, $\sim$ 2eV, suggest that electron motion is much quicker than phonon relaxation, and motivate to use the adiabatic limit. It also enormously simplifies the calculation.

The parameter $\beta$ = $k_{br}/k_{JT}$, which regulates the distortion among the Jahn-Teller and breathing mode, plays an important role to decide the role of JT distortion over the breathing mode. $\beta$ is given by $\beta$ = $k_{\mathrm{br}}/k_{\mathrm{JT}}$ = $(\omega_{\mathrm{br}}/\omega_{\mathrm{JT}})^2$, where $\omega_{\mathrm{br}}$ and $\omega_{\mathrm{JT}}$ are the vibration energies for the manganites breathing and Jahn-Teller modes, respectively. From experimental results and band-calculation data [42], $\omega_{\mathrm{br}}$ and $\omega_{\mathrm{JT}}$ are estimated as $\sim$ 700cm$^{-1}$ (0.09eV) and 500-600cm$^{-1}$ (0.06-0.07eV), respectively, leading to $\beta \approx$ 2. As long as $\beta$ is larger than unity the results are not affected if we neglect the breathing mode and retain the JT mode only.

Neglecting the breathing mode distortions the electron-phonon interaction becomes

$$H_{\mathrm{EP}} = \sum_{\mathbf{i}} H_{\mathbf{i}}^{\mathrm{JT}}. \tag{1.4}$$

The on site Coulomb (Hubbard) interaction decides the occupancy of $e_g$ states at each Mn site. The on site and nearest neighbour terms have the form:

$$H_{\mathrm{el-el}} = U \sum_{\mathbf{i}} \rho_{\mathbf{i}} \rho_{\mathbf{i}} + U^c \sum_{\langle \mathbf{i},\mathbf{j} \rangle} \rho_{\mathbf{i}} \rho_{\mathbf{j}}, \tag{1.5}$$

where $\rho_{\mathbf{i}} = \sum_{\alpha\sigma} n_{\mathbf{i}\alpha\sigma}$ and $\alpha$ is for the two orbitals in $e_g$ sector.

Since $J_H \gg t$, only $e_g$ electrons with 'parallel' spin orientation are allowed on each Mn, while the JT coupling prefers occupancy of only one of the two orbitals. Between them, these couplings mimic the effect of the Hubbard repulsion.

The above discussion shows that there are several important couplings at play in the manganites. These include: (i) $H_{\mathrm{k}}$, the kinetic energy of the $e_g$ electrons, (ii) $H_{\mathrm{H}}$, the Hunds coupling between the $e_g$ electron spin and the localised $t_{2g}$ spin, (iii) $H_{\mathrm{AF}}$, the superexchange coupling between nearest neighbour $t_{2g}$ spins, (iv) $H_{\mathrm{EP}}$, the coupling between the $e_g$ electrons and JT distortions of the MnO$_6$ octahedron, and finally, (v) $H_{\mathrm{el-el}}$, the Coulomb interactions among the $e_g$ electrons.

$$H = H_{\mathrm{k}} + H_{\mathrm{H}} + H_{\mathrm{AF}} + H_{\mathrm{EP}} + H_{\mathrm{el-el}}. \tag{1.6}$$

The parameter estimates for this Hamiltonian are as follows:

- Hopping scale: $t$ is widely believed to be a fraction eV. The estimated value of $t$ is between 0.2eV to 0.5 eV [5, 43].

- Hunds coupling $J_H$: Okimoto *et al.* [44] estimated the value of the Hunds coupling to be order of 2eV, *i.e*, much larger than the $t$. Other results [25, 45] also confirm that the Hunds coupling is greater than 1eV.

- Hubbard interaction $U$: The onsite potential between the $e_g$ electrons is the largest energy scale and is estimated to be order of 5eV for CaMnO$_3$ and order of 3eV for LaMnO$_3$ [46] using photo emission technique.

- Jahn-Teller coupling $\lambda$: The dimensionless electron-phonon coupling, $\lambda$ is defined as $\sqrt{2E_{JT}/t}$ where $E_{JT}$ is the static Jahn-Teller energy. $E_{JT}$ is estimated to be 0.25eV [5]. Using t= 0.2eV $\sim$ 0.5eV, $\lambda \sim 1.0 - 1.6$.

- AF superexchange $J$: The AF scale is the smallest in the manganites. In units of $t$, $JS^2 \sim 0.1t$, estimated by Perring *et al.* [47]. Later estimates have arrived at a smaller value [48]. $J$ cannot be neglected despite its smallness as it is necessary to understand the antiferromagnetism (AFM) in CaMnO$_3$ and to understand the AFM charge ordered state for $x$ = 0.5 as we will discuss in Chapter.3.

One simplification of the model without loss of essential physics is to take the widely used limit $J_H/t \rightarrow \infty$. In such a limit, the $e_g$ electron spin perfectly aligns along the local $t_{2g}$ spin direction, reducing the number of degrees of freedom. Then, in order to diagonalise the Hunds term, the spinless $e_g$ electron operator, $c_{\mathbf{i}\alpha}$, is redefined as $c_{\mathbf{i}\alpha} = \cos(\theta_{\mathbf{i}}/2) d_{\mathbf{i}\alpha\uparrow} + \sin(\theta_{\mathbf{i}}/2) e^{-i\phi_{\mathbf{i}}} d_{\mathbf{i}\alpha\downarrow}$. In terms of the redefined $c$ variables in terms of $d$ variables, the kinetic energy takes the simpler form

$$H_{\text{kin}} = -\textstyle\sum_{ia,\alpha\beta} \tilde{t}^a_{\alpha\beta} c^\dagger_{i\alpha} c_{i+a\beta} \, ,$$

where $\tilde{t}^{\mathbf{a}}_{\alpha\beta}$ is defined as $\tilde{t}^a_{\alpha\beta}$= $\Theta_{ij} t^a_{\alpha\beta}$ with $\Theta_{ij}$ given by $\Theta_{ij} = \cos(\theta_i/2)\cos(\theta_j/2) + \sin(\theta_i/2)\sin(\theta_j/2)e^{-i(\phi_i - \phi_j)}$ . This factor denotes the change of hopping amplitude due to the difference in angles between $t_{2g}$ spins at sites $i$ and $j$.

We have argued that large Hunds coupling and a large JT splitting discourages double occupancy of the $e_g$ orbitals at a site. Due to this the effect of the actual Hubbard repulsion is not crucial, at least in the charge and orbital ordered phases. It is also believed that the CO-OO in the half-doped manganites, a phase of major importance for us, is driven primarily by the strong JT coupling, with the on-site Coulomb interaction playing a lesser role [43]. But in the charge disordered and orbitally disordered case (like in the FM-M phase away from half filling as shown in Fig-1.10), there is no JT distortion to mimic the Hubbard term and one need to include explicit hubbard term. But we work in the case where electron density per site is less than one and neglect the Hubbard repulsion.

Rewriting the overall model with the modified kinetic term, at $J_H/t \to \infty$, and neglecting the electron-electron interaction, we have:

$$H = H_{\text{kin}} + H_{\text{AF}} + H_{\text{EP}}. \tag{1.7}$$

We will add the effect of disorder to this in the later chapters.

## 1.7 Plan of the thesis

The aim of this thesis is to uncover the organising principle behind the wide variety of B site doping results in the manganites, and explore the possibility of B site disorder as a tool for electronic phase control.

In Chapter.2, we will discuss both A and B site disorder, but the focus is mainly on B site doping, classifying the wide variety of results in terms of the reference manganites state and the valence and magnetic character of the dopant.

This is followed in Chapter.3 by a discussion of our results on the impact of weak homogeneous (A site) disorder and strong dilute (B site) scattering on the $x = 0.5$ CE charge ordered manganites. We will use the 'reference' model for the clean manganites discussed in Chapter.1 and incorporate the disorder (A site disorder and B site disorder) into the model. The modelling of B site disorder in this effort is crude, incorporating only a strong repulsive potential, but leads to results which capture few of the key experimental effects, including the percolative metallisation of the CE insulator.

In Chapter.4 and 5 we consider a more elaborate model for B site disorder. The impurities are modelled in terms of their valence in the manganites, the position of the impurity level with respect to the manganese $e_g$ levels, and the exchange and hopping interactions between the dopant and neighbouring Mn atoms. Chapter.4 focuses on situations where valence change on Mn due to B impurities is the key effect, while in Chapter.5 we focus on the impact of magnetic dopants which leads to magnetic reconstruction.

Finally, Chapter.6 is not related to manganites but concerns another family of metallic magnets. We studied the Kondo lattice model, with large S spins, across the whole coupling range - from the perturbative RKKY end to the strong coupling double exchange limit. In addition to solving this model completely, we revisit the classic problem of $4f$ magnetism.

# Chapter 2

# Experimental survey of disorder effects

## 2.1 Background

There are two microscopic sources of disorder in the manganites as we have touched upon in Chapter.1.

- The size mismatch of A and A′ in the material $A_{1-x}A'_xMnO_3$ leads to tilting and distortions of the $MnO_6$ octahedra and variations in local electronic parameters. For a given choice of A and A′ this disorder naturally grows with $x$, peaking at $x = 0.5$, and vanishes at $x = 0$ and $x = 1$. The disorder can be quantified even for more complex A site combinations *e.g,* $A_{1-x}A'_yA''_{x-y}$ *etc*, via the variance.

- For a given A and A′ combination one can substitute on the Mn site. This can change the valence of the Mn, introduce a strong scattering potential in the conduction network, and affect the local magnetic state. Unlike the A site case this cannot be quantified purely by a size variance.

Why are the manganites susceptible to what seem to be only moderate disorder? This entire thesis is geared towards answering that question, but let us provide a suggestion based on our discussion in Chapter.1.

- The multiple strong couplings in the manganites lead to a rich $x - T$ phase diagram with first order phase boundaries. There are regions of (potential) phase separation where disorder can lead to nanoscale textures and percolative phenomena.

- The Jahn-Teller coupling is a major player in the low bandwidth manganites, so, quite independent of phase competition, disorder can interplay with this coupling to promote polaron formation. This is visible in the low $r_A$ ferromagnetic metals.

While broadly the effects above can arise from both 'A site' and 'B site' disorder, we will see that in the disorder regime of relevance, A site mismatch has mainly a disruptive effect on long range order, and enhances the resistivity, while a low density of (suitable) B dopants can promote a competing state even enhancing the conductivity.

Most of the interesting B site doping results have been obtained in systems where the A site mismatch $\sigma_A$ is small. The important effects include metallisation of insulators, emergence of charge order from a homogeneous system, and conversion of antiferromagnets to ferromagnets. Specifically:

1. Doping Fe on a ferromagnetic metal (FM-M) at $x \sim 0.40$ promotes a charge ordered insulating (CO-I) state.

2. Magnetic dopants like Cr, Co or Ni (but not Fe) on the Mn site in a $x = 0.5$ CO-I manganites promote a percolative ferromagnetic metal, while non-magnetic dopants of the same valence do not. Ru or Ti also convert the CO-I to a FM-M.

3. The orbital ordered A type antiferromagnet at $x = 0$ is destabilised in favour of a FM state by both magnetic and non-magnetic dopants.

On spatial imaging most of these systems reveal phase separation (PS) and many of them also exhibit enormous magnetoresistance.

The parameter space describing B site doping is rather large. It involves two key parameters of the 'reference' manganites: the bandwidth (BW), controlled by the average ionic radius $r_A$, and the hole doping $x$. The cation disorder $\sigma_A$ in these manganites is small, typically $< 10^{-3}$ Å$^2$, since strong A site disorder tends to mask the B site effects.

Before describing existing B site experiments, we will describe the effect of A site disorder based on a few experiments in the next section. A site disorder dominates the physics in some of the manganites and must be minimised to bring out the interesting effects of B site doping.

## 2.2 The effects of A site disorder

The size mismatch between A and A′ suppresses long range order in the manganites. Among the phases, the charge ordered state is most affected by A site disorder while the FM-M is relatively weakly affected. Let us start with the impact of A site disorder in the canonical FM-M phase and then move to the CO phase at $x = 0.5$.

### 2.2.1 Impact on the ferromagnetic metal

The ferromagnetism in the manganites is driven by electron delocalisation, and can be related to the electronic kinetic energy. It depends on the hole doping $x$, the bandwidth (dictated by $r_A$) and the scattering/localisation effects brought in by disorder.

It is traditional to track the $T_c$ of ferromagnetic phases (at fixed hole doping) in terms of the 'tolerance factor' of the manganites. The tolerance factor, $t_f$, related to $r_A$, is a measure of bandwidth (BW) in these materials. The tolerance factor and the bandwidth are defined as

$$t_f = \frac{r_A + r_O}{\sqrt{2}(d_{Mn-O})} ,$$

$$\text{BW} \propto \frac{cos\left[\frac{1}{2}(\pi - \beta)\right]}{d_{Mn-O}} .$$

Here $\beta$ is the Mn-O-Mn bond angle, $r_A$ is the average radius of A ions and $r_O$ is that of oxygen. $d_{Mn-O}$ is the Mn-O bond length. The tolerance factor is directly proportional to the $r_A$. $\beta$ in the above BW expression depends on the A site radius, and larger the $r_A$ smaller the $\beta$, which implies larger $r_A$ increases the BW.

A detailed study of doped $LaMnO_3$ at fixed $x$ reveals an interesting relationship between the ferromagnetic $T_c$ and $t_f$ [49]. Fig-2.1 shows an increase in $T_c$ with increasing tolerance factor up to $t_f = 0.93$ after which $T_c$ slowly decreases.

The tolerance factor is large for the $La_{0.7}Ba_{0.3}$ (LaBa) family. This is due to the large ionic radius of La and Ba among rare earth (lanthanide) and alkaline earth elements respectively. The $r_A$ in $La_{0.7}A'_{0.3}MnO_3$ is varied with different size of A′ ion (Ca, Sr, Ba ions). In this LaA′ family the the ionic radius of La is close to the ionic radius of Ca. The La size is about $0.1$ Å smaller than that of Sr, and $\sim 0.3$ Å smaller than that

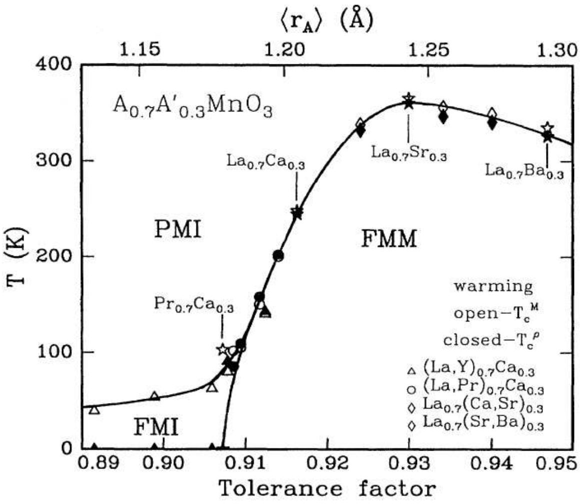

Figure 2.1: Variation of ferromagnetic $T_c$ with tolerance factor for different manganites with $x = 0.3$. From H.Y. Hwang, *et al.*, Phys. Rev. Lett. **75**, 914 (1995).

of Ba. While $r_A$ increases in the sequence LaCa, LaSr, LaBa, the size mismatch $\sigma_A$ also increases quickly in the same sequence.

If the size mismatch were neglected the transition temperature should increase in the sequence LaCa, LaSr, and LaBa. The T$_c$ increases from LaCa to LaSr although the size mismatch between La and A′ increases. In this region the size disorder induced suppression of kinetic energy is the weaker effect, dominated by the gain in kinetic energy due to increase in $t_f$.

From LaSr to LaBa, however, the size mismatch between La and Ba is large enough to suppress the T$_c$ although there is significant increase in $t_f$. This was one of the earliest examples of the impact of A site disorder on the the ferromagnetic phase. Among the rare earth (RE) ions used in the manganites La has largest ionic radius, 1.36Å. Other ions are smaller than La and the smallest radius among them is for Y (1.18Å). Size mismatch between La and Ba suppress the T$_c$ in $La_{0.7}Ba_{0.3}MnO_3$ (LBMO) compared to $La_{0.7}Sr_{0.3}MnO_3$ (LSMO). $\sigma_A$ is smallest for $La_{0.7}Ca_{0.3}MnO_3$ (LCMO) and is less than $0.001$Å$^2$. For LSMO it is roughly $0.002$ Å$^2$ while it increases to $0.013$Å$^2$ for LBMO. The size mismatch between A and A′ increases when rare earth elements change keeping Ba fixed, in the sequence LaBa, PrBa, NdBa, SmBa,... and is very large for YBa. $\sigma_A$ increases from $0.013$Å$^2$ in LaBa to $0.019$Å$^2$ in NdBa and is $0.024$Å$^2$ in SmBa. All the $\sigma_A$ values are taken from the Attfield group [52]

A-site disorder in LaCa or LaSr is smaller than in LaBa but with decrease in the radius of RE ions, from La to Y, the mismatch increases. Studies with controlled variation in $r_A$ indicate that A site disorder has a dramatic effect on the ferromagnetic T$_c$ and resistivity in Ca or Sr doped manganites. For example, $La_{0.7}Sr_{0.3}MnO_3$ (LaSr), is a metal at both low $T$ and $T > T_c$ and shows metal to metal (M-M) crossover. In that spirit, LaCa shows metal to insulator (M-I) crossover, while PrCa shows I-I. These simple binary A site systems are well studied, have relatively small $\sigma_A$, and the transport response can be argued to arise mainly from variations in r$_A$. However, more complex cationic combinations have been used [50, 51, 52, 53, 54], to vary $\sigma_A$ at fixed $r_A$ and $x$. Experimental data with various $\sigma_A$ and $r_A$ for $x = 0.3$ is plotted in Fig-2.2 [55]. In Fig-2.2(a), a transport 'phase diagram' is shown indicating the nature of low temperature to high temperature crossover for different $r_A$ and $\sigma_A$. For instance M-I indicates a metal to insulator transition with temperature. While metal-insulator transition (MIT) driven by reducing $r_A$ are well understood, we see that just increasing $\sigma_A$ at fixed $r_A$ can drive a MIT in a certain parameter regime. Disorder can also drive a metallic system insulating at $T = 0$.

In Fig-2.2(b), the transition temperature decreases with increasing $\sigma_A$. The $T_c$ is larger for large r$_A$ materials even if the disorder is the same. The effect of disorder is more drastic for small r$_A$ materials. The $T_c$ decreases sharply with increase in $\sigma_A$ from zero to $0.01\text{Å}^2$ for $r_A = 1.23\text{Å}$ while the change in $T_c$ for $r_A = 1.26\text{Å}$ is very slow. Other notable effect is the change in $T_c$ for $r_A = 1.20\text{Å}$ when $\sigma_A \sim 0.005\text{Å}^2$. An abrupt change from orbital disorder to order in the insulating regime at $0.005\text{Å}^2$ is evidenced by anomalies in the unit cell parameters and conductivity data [52]. Because of small r$_A$, which implies smaller bandwidth, the Jahn-Teller distortions plays an important role when disorder increases to certain value. One way to understand the connection between disorder and Jahn-Teller distortions in this case is that the both of them leads to localisation of charge and reinforce each other.

### 2.2.2 Effect on the CE charge ordered insulator

At half doping, the manganites are ferromagnetic metal at large $r_A$ and charge ordered insulators with CE magnetic order at small $r_A$. Typically, the A′ ions that replace half the A ions in the $x = 0.5$ material sit in random locations, *i.e*, have an alloy like con-

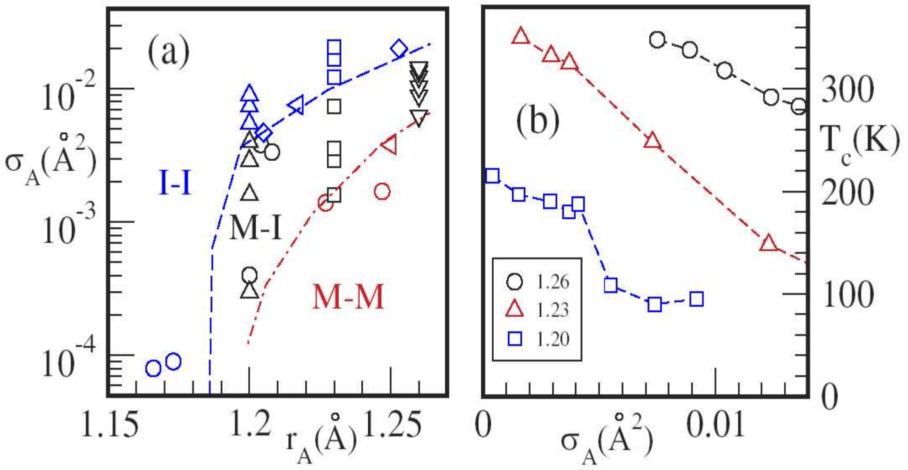

Figure 2.2: Organising the transport crossover and the suppression in ferromagnetic $T_c$ in terms of mean ionic radius, $r_A$, and A site variance $\sigma_A$. (a). Transport 'phase diagram' indicating how the crossover from low to high temperature changes with changing $r_A$ and $\sigma_A$. (b). The ferromagnetic $T_c$. From the experimental data organised in S. Kumar and P. Majumdar, Phys. Rev. Lett. **96**, 016602 (2006).

figuration. The state that emerges is affected by both the mean ionic radius as well as the variance $\sigma_A$, without a simple way to 'deconvolve' the effect of disorder. It is experimentally seen that when half of the lanthanide ions are replaced by Ca, long range CE-CO-OO emerges at the lowest temperature [56]. The long range order survives in these manganites, $A_{0.5}Ca_{0.5}MnO_3$, since $\sigma_A$ is small $\sim 10^{-3}$Å$^2$, so one observes essentially the 'clean' phases.

Replacing Ca with Sr leads to the same CE long range order in the ground state except for $La_{0.5}Sr_{0.5}MnO_3$ (LSMO). LSMO is an A-type antiferromagnet. Unlike the Ca and Sr families, Ba doped manganites had not been studied till recently. One of reason for this was the large size mismatch between Ba and the RE, leading to a strong suppression of long range order.

Millange *et al.* studied the difference between the A site "ordered" and disordered $La_{0.5}Ba_{0.5}MnO_3$ (LBMO) manganite and reported that both are ferromagnetic metal with transition temperature of ordered system greater than that of disordered case [59]. They prepared the oxygen deficient perovskite $LaBaMnO_5$ which is importantly La/Ba ordered in every other (001) layer. Low temperature oxidation of this La/Ba ordered compound, forms $LaBaMn_2O_6$ (2 units of $La_{0.5}Ba_{0.5}MnO_3$) keeping the La/Ba ordering

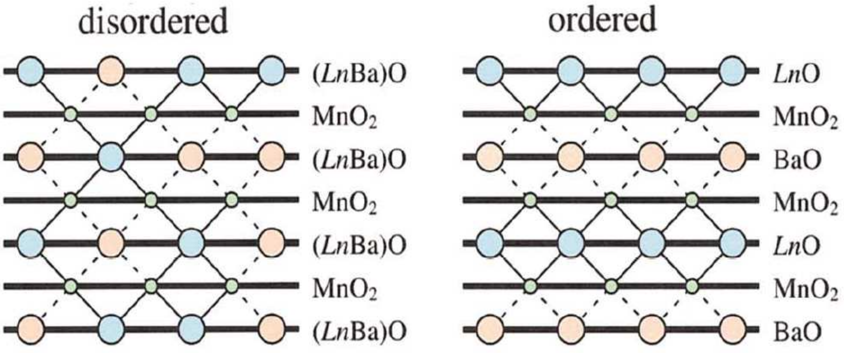

Figure 2.3: Schematic structures of half doped manganites showing the lanthanide (Ln) and Ba ions. **Left:** An A site disordered 'solid solution' with randomly located Ln and Ba. **Right:** A site ordered structure with alternate stacking of LnO and BaO layers. From D. Akahoshi *et al.*, Phys. Rev. Lett. **90**, 177203 (2003).

unchanged. Ueda *et al.* reported that the charge ordering transition temperature for $Y_{0.5}Ba_{0.5}MnO_3$ manganite can be as high as 500K for the ordered case [60].

These two results (La-Ba with largest ionic radius and Y-Ba with smallest ionic radius) show that the Ba doped manganites at half filling varies from a ferromagnetic metal to a CE charge ordered insulator. Till recently there was no experiment to systematically explore the effect of A site disorder on the Ba doped manganites. Akahoshi *et al.* [62] successfully prepared the samples at half filling with a special planar ordering in A (lanthanide) and A' (Ba) ions. Each plane consists of either A or A', a schematic of the ordered and disordered structures at half doping is shown in Fig-2.3.

Before discussing the impact of A site disorder, let us discuss the clean phase diagram first. As shown in Fig-2.4, there are mainly two phases with decrease in lanthanide ionic radius (indicated Ln in the figure). The ground state is ferromagnetic for larger Ln. From LaBa to YBa, the tolerance factor decreases slowly with decrease in ionic radius of Ln, and the ferromagnetic $T_c$ decreases with tolerance factor from LaBa to NdBa. With further decrease in the Ln radius, in SmBa, the localising/charge ordering tendency overcomes kinetic energy and the ground state is a charge and orbital ordered insulator CE magnetic order. With further decrease in the radius the transition temperature for charge ordering increases from Sm to Y. To the right of tricritical point, there is an A-type antiferromagnetic phase in the low temperature regime.

With randomly placed Ba and Ln, known as a solid solution, the ferromagnetic phase

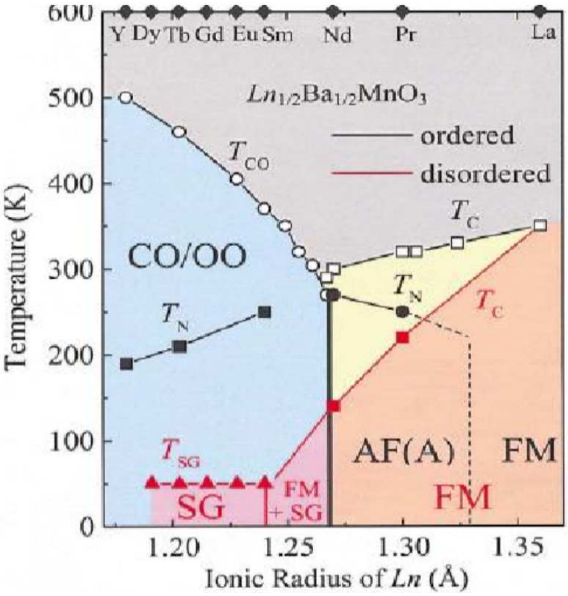

Figure 2.4: Experimental "bicritical" phase diagram in the $x$ = 0.50 manganites obtained for ordered and disordered structures shown earlier. From D. Akahoshi *et al.*, Phys. Rev. Lett. **93**, 227202 (2003).

is weakly affected as shown in Fig-2.4, with a moderate suppression of the $T_c$. The LaBa manganite is least affected and the transition temperature is same in both ordered and disordered case. There is large change in ferromagnetic $T_c$ in the disordered case compared to the ordered structure in PrBa and NdBa. This is because of the increase in size mismatch between Ln and Ba ions. In the ferromagnetic part of the phase diagram, NdBa is most affected and is close to the tricritical point.

The CE-CO phase, however, is completely suppressed and converted to a nanoscale correlated glassy state. The size mismatch between the Ln and Ba in SmBa is more than that of NdBa. This size mismatch between Ln (Sm, Eu, etc.) and Ba suppresses the charge order completely. Analyses of x-ray diffuse scattering and ac susceptibility measurements reveal that the crystals with small bandwidth (Left of SmBa in Fig-2.4) behave like canonical atomic spin glasses. Right of SmBa, $Nd_{0.5}Ba_{0.5}MnO_3$ shows a metallic ground state, as well as CMR in the vicinity of $T_c$ [63]. The CMR seen in the NdBa sample is at an external magnetic field of 7T which is quite large.

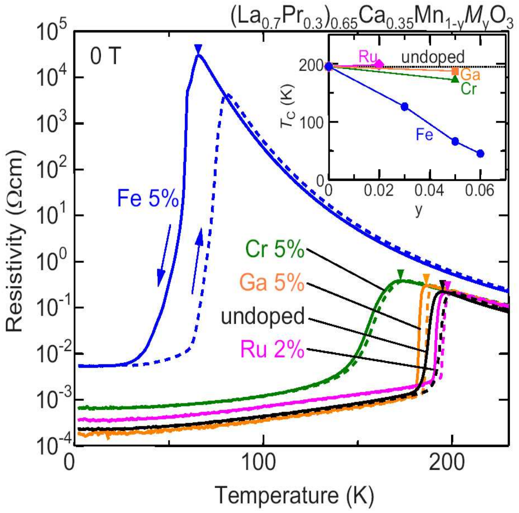

Figure 2.5: Different B site dopants on $(La_{0.7}Pr_{0.3})_{0.65}Ca_{0.35}MnO_3$ (LPCMO). Temperature dependence of resistivity for undoped, 5% M (Fe, Cr, Ga) doped, and 2% Ru doped LPCMO. Inset shows transition temperature versus the doping level. From H. Sakai, *et al.*, Phy. Rev. **B 76**, 155112 (2007).

## 2.3 B site doping experiments

One of the striking early experiments on B site doping was the zero field insulator-metal (IM) transition in $Pr_{0.5}Ca_{0.5}Mn_{1-y}Cr_yO_3$ driven by small percentage of Cr doping [61]. The absence of any spontaneous magnetisation in $Pr_{1-x}Ca_xMnO_3$ for any $x$ and the stability of the insulating state in $Pr_{0.5}Ca_{0.5}MnO_3$ to large magnetic field (up to 28T) added interest to the IM transition with Cr doping [6].

Following this, a large combination of reference states and B dopants have been explored experimentally over the years. The general principle is best illustrated by focusing on two reference states, (i) the FM-M at $x \sim 0.33 - 0.40$, and (ii) the CE-CO-I at $x = 0.50$. Within these families, experimenters have explored manganites with different bandwidth, *i.e*, different $r_A$, and studied the impact of dopants with different valence and magnetic character.

For manganites at $x = 0.5$ with weak A site disorder, large $r_A$ leads to a FM-M ground state, small $r_A$ to a CE-CO-OO-I state [62, 56] and intermediate $r_A$ to A-type antiferromagnetic order. Both the FM-M and the CE-CO phase are strongly affected by A site disorder [62] in case of Ba doped manganites (where $\sigma_A \sim 10^{-2}$Å$^2$), so most of the B doping studies are on the $Ln_{1-x}Ca_xMnO_3$ family, where $\sigma_A \sim 10^{-3}$Å$^2$ and the

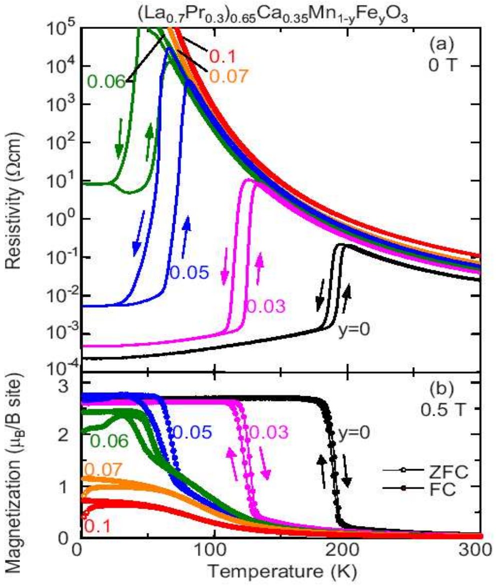

Figure 2.6: Fe doping on LPCMO ($x = 0.35$). Temperature dependence of resistivity at zero field and magnetisation at 0.5T, for Fe doping on LPCMO. Measurements were performed in both cooling and warming runs. From H. Sakai, *et al.*, Phy. Rev. **B 76**, 155112 (2007).

reference state sustains long range order. Typical Ln are La, Nd, and Pr.

### 2.3.1 Doping the ferromagnetic metal

The ferromagnetic metal (FM-M) at $x \sim 0.33 - 0.40$ is a common state in the large and intermediate BW manganites. Moderate disorder does not affect the robust FM metallic state, as we saw in section 2.1, while strong A site disorder can suppress the ferromagnetic $T_c$. However, it does not seem possible to 'transform' the ferromagnetic metal to a CO insulator with A site disorder. This robustness may suggest that a few percent of B site dopants will not have any significant impact on the FM-M state. Surprisingly, CO microdomains seem to form with few percent of selected B site dopants, as we discuss below. This emergence of charge order from a robust ferromagnetic state is rare in correlated materials.

A metal-insulator (MI) transition in the ground state, for Fe doping on a FM-M (LCMO at $x$ = 0.33), was observed a decade back. However, the metal insulator transition with Fe doping was not dramatic in LCMO as a large percentage of Fe doping ($\eta \sim 12\%$ ) is needed to see such effect [68]. A MI transition in the ground state was

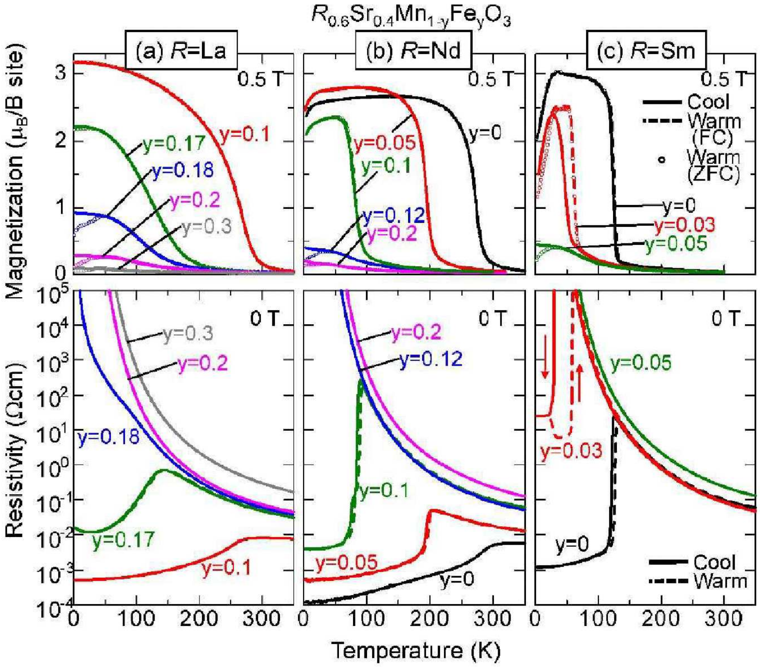

Figure 2.7: Fe doped $R_{1-x}Sr_xMnO_3$ at $x = 0.40$, with R being La, Nd or Sm. Temperature dependence of the magnetisation at 0.5T and the resistivity at zero field. Solid and dashed lines indicate cooling and warming runs, respectively. From H. Sakai, *et al.*, J. Phys. Soc. Jpn. **77**, 124712 (2008).

also seen in the same year with increasing Mg doping onto $Pr_{0.7}Ca_ySr_{1-y}MnO_3$ [69]. Recently with more experiments on Fe doping on a FM metallic state, the minimum $\eta$ required to convert a FM-M to an insulator is down to 5% [70]. The trick was to use low bandwidth manganites with ferromagnetic phase at $x \sim 0.4$. The FM-M state in such a manganite goes insulating at a lower concentration compared to a broadband manganites like LCMO. The charge ordered (CO) microdomains seen recently [70] in these Fe doped systems suggest that the MI transition is not a simple disorder driven localisation.

Here we highlight three sets of measurements in Figs-2.5, 2.6, and 2.7. Fig-2.5 probes the resistivity, $\rho(T, B)$ at fixed $x$, $r_A$ for different dopants (mostly at $\eta = 5\%$) [71]. Fig-2.6 probes $\rho(T, \eta)$ for Fe doping on the same parent manganite as in Fig-2.5. Fig-2.7 probes the $\rho(T, r_A, \eta)$ for various manganites with different bandwidth with Fe dopant [70].

Fig-2.5 shows the change in resistivity with temperature for different dopants (Ga, Cr, and Fe in this case) in the reference ferromagnetic manganite, $(La_{0.7}Pr_{0.3})_{0.65}Ca_{0.35}MnO_3$

(LPCMO), with moderate $\eta$ value (we use $\eta$ instead of $\gamma$ for dopant concentration). The reference manganite is FM-M in ground state and shows a thermally induced metal-insulator transition (MIT). With Fe doping this trend is sharply enhanced, while the FM $T_c$ is strongly suppressed.

Note that the LPCMO sample is close [35] to a charge ordered state. The impact of Ga, Cr and Fe doping in FM-M state appears to be qualitatively different at intermediate temperature with different peak in the resistivity. The resistivity peak with Fe doping is larger than the other two cases. Ga suppresses the $T_c$ from $\sim 190$K to $\sim 185$K, Cr suppresses it to $\sim 160$K but Fe suppresses it to much more lower value $\sim 60$K. All three dopants are expected to be in a $3+$ state in the manganite. By contrast Ru doping seems to have little effect on the system. The puzzles from these results are (i) the qualitatively distinct effects of Ru doping versus the Ga, Cr, or Fe doping and (ii) the quantitatively different effects of Ga, Cr and Fe doping.

Fig-2.6 shows the Fe doping again on an LPCMO sample at $x = 0.35$ for different dopant concentration. It shows the rapid suppression of the ferromagnetic $T_c$, the broadening hysteresis loop close to $T_c$, and the enormous (and very nonlinear) increase in residual resistivity with increasing $\eta$. Around $\eta \sim 7\%$, the ferromagnetic moment goes to $1\mu_B$ and the low temperature resistivity is like that of a CO insulator in manganites.

Fig-2.7 shows the Fe doping, with varying concentration, on three manganites with different bandwidth, for the same hole doping ($x = 0.4$). $La_{1-x}Sr_xMnO_3$ (LSMO), the canonical FM-M has the largest $r_A$ and bandwidth, $Nd_{1-x}Sr_xMnO_3$ (NSMO) has a lower BW, while $Sm_{1-x}Sr_xMnO_3$ (SSMO) has the least. The Fe undoped materials have successively lower $T_c$ in the sequence LSMO, NSMO and SSMO. LSMO seems to be insensitive to Fe doping for $\eta < 0.1$ while even at $\eta = 0.05$ the $T_c$ of NSMO decreases from 300K to 200K. In SSMO the original 120K $T_c$ has been pushed down to $\sim$ 20K with $\eta = 0.05$. The increase in resistivity with $\eta$ gets more pronounced as $r_A$ reduces from LSMO to SSMO. When the bandwidth is reduced by changing $r_A$ from LSMO to SSMO, the Fe content decreases from 18% to 5% which is minimal concentration to suppress the ferromagnetic transition and convert the ferrometal to a charge ordered insulator. The presence of short range charge-orbital ordering at low temperature has been confirmed using transmission electron microscopy.

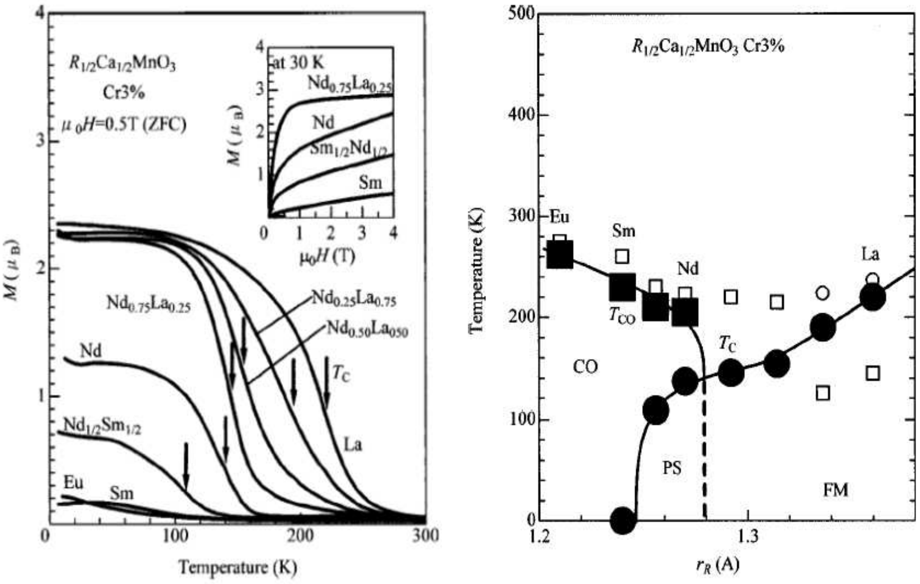

Figure 2.8: **Left**: Temperature dependence of magnetisation M (at 0.5T) for 3% Cr doped manganites $A_{0.5}Ca_{0.5}MnO_3$ with variation of the averaged ionic radius $r_A$. M was measured after cooling down to 5K in the zero field. Arrows indicates the curie temperature. **Right**: Phase diagram of 3% Cr doped manganites $A_{0.5}Ca_{0.5}MnO_3$ against average ionic radius $r_A$. Closed circles and squares are curie temperatures and critical temperatures for the charge ordering transition respectively. Open symbols represent the data for the clean samples with variation of $r_A$(without Cr doped). From Y. Moritomo, *et al.*, Phys. Rev. **B 60**, 9220 (1999). We use A in place of R to denote RE ions.

### 2.3.2 Doping the CE-CO insulator at $x = 0.5$

A large number of experiments have explored the metallisation of insulating states via B site doping. At half filling, the CE-CO-I can be metallised by selected B site dopants. The stability of the CO state in the half doped manganites changes as one moves from LCMO to YCMO, and it is easier to metallise a comparatively weak CO state via B doping. The experimental results can be organized in terms of (i) varying the $r_A$ of the reference manganites, staying at fixed dopant concentration, (ii) varying dopant concentration, and (iii) varying the dopants, staying with a fixed reference state and fixed dopant concentration.

The left panel in Fig-2.8 shows the temperature dependence of the magnetisation M (at 0.5T) for 3% Cr doping into the half doped manganites $A_{0.5}Ca_{0.5}MnO_3$ [56]. There is variation of the average ionic radius ($r_A$) from $La_{0.5}Ca_{0.5}MnO_3$ to $Eu_{0.5}Ca_{0.5}MnO_3$.

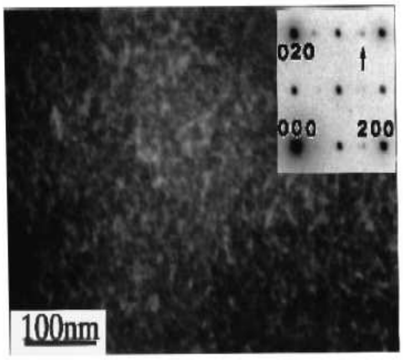

Figure 2.9: Dark field image at 120K (which is less than transition temperature) for $Nd_{0.5}Ca_{0.5}Mn_{0.97}M_{0.03}O_3$. The bright and dark contrast corresponds to the CO and FM microdomains respectively. From Y. Moritomo, *et al.*, Phys. Rev. **B60**, 9220 (1999).

The ground state is a CE-CO insulator for any A ion (La to Eu) for Ca family unlike Ba family. This is shown in right hand side of the same figure with open symbols. When 3% of Cr is doped into $La_{0.5}Ca_{0.5}MnO_3$, it goes to a FM-M at low temperature with magnetic moment larger than $2\mu_B$ in presence of small magnetic field (0.5T).

Conversion of CE-CO insulator to a ferromagnetic phase is quite dramatic in case of $La_{0.5}Ca_{0.5}MnO_3$ (LaCa) with FM $T_c$ more than 250K. The transition temperature decreases with decrease in $r_A$ from LaCa to EuCa. For Cr doping into $Nd_{0.5}Ca_{0.5}MnO_3$, the magnetic moment is still more than $1\mu_B$ and for (NdSm)Ca, the magnetic moment is quite close to $1\mu_B$. There is hardly any ferromagnetic response for SmCa or EuCa manganites. The variation in the B doping induced moment as well as the $T_c$ is controlled simply by the bandwidth.

The right panel in Fig-2.8 shows data at 3% of Cr doping. The averaged ionic radius of the manganites varies from LaCa to NdCa. To get the intermediate $r_A$ in between LaCa and NdCa, (LaNd)Ca manganites used as parent material with different proportion of La and Nd ion in it. As long as La is present, with or without Nd, Cr doping on Mn site converts the CE-CO insulator to a ferromagnetic metal without any sign of phase separation in the low temperature. But for NdCa or (NdSm)Ca, the low temperature state is phase separated into FM and CO microdomains. In these phase separated state, the whole of the CO state does not convert into FM metal. Both the CO insulator and FM 'metal' coexist at low temperature.

Fig-2.9 shows the dark field image at 120K (which is below transition temperature,

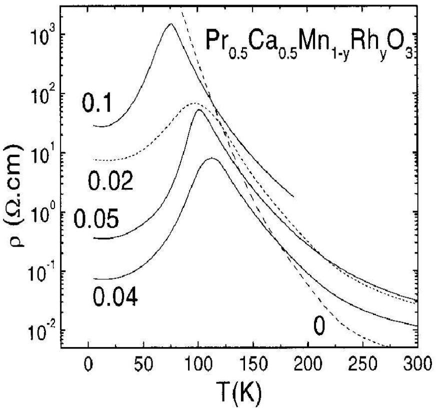

Figure 2.10: Rh doping on PCMO ($x = 0.50$). Temperature dependence of the resistivity in absence of magnetic field. From B. Raveau, *et al.*, J. Appl. Phys. **90**, 1297 (2001).

150K) for $Nd_{0.5}Ca_{0.5}MnO_3$ doped with Cr [56]. The bright and dark contrast corresponds to the CO and FM microdomains respectively. One can clearly see the coexistence of CO and FM domains in it. The effective electron density is 0.485 with 3% of Cr dopant at half filling. The wave vector of the charge ordering in CO regions is found to be 0.445. Overdoped samples ($x$ > 0.5) shows incommensurate wave vector in the ground state and roughly the wave vector, $q$ is proportional to the electron density ($n = 1 - x$) [57]. This incommensurate wave vector for over doped samples is explained using a phenomenological Ginzburg-Landau theory [58]. So the wave vector in the Cr doped $Nd_{0.5}Ca_{0.5}MnO_3$, which is equal to 0.445 indicates that the charge density of CO microdomain is 0.445. The volume ratio of the FM and CO microdomains in the 3% Cr doped $Nd_{0.5}Ca_{0.5}MnO_3$ is 1:1. The electron density of the FM microdomain is estimated to be 0.525 by using the total electron density, the electron density of CO regions, and volume fraction of the two phase. Electron density in the FM microdomain is more than 0.5 while the electron density in CO microdomain is less than 0.5.

Fig-2.10 and Fig-2.11 show the effect of increasing dopant concentration on the CE-CO insulator. Fig-2.10 shows the impact of Rh doping ($4+/5+$ valence) on the half doped manganites, $Pr_{0.5}Ca_{0.5}MnO_3$ [64]. Fig-2.11 shows the effect of Cr doping (3+ valence) on another half doped manganite, $Nd_{0.5}Ca_{0.5}MnO_3$ [65]. Both of the manganites are charge ordered insulator with CE type AFM ground state. In both the cases growing $\eta$ value metallises the CE-CO insulating phase. The detailed physics how-

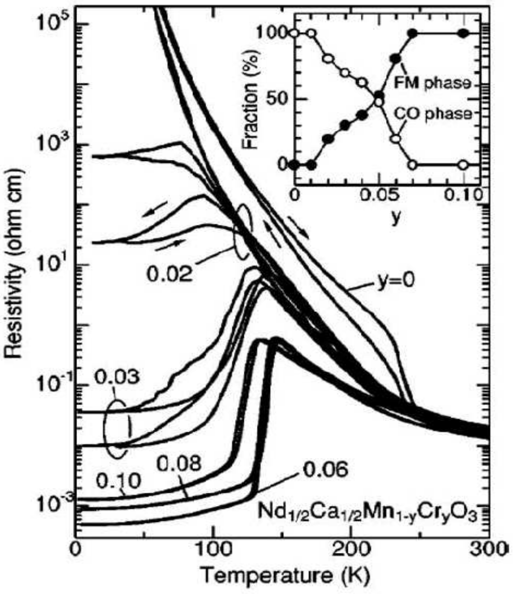

Figure 2.11: Cr doping on $Nd_{0.5}Ca_{0.5}MnO_3$ showing temperature dependence of the resistivity. Inset: Fraction of FM and CO phase at 30K. From T. Kimura, *et al.*, Phys. Rev. **B 62**, 15021 (2000).

ever is quite different in the two cases due to the different valence states and magnetic character of the dopants. Quite generally, the dopant in both cases reduce the low temperature resistivity, producing a peak in $\rho(T)$ which moves outward with increase in $\eta$ value. At moderate $\eta$ it leads to a $\rho(T)$ profile that is reminiscent of the metal to paramagnetic insulator transition in the B undoped $x \sim 0.4$ FM-M state.

The inset in Fig-2.11 demonstrates the volume fraction of CO and FM microdomains found in the Cr doped manganite as discussed in the Fig-2.9. At intermediate $\eta$ the system has *finite phase volumes* of both FM-M and CO-I phases. The system is CO insulator before Cr doping and the CO component decreases with Cr concentration. For 5% Cr doping, the volume of the FM microdomains and the volume of CO microdomains become equal to each other. The CO phase is completely converted into FM-M phase for $\eta \sim 8\%$. The volume fraction of microdomains is inferred via analysis of structural data in the experiment.

Lest it create the impression that any dopant, irrespective of valence or magnetic character, can convert the CE-CO phase to FM-M, Fig-2.12 shows results on the half doped manganite, $Nd_{0.5}Ca_{0.5}MnO_3$ for a wide variety of dopants with $\eta = 3\%$ [66]. The dopants are either in $2+$ valence state or in $3+$ valence state. Some of the dopants

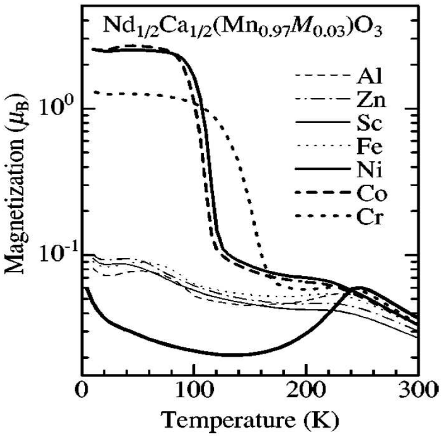

Figure 2.12: Different dopant on $Nd_{0.5}Ca_{0.5}MnO_3$. Temperature dependence of magnetisation M for different dopants (Al, Zn, Sc, Fe, Ni, Co, Cr). magnetisation was measured under a field of 0.5T in warming run after cooling down to 10K in the zero field. From A. Machida, *et al.*, Phy. Rev. **B 65**, 064435 (2002).

are magnetic while others are non-magnetic. Among the non-magnetic dopants a few have full $d$ shell and others are without any $d$ electron. As shown in Fig-2.12, only three of the dopants (Cr, Ni, and Co) create ferromagnetism from a CE-CO insulator state while other cases show no sign of ferromagnetism.

The Fig-2.13 compares the impact of Ru (a 4+ dopant) and Cr (a 3+ dopant) on the $Ln_{0.5}Ca_{0.5}MnO_3$ family [67]. The bandwidth (BW) reduces along the Ln series from La to Ho. Here 5% of Cr or Ru is doped into the manganites as opposed to 3% Cr in Fig-2.8. With 5% Cr or Ru, the low temperature magnetic moment increases up to $3\mu_B$ for LaCa, PrCa, and NdCa whereas the magnetic moment remains below $1\mu_B$ for SmCa and HoCa. The ferromagnetic transition temperature for the LaCa manganite is larger than other two among LaCa, PrCa, and NdCa manganites with Cr or Ru doping. Ru doping has systematically larger ferromagnetic transition temperature as compared to Cr doping for any of the LnCa manganite as shown in Fig-2.13. For SmCa and HoCa manganite, neither Ru nor Cr doping creates ferromagnetism at least with $\eta = 5\%$ used in this experiment. The Ru valence (4+) may be playing a decisive role here in producing the higher $T_c$.

The lower the bandwidth of the manganite, the stronger the CO state at $x = 0.5$. It is not easy to 'melt' a 'strong' CO state like that in HoCa at half filling. The CO in LaCa is relatively easy to destroy. It is mainly Ca based manganites that are studied at half

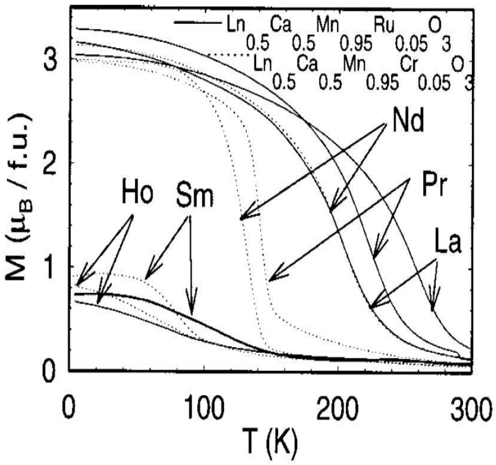

Figure 2.13: Cr and Ru doping on $Ln_{0.5}Ca_{0.5}MnO_3$, with Ln being La, Nd, Pr, Sm and Ho. magnetisation data at 5% doping of Ru (solid lines) and Cr (dotted lines) at 1.45T From C. Martin, *et al.*, Phy. Rev. **B 63**, 174402 (2001).

filling to explore metallisation of the insulator with B dopants.

### 2.3.3 Doping the AF-OO insulator at $x = 0$

Most of the B doing experiments are at $x = 0.5$ to understand the metallisation of the CO-I. However, there has also been work on B doping the parent AF-CO-I at $x = 0$.

$LaMnO_3$ (with $x = 0$) is an A type antiferromagnet with orbital ordering temperature $\sim 750$K. It is insulating to high temperature. When doped with a few percent of Co, this induces ferromagnetism. This ferromagnetism is due to mixed valence state of Mn ($Mn^{4+}$-$Mn^{3+}$) resulting from Co doping. It was believed initially that the ferromagnetism induced is due to the ferromagnetic interaction between Co and Mn [73]. Other magnetic and non-magnetic dopants with different valence state have been doped into $LaMnO_3$, to check if mixed valence is the origin of the observed effect. In Fig-2.14, the magnetisation resulting from a wide variety of magnetic as well as non-magnetic dopants is shown. With increase in $\eta$ for Co, Ni, Zn or Li the ferromagnetic peak, at low $T$ and weak field, increases quickly. With Ga or Ru the increase in dopant concentration shows less effect.

Among the six dopant Zn is divalent, Li is monovalent. Ni and Co are found to be in both $2+/3+$ valence state [74]. Ga is $3+$ dopant while Ru is in $4+$ valence state. At low temperature for non-magnetic dopants like Zn or Li the ferromagnetic peak is due

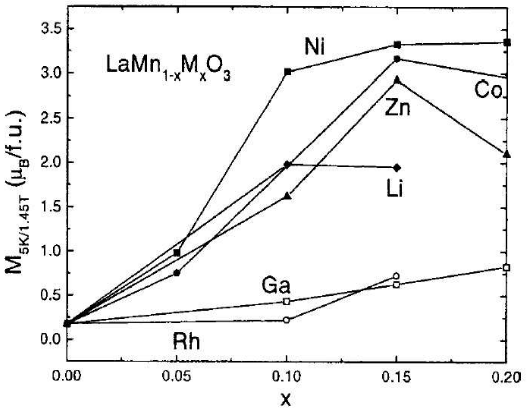

Figure 2.14: Doping dependence of magnetisation at 5K and 1.45T field for different dopants on LaMnO$_3$. From S. Hebert, *et al.*, Phy. Rev. **B 65**, 104420 (2002).

to the mixed valent state in Mn.

This study of the substitution on the Mn site in LaMnO$_3$ shows that the valence of the foreign element plays a prominent role in destroying the orbital ordering and inducing ferromagnetism. As ferromagnetism is observed for non-magnetic 2+ or 1+ dopants, the origin of ferromagnetism cannot be explained by the possible ferromagnetic superexchange between Mn$^{3+}$ and B$^{1+}$ or B$^{2+}$ species. The introduction of Mn$^{4+}$, which can induce double exchange, is necessary to efficiently break orbital ordering and associated A-type antiferromagnetism leading to strong ferromagnetism. For the Ni and Co substituted systems, the divalent nature of these substituting elements could also be responsible for the induced ferromagnetism. Ferromagnetic peak in case Ni or Co doped LaMnO$_3$ manganite is larger than Zn doped case. Ferromagnetic peak difference between Zn doped case and Co (or Ni) doped case may be explained with ferromagnetic superexchange with Mn$^{3+}$, which could destroy the OO state of LaMnO$_3$ easily. But in other side, Ga$^{3+}$ or Ru$^{4+}$ would not create any Mn$^{4+}$ species and shows no prominent ferromagnetic peak. Ferromanetic interaction between B dopant and Mn$^{3+}$ may be playing a role but not necessary to create ferromagnetism in orbital ordered LaMnO$_3$.

## 2.4 Conclusions

We discussed a few experimental results on 'A site' and 'B site' disorder in the manganites.

First we discussed A site disorder in the ferromagnetic metal. There is always a competition between the bandwidth and strength of the disorder. In large bandwidth materials A site disorder decreases the ferromagnetic transition temperature. In the half doping case, the ground sate is CO-OO at low bandwidth and FM-M at large bandwidth in the absence of disorder. Moderate A site disorder destroys the CO-OO and creates spin-glass like phase.

We also discussed experiments on B site doping, mostly on the FM metal and CE-CO insulator. Suitable B dopants can convert the FM-M to a CO-I state, and convert the CE-CO-I state to a FM metal. These doped states involve cluster coexistence of the competing phases.

# Chapter 3

# Distinct effects of A and B site disorder

The manganese oxides of the form $A_{1-x}A'_xMnO_3$ involve a remarkable interplay of charge, spin, lattice, and orbital degrees of freedom [5]. This cross coupling is most striking in the half doped $(x = 0.5)$ manganites many of which have a charge and orbital ordered insulating (CO-OO-I) ground state with 'CE' magnetic order - a zigzag pattern of ferromagnetic chains with antiferromagnetic (AF) coupling between them. The CE-CO-I phase shows up in manganites with low mean cation radius $(r_A)$ while systems with large $r_A$ are ferromagnetic metals (FM-M). The variation of $r_A$ leads to a 'bicritical' phase diagram [62] with a first order boundary between the FM-M and the CE-CO-I phases.

Disorder has a remarkable effect on the bicriticality. Even moderate 'alloy' disorder, due to random location of A and A' ions at the rare earth site, converts the CE-CO phase to a short range correlated glass, but has only limited impact on the ferromagnet [62, 63, 6]. The asymmetric suppression of spatial order by cation disorder and the emergence of a charge-orbital-spin glass at low $r_A$ are one set of intriguing issues in these materials. Unusually, while alloy type randomness on the A site leads to a *homogeneous glassy phase*, the substitution of a few percent of Mn (the 'B site') by elements like Cr [83, 61] leads to *phase separation* of the system [84, 65, 85, 86] into FM-M and AF-CO-I domains. Apart from Cr, other B site dopants like Ru, Rh, Ni, Co also leads to a ferromagnetic metal when doped into the CE-CO phase at half doping [67, 64, 66]. The difference between A and B site disorder holds the key to the much discussed phase coexistence and spatial inhomogeneity in the manganites.

In this chapter we discuss our results on the relative effects of A and B type substitutional disorder on phase competition in a manganite model. We study weak 'alloy' disorder and dilute strongly repulsive scatterers. Our main results are: (i) Alloy disorder indeed leads to asymmetric suppression of long range order; moderate disorder converts long range CE-CO to an *insulating glass* with nanoscale inhomogeneities, while FM order is only weakened. (ii) A low density, $\gtrsim 4\%$, of strong scatterers in the CE phase leads to cluster coexistence of AF-CO + FM regions and the ground state is a *poor metal*.

While we proposed a model for B doping, there has been significant earlier work on modelling A site disorder [55, 77, 78, 80, 81, 95, 82].

## 3.1 Model Hamiltonian and method

We consider a two band model for $e_g$ electrons, Hunds coupled to $t_{2g}$ derived core spins, in a two dimensional square lattice. The electrons are also coupled to Jahn-Teller phonons, while the core spins have an AF superexchange coupling between them. These ingredients are all necessary to obtain a CE-CO phase. Our 'clean' model is defined below:

$$\begin{aligned} H_{clean} &= \sum_{\langle ij \rangle \sigma}^{\alpha\beta} t_{\alpha\beta}^{ij} c_{i\alpha\sigma}^{\dagger} c_{j\beta\sigma} - J_H \sum_i \mathbf{S}_i . \boldsymbol{\sigma}_i + J \sum_{\langle ij \rangle} \mathbf{S}_i . \mathbf{S}_j \\ &\quad - \lambda \sum_i \mathbf{Q}_i . \boldsymbol{\tau}_i + \frac{K}{2} \sum_i \mathbf{Q}_i^2 - \mu \sum_i n_i \end{aligned} \tag{3.1}$$

Here, $c$ and $c^{\dagger}$ are annihilation and creation operators for $e_g$ electrons and $\alpha$, $\beta$ are the two Mn-$e_g$ orbitals $d_{x^2-y^2}$ and $d_{3z^2-r^2}$, labelled $(a)$ and $(b)$ in what follows. $t_{\alpha\beta}^{ij}$ are hopping amplitudes between nearest-neighbor sites with the symmetry dictated form: $t_{aa}^x = t_{aa}^y \equiv t$, $t_{bb}^x = t_{bb}^y \equiv t/3$, $t_{ab}^x = t_{ba}^x \equiv -t/\sqrt{3}$, $t_{ab}^y = t_{ba}^y \equiv t/\sqrt{3}$, where $x$ and $y$ are spatial directions.

The $e_g$ electron spin is $\sigma_i^{\mu} = \sum_{\sigma\sigma'}^{\alpha} c_{i\alpha\sigma}^{\dagger} \Gamma_{\sigma\sigma'}^{\mu} c_{i\alpha\sigma'}$, where the $\Gamma$'s are Pauli matrices. It is coupled to the $t_{2g}$ spin $\mathbf{S}_i$ via the Hunds coupling $J_H$, and we assume $J_H/t \gg 1$. $\lambda$ is the coupling between the JT distortion $\mathbf{Q}_i = (Q_{ix}, Q_{iz})$ and the orbital pseudospin $\tau_i^{\mu} = \sum_{\sigma}^{\alpha\beta} c_{i\alpha\sigma}^{\dagger} \Gamma_{\alpha\beta}^{\mu} c_{i\beta\sigma}$, and $K$ is the lattice stiffness. We set $t = 1$, $K = 1$ , and treat the $\mathbf{Q}_i$ and $\mathbf{S}_i$ as classical variables [87, 88]. The chemical potential $\mu$ is adjusted so that

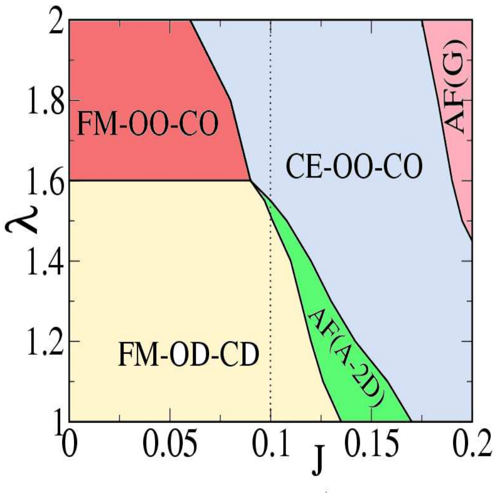

Figure 3.1: The ground state at $x = 0.5$ for various $J$ and $\lambda$, in the absence of any disorder. The vertical dotted line indicates our parameter variation in this study.

the desired electron density is obtained. We include the effect of disorder through an onsite potential in the later part of the chapter.

## 3.2 Phase diagram at $x$ = 0.50

The clean CE ground state at $x = 0.5$ has been studied earlier [89, 90, 91, 92, 93] using mean field and Monte Carlo (MC) techniques and is well understood. The impact of disorder on the phase competition appropriate to $x = 0.5$ has been studied on small clusters [94, 95, 96] usually using simplified models either without orbital variables [95] or ignoring the electron-phonon coupling [96]. The difficulty of simulating the full model, equation[3.1], on a large system has prevented any conclusive study. We use our travelling cluster approximation (TCA) based MC [97] to solve the problem. Compared to exact diagonalization (ED) based MC which can handle typical sizes $\sim 8 \times 8$, we study the full model on lattices upto $40 \times 40$. In all our studies we use a moving cluster of size $\sim 8 \times 8$ [97] to anneal the spin and phonon variables. We explain the method in the Appendix. In the Appendix we also indicate how to calculate the conductivity (using the Kubo approach) and other physical indicators like DOS, and spin structure factors.

Before discussing the effect of disorder we determine the clean ground state at $x = 0.5$ for varying $J$ and $\lambda$, using the TCA, as shown in Fig-3.1. Since the experimental

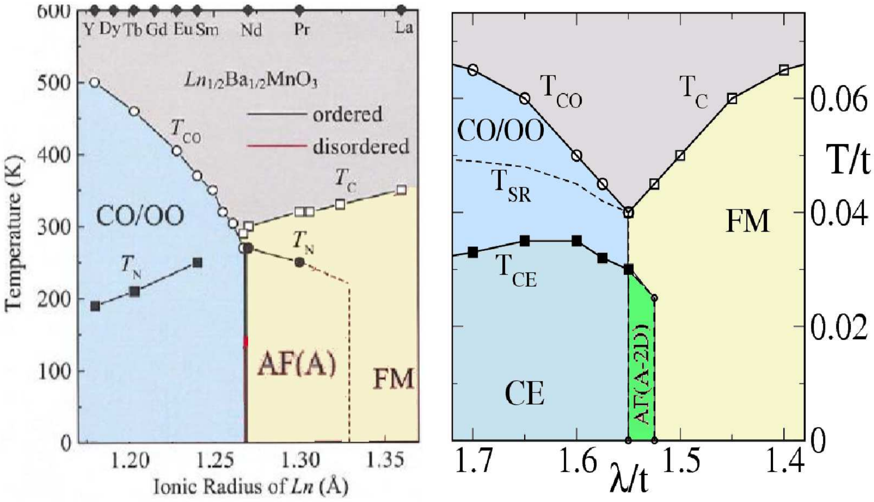

Figure 3.2: (a) Experimental 'bicritical' phase diagram in the $x = 0.5$ manganites obtained for ordered structures [62]. (b) Our result: clean phase diagrams at $x = 0.5$ for $J = 0.1$.

$\mathrm{E}_{JT} = 0.25$eV and $t \sim 0.2 - 0.5$eV, we obtain $\lambda/t \sim 1.0 - 1.6$ [7]. We explore the window $\lambda/t \sim 1 - 2$. We are interested in the CE-CO phase and we find it for $J/t \sim 0.1 - 0.2$ for the $\lambda/t$ range chosen. Our $J$ is really $JS^2$, and given that we have assumed $J_H/t \to \infty$ (overestimating the FM tendency) our $J$ values are reasonable [7, 47].

At low $\lambda$ and low $J$ double exchange is the dominant interaction and kinetic energy optimization leads to a homogeneous ferromagnetic state without any orbital or charge order (FM-OD-CD). This phase has a finite density of states at the Fermi level $\epsilon_F$ and is metallic. As $J$ is increased, keeping the JT coupling small, a magnetic state emerges with peaks in the structure factor $S_{mag}(\mathbf{q})$ at $\mathbf{q} = \{0, \pi\}$ or $\{\pi, 0\}$ (we call this the A-2D phase), then an orbital ordered but uniform density CE phase, with simultaneous peaks at $\mathbf{q} = \{0, \pi\}, \{\pi, 0\}$, and $\{\pi/2, \pi/2\}$. At even larger $J$ the dominant correlations are 'G type' with a peak at $\mathbf{q} = \{\pi, \pi\}$. By contrast, increasing $\lambda$ at weak $J$ keeps the system ferromagnetic but leads to charge and orbital order (FM-CO-OO) for $\lambda \gtrsim 1.6$. Our interest is in a *charge ordered* CE phase. Such a state shows up when both $\lambda$ and $J$ are moderately large. The TCA based phase diagram is broadly consistent with previous variational results [89, 91, 92, 93] and with ED-MC on small systems [90].

Left panel of Fig-3.2 shows the phase diagram of $\mathrm{A}_{1/2}\mathrm{Ba}_{1/2}\mathrm{MnO}_3$ (A is denoted as Ln in the figure). Average radius, $r_A$, of the A site increases from Y to La in the phase

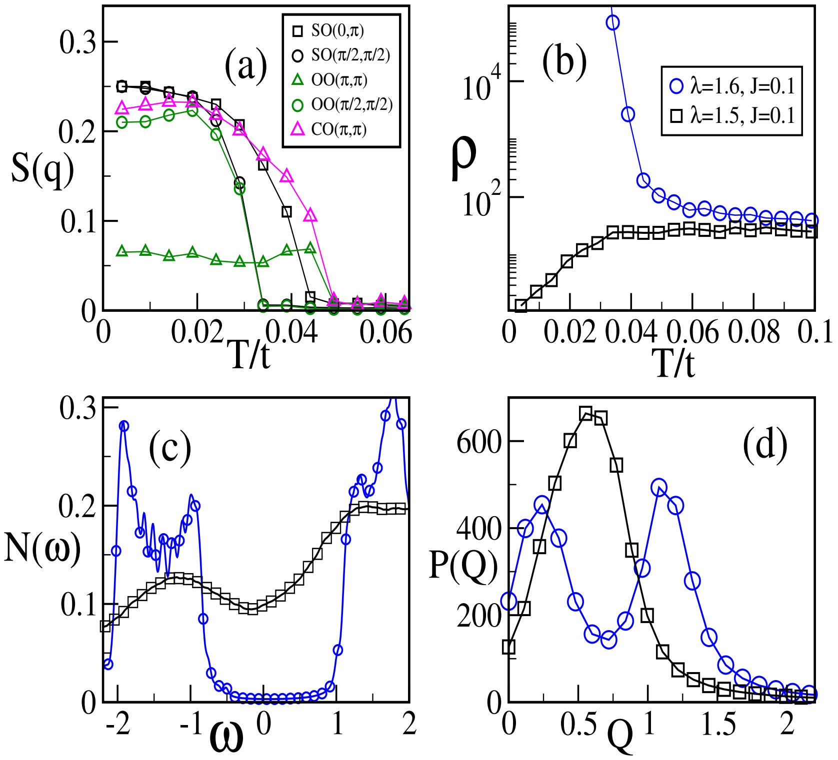

Figure 3.3: Spin structure factors, resistivity, DOS, and P(Q) for CE-CO-I at $J = 0.1$ and $\lambda/t = 1.6$. In (b),(c), and (d) corresponding data for the FM-M (at $\lambda/t = 1.5$, $J = 0.1$) is also plotted. (a) The $T$ dependence of the major peaks in the structure factor for spin order (SO), orbital order (OO) and charge order (CO) in the clean limit. Note the clear separation of scales between $T_{CO}$, $T_{SR}$ and $T_{CE}$. (b) The resistivity for CE-CO-I case with temperature. (c) Density of state for lowest temperature, $T = 0.005$. (d) Distribution of lattice distortions, $P(Q)$ at lowest temperature, $T = 0.005$. P(Q) values are in arbitrary units.

diagram. The average radius controls the hopping scale $t$ in our model. Keeping electron-phonon coupling ($\lambda$) fixed to a value, one should change $t$ to model bandwidth variation. We opt to keep $t$ fixed and vary $\lambda$ to mimic BW variation. Fig-3.1 shows the possibilities of phase change from FM-M to CE-CO-I when we keep $J$ fixed and increase $\lambda$.

To minimise the number of parameters we set $J = 0.1$. We mimic the bandwidth variation arising from changing $r_A$ by varying $\lambda$ across the boundary between CE-CO and FM-OD-CD as shown in the right panel of the Fig-3.2. As we go from $\lambda = 1.4$ to $\lambda = 1.7$, we find mainly three phases in the ground state. We find FM-M at low $\lambda$, A-2D type AFM at a small window of intermediate $\lambda$ value and finally CE-CO-I phase at larger $\lambda$. The three phases we find are similar to the experimental phase diagram shown in the left panel of the figure.

In the clean limit at $T = 0$ as $\lambda$ is increased there is a transition from a FM-M to the A-2D phase at $\lambda/t \sim 1.52$, and then a transition to a CE-CO phase at $\lambda/t \gtrsim 1.55$. On the FM-M side, $\lambda/t \leq 1.52$, there is only a single thermal transition [1] at $T_C$ as one cools the system. At large $\lambda/t$, however, cooling first leads to a CO-OO phase, at $T_{CO}$, without magnetic order, followed by strong features in $S_{mag}$ at $\mathbf{q} = \{0, \pi\}$ and $\{0, \pi\}$, showing up at $T_{SR}$, indicative of stripelike correlations. Finally, at a lower $T$ the system makes a transition to CE order. If we set $t = 0.3$eV, and use a factor of $3/2$ to convert transition scales between 2D and 3D, our $T_C$ at bicriticality would be $\sim 200$K.

There are mainly two phases, FM-M and CE-CO-I arising from the variation of bandwidth in the ABaMnO series. As we will see later, 'A site' disorder effect on the FM-M phase is weak. We are much more interested in the dramatic change in the CE-CO-I phase due to 'A site' disorder.

Before discussing the disorder effect on the CE-CO-I phase, we discuss major the structure factors peaks. Fig-3.3(a) shows the $T$ dependence of the major peaks in the spin, charge and orbital structure factor in the clean limit at $\lambda/t = 1.6$, illustrating the distinct $T_{CO}$, $T_{SR}$ and $T_{CE}$ scales. The resistivity for CE-CO-I case shows strong insulating behaviour at low temperature as shown in (b). Density of states at $T = 0.005$ shows the gap in the DOS around the Fermi level. The distribution of lattice distortions, $P(Q)$, at $T = 0.005$, shown in (d), is bimodal. The corresponding data for the FM-M at $\lambda/t = 1.5$ is shown in (b), (c) and (d) to show the contrast between FM-M and CE-CO-I phase at half filling. We will explain the $P(Q)$ in more detail later since we use it as a probe of charge order and insulating behaviour.

## 3.3 A site vs B site disorder at half doping

### 3.3.1 Minimal model of disorder

At $x = 0.5$, the proportion of A' to A is $\sim 1$, so the disorder is 'homogeneous' over the system, not confined to any special sites since the A and A' ions are randomly present

---

[1] Our 2D magnetic "$T_C$" correspond to correlation length $\xi(T_C) \approx L$. There is no genuine $T_C$ for $L \to \infty$ in 2D. The real 3D $T_C$ will be $\approx 3/2$ times the 2D scale here.

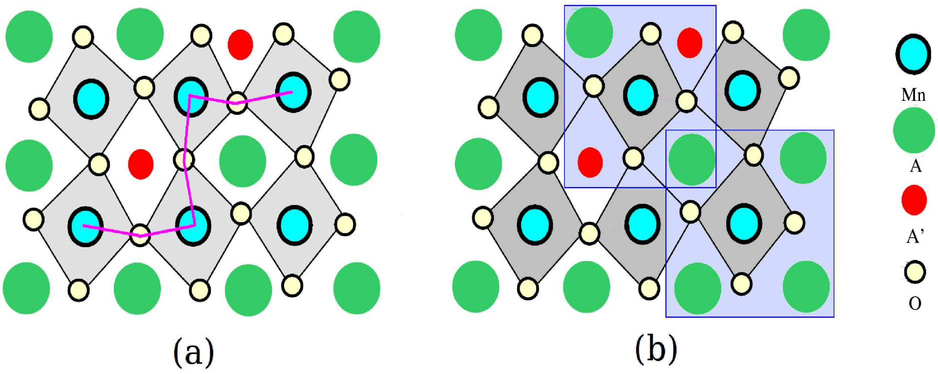

Figure 3.4: A schematic to show the A site disorder in manganites. The A site has RE and AE ions, with small and large radius respectively. (a) Shows the change in Mn-O-Mn angle due to different radii of A site. (b) Shows the different charge environment for the Mn sites due to different AE$^{3+}$ and RE$^{2+}$ ions.

in the sample. Size mismatch between A and A′ ions leads to change in the Mn-O-Mn angle which is connected to the hopping parameter so the random Mn-O-Mn angle acts as a hopping disorder. In our model we include disorder via a random onsite potential on the Mn site. The disorder is picked from the distribution

$$P_A(\epsilon_i) = \frac{1}{2}(\delta(\epsilon_i - \Delta) + \delta(\epsilon_i + \Delta)).$$

Modelling B site disorder is different as only few percent of Mn sites are replaced by a B site dopant. The B dopant are also usually in fixed valence states. This implies that the electron density at the impurity site is fixed and integral, i.e, the impurity level is far above $\epsilon_F$. With all this in mind the B site doping case is modelled via

$$P_B(\epsilon_i) = \eta\delta(\epsilon_i - V) + (1-\eta)\delta(\epsilon_i),$$

where $\eta$ is the percent of substitution and $V$ the effective potential at the impurity site. Our overall model becomes:

$$H = H_{clean} + \sum_i \epsilon_i n_i \tag{3.2}$$

For A type disorder the mean value is $\bar{\epsilon}_i = 0$ and the variance is $\Delta_A^2 = \langle(\epsilon_i - \bar{\epsilon}_i)^2\rangle = \Delta^2$, while for B type disorder $\bar{\epsilon}_i = \eta V$ and $\Delta_B^2 = \langle(\epsilon_i - \bar{\epsilon}_i)^2\rangle \;=\; V^2\eta(1-\eta)$. Schematics of A site and B site disorder are shown in Fig-3.4 and Fig-3.5 respectively.

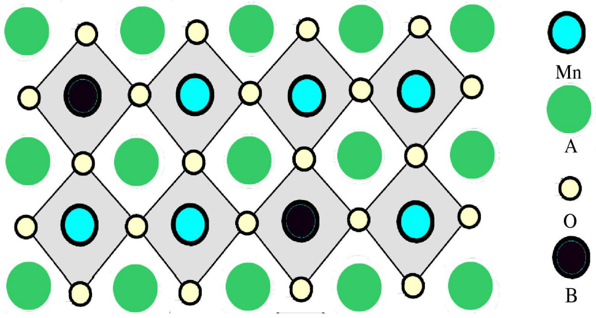

Figure 3.5: A schematic to show the B site disorder in manganites. We keep the radius of A site ion fixed to emphasize Mn site effects. Few of the Mn are replaced by the different element.

### 3.3.2 A site disorder: ‘glassy’ state

The key experiment [62] on the effect of A site disorder on bicriticality compared an ‘ordered’ structure, where the rare earth and alkaline earth ions *sit on alternate layers*, with the ‘disordered’ case where they are randomly distributed. The result is reproduced in the left panel in Fig-3.6. While the ordered case has large transition temperatures for the CO-OO, CE, FM phases, *etc*, a random distribution of A and A′ ions destroy the CE-CO phase and partially suppresses the ferromagnetic $T_c$. The experimental phase diagram has been discussed in Chapter.2.

The right panel in Fig-3.6 shows our result, where we superpose the clean phase diagram and the case with A type disorder $\Delta_A = 0.3$. In the clean limit at $T = 0$ as $\lambda/t$ is increased there is a transition from a FM-M to the A-2D phase at $\lambda/t \sim 1.52$, and then a transition to a CE-CO phase at $\lambda/t \gtrsim 1.55$ as we discussed in the previous section. In the presence of A type disorder with $\Delta_A = 0.3$ we do not find any spatial order on the CE side in either the charge, or orbital, or magnetic sector, down to $T \sim 0.005$. The absence of order in the CE-CO side can be traced back to the ‘random field’ $\epsilon_i$ coupling directly to the charge order parameter $n_i$. This breaks down charge correlations to the atomic scale. The ferromagnet being a $\mathbf{q} = 0$ state is more robust to A type disorder [95].

There are short range stripelike magnetic correlations that persist as peaks at $\mathbf{q} = \{0, \pi\}$ and $\{\pi, 0\}$ in $S_{mag}(\mathbf{q})$. The onset of this feature is shown by the (red) dotted line in right panel of Fig-3.6. This appears even on the ferromagnetic side below $T_C$. The $T_C$ itself is somewhat suppressed by disorder and the ground state is an *unsaturated* ferro-

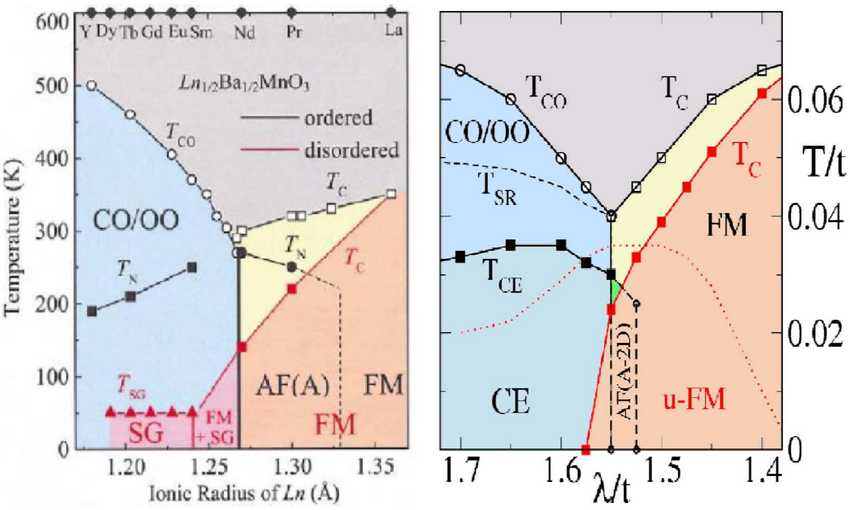

Figure 3.6: (a) Experimental 'bicritical' phase diagram in the $x = 0.5$ manganites obtained for ordered and disordered (alloy) structures [62]. (b) Our results: superposed phase diagrams at $x = 0.5$ for $\Delta_A = 0$ and $\Delta_A = 0.3$. The long range CE-CO for $\lambda > 1.55$ at $\Delta_A = 0$ is completely wiped out at $\Delta_A = 0.3$ while the FM-M phase at low $\lambda$ becomes an unsaturated FM with short range A-2D type correlations.

magnet (u-FM). Our analysis of the structure factor in the disordered system, however, does not suggest any coexistence of two distinct locally ordered phases at any $\lambda$. *A type disorder in the bicritical regime does not induce phase coexistence.* We have confirmed this directly from the spatial snapshots as well, as we discuss later.

We have explored A type disorder with strength $\Delta_A = 0.1,\ 0.2,\ 0.3$ and $0.4$, over the range of $\lambda/t$ value. We now specialize to $\lambda/t = 1.6$, which is a CE-CO phase near the clean phase boundary in Fig-3.6 and explore the impact of A type (and later B type disorder) in detail for various $\Delta_A$. Fig-3.7(a) shows the variation of the major peaks in the magnetic structure factor with $\Delta_A$ at low temperature ($T = 0.01$). Perfect CE phase with $SO(\pi/2, \pi/2)$ equal to 0.25 decreases for $\Delta_A$=0.1 and goes to zero for $\Delta_A$=0.2 and above. Other magnetic structure factor, $SO(0, \pi)$ decreases with increase in $\Delta_A$.

The naive expectation is that disorder would lead to cluster coexistence [98, 99] of AF-CO phases, that arise for $x > 0.5$, with the phase at $x < 0.5$. But the peak at $\mathbf{q} = \{\pi/2, \pi/2\}$ vanishes quickly, leading to a phase with stripelike correlations, and the $\mathbf{q} = \{0, \pi\},\ \{\pi, 0\}$ peaks also vanish for $\Delta_A > 0.6$ leaving a glass.

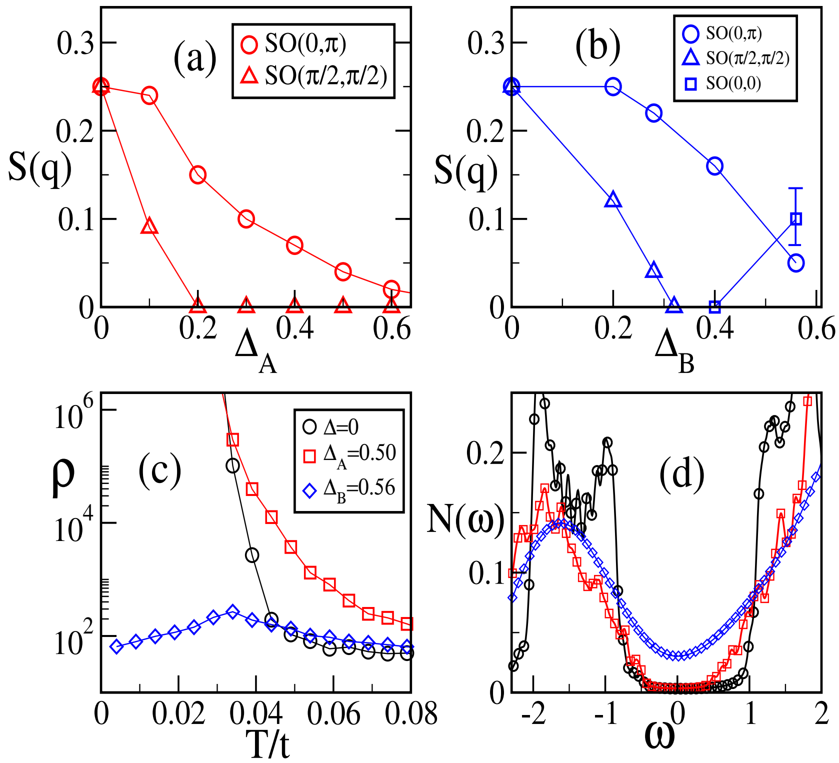

Figure 3.7: Structure factors and resistivity at $J = 0.1$ and $\lambda/t = 1.6$. The B disorder $\Delta_B$ arises from to $V = 2$ and dilution $\eta = 0.08$. (a) Variation of the major peaks in the magnetic structure factor with $\Delta_A$ at low temperature ($T = 0.005$). (b) Same as (a), now with B type disorder, $V = 2$ and varying $\eta$. Note the emergence of the FM $\mathbf{q} = \{0, 0\}$ peak around $\Delta_B = 0.4$ ($\eta = 0.04$). (c) The resistivity $\rho(T)$ in the clean CE-CO case and in the presence of A type and B type disorder, with $\Delta_A \approx \Delta_B \sim 0.5$. (d) DOS for three cases as in (c) at low temperature ($T = 0.005$).

### 3.3.3 B site disorder: phase coexistence

The response to B type disorder is more interesting. We have explored $V = 1,\ 2$ and $4$ and $\eta = 2,\ 4$ and $8\%$. Since B site dopant is believed to be in a definite valence state we focus here on $V = 2$ which is sufficiently repulsive to force $\langle n_i \rangle = 0$ ($e_g^0$ state) at the impurity sites and assume that the valence state of B dopant is fixed. The response, as we vary the fraction of scatterers ($\eta$), is similar to A type at weak $\Delta_B$. However, before the peak at $\mathbf{q} = \{0, \pi\},\ \{\pi, 0\}$ vanishes we see the emergence of a peak at the ferromagnetic wavevector, $\mathbf{q} = \{0, 0\}$ as shown in Fig-3.7(b). There is a window at intermediate $\eta$ where *B type disorder leads to coexistence of FM and CO-OO-AF regions*. In terms of transport, Fig-3.7(c), intermediate A type disorder strengthens the insulating character in $\rho(T)$, while B type disorder of comparable variance leads to an insulator-

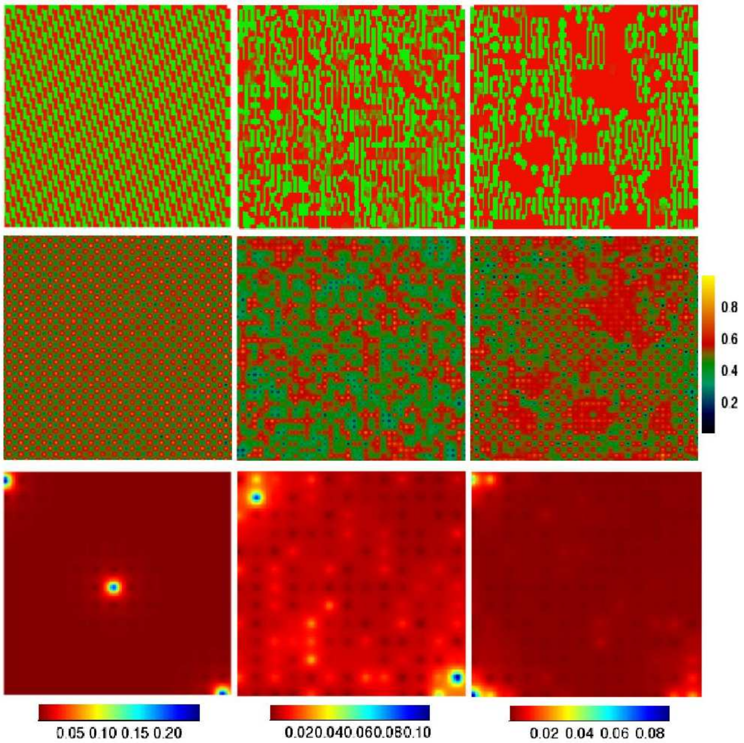

Figure 3.8: MC snapshots and magnetic structure factor at low temperature, $T = 0.01$, size $40 \times 40$. Left row: $\lambda = 1.6$, non disordered, middle row, $\lambda = 1.6$, A type disorder with $\Delta_{eff} = 0.5$, right row, $\lambda = 1.6$, B type disorder with $V = 2$, $\eta = 8\%$, $\Delta_{eff} = 0.56$. Top panel shows the nearest neighbour magnetic correlation $\mathbf{S}_i.\mathbf{S}_{i+\delta}$, where $\delta = x$ or $y$. Middle panel shows the charge density $\langle n_i \rangle$ for the configuration above. Bottom panels shows the MC averaged $S_{mag}(\mathbf{q})$. In each panel $\mathbf{q} = \{0, 0\}$ at the bottom left corner, $\mathbf{q} = \{\pi, 0\}$ at the bottom right corner, *etc*.

metal transition on cooling, and a (poor) metallic state at low temperature.

The top row in Fig-3.8 compares low temperature MC snapshots of the magnetic correlations in the clean system at $\lambda = 1.6$ (left), to that with $\Delta_A = 0.5$ (center) and $\Delta_B = 0.56$ (right). The respective panels in the middle row show the electron density $\langle n_i \rangle$ corresponding to the panels above. The panels at the bottom are the thermally averaged $S_{mag}(\mathbf{q})$ in the three cases. In the clean limit the magnetic correlations are CE, with a checkerboard density distribution, and simultaneous magnetic peaks at $\mathbf{q} = \{0, \pi\}$, $\{\pi, 0\}$ and $\{\pi/2, \pi/2\}$. For A type disorder there are stripelike magnetic correlations with small (atomic scale) FM clusters but no signature of phase coexistence. The density field is also inhomogeneous in the nanoscale, with only short range charge correlations, and $S_{mag}(\mathbf{q})$ has weak peaks at $\mathbf{q} = \{0, \pi\}$ and $\{\pi, 0\}$ but no notice-

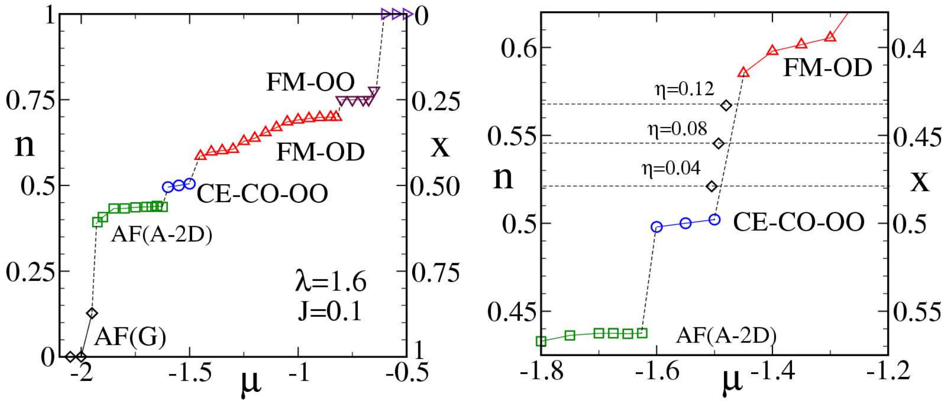

Figure 3.9: The doping ($n = 1-x$) dependence of the ground state for varying chemical potential $\mu$ and typical electronic couplings, $\lambda = 1.6$ and $J = 0.1$, near the FM-OD-CD & CE-CO phase boundary. The phases in the vicinity of $x = 0.5$ (enlarged view shown in the right panel) are expected to show up in a cluster pattern on introducing disorder at $x = 0.5$. Between $x = 0.5$ and $x = 0.4$, the effective carrier density ($x_{eff}$) for different $\eta$ value are shown.

able feature at $\mathbf{q} = \{0, 0\}$. B type disorder, however, leads to FM *regions* coexisting with stripelike AF correlations. The density field shows a corresponding variation, being roughly homogeneous within the FM droplets (with local density $n \sim 0.6$), and a CO pattern away from the FM regions. $S_{mag}(\mathbf{q})$ now has peaks at $\mathbf{q} = \{0, \pi\}, \{\pi, 0\}$ *and* $\{0, 0\}$, as seen earlier in Fig-3.7(b).

## 3.4 Emergence of phase coexistence

Since B site disorder creates cluster coexistence [98, 99] of phases *of different densities* that arise in the clean limit, Fig- 3.9 show the phases and phase separation windows that occur at a typical coupling, $J = 0.1$ and $\lambda = 1.6$. We will explain various phases in the next chapter. We focus on the three phases, one at half doping and other two phases are close to half doping. For these couplings the clean system is a CE-CO phase at $x = 0.5$, a FM-M for $x \lesssim 0.4$, and an A-2D type AF for $x \gtrsim 0.55$. Between these phases there are windows of PS.

Among these three phases, the CE-CO-I at $x = 0.5$ is phase separated from the FM-M and the A-2D at low hole density and large hole density, respectively. If the carrier density is in one of these PS windows the system would break up into coexisting patches

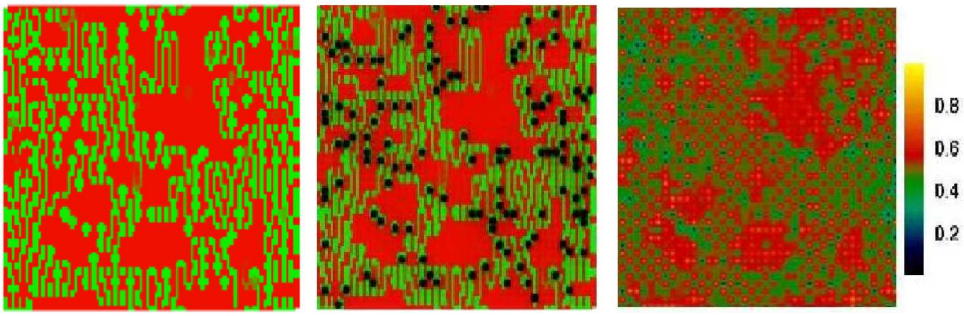

Figure 3.10: Left panel shows the nearest neighbour magnetic correlation $\mathbf{S}_i.\mathbf{S}_j$ with B site disorder of $\eta = 0.08$ as shown in Fig-3.8. Middle panel shows the impurity location with black dots superposed on the left panel. Right panel shows the corresponding charge density $\langle n_i \rangle$ for the same impurity configuration. FM-M cluster is found to be in the impurity free regions.

of the two adjacent phases. For a system at the edge of PS *a small valence change driven variation in the carrier density can push it into the PS window.* The $n_{eff}$ (=1-$x_{eff}$, effective carrier density) for different $\eta$ (at $x = 0.5$) are shown in the right panel of the Fig- 3.9. The tendency towards large scale PS competes with the fragmenting effect of disorder, leading finally to a percolative state. We explain the differing effects of A type and B type disorder as follows.

(1) The introduction of A type disorder does not lead to coexistence of large FM-M and AF-CO-OO clusters, despite the presence of a PS window in the clean problem, Fig-3.9, because (a) atomic scale potential fluctuations disallow CO coherence beyond a few lattice spacings, while (b) homogeneous FM-M clusters are destabilized by the disorder and become charge modulated. The result is a nanoscale correlated insulating glassy phase.

(2) Dilute strongly repulsive scatterers act very differently: (a) they force an $e_g^0$ state at the impurity sites and generate an 'excess density' $0.5 \times \eta$ which has to be distributed among the remaining Mn sites, (b) the parent $x = 0.5$ CO phase cannot accommodate this excess charge homogeneously and the system prefers to phase separate into $x \sim 0.5$ AF-CO and $x \sim 0.4$ FM clusters, (c) unlike the A type case, the FM clusters can survive and percolate since at low $\eta$ there can be *large connected patches* without a B type site. We have verified this explicitly for several impurity configurations.

The current paths in the phase separated regime are dictated by avoidance of B

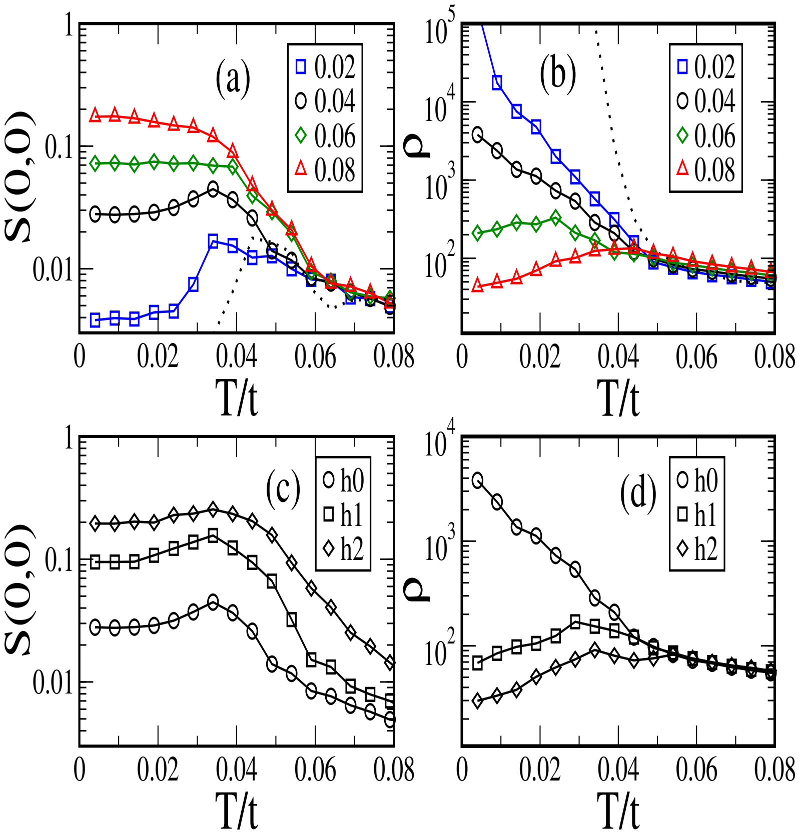

Figure 3.11: Temperature dependence of resistivity and ferromagnetic peak for different B site disorder on reference state $x = 0.50$. (a) Ferromagnetic peak with different $\eta$ value. (b) Resistivity with different $\eta$ value . In (a) and (b) dotted line is for the reference state ferromagnetic peak and resistivity respectively for CE-CO-I phase. (c) ferromagnetic peak and (d) the resistivity variation with temperature for $\eta = 0.04$ in presence of external magnetic field $h_0 = 0, h_1 = 0.002, h_2 = 0.005$ and we use $V = 5$.

dopant sites. Fig-3.10 shows the impurity location in the middle panel of the figure. Left panel of the figure shows the nearest neighbour magnetic correlation with B site disorder of $\eta = 0.08$ as shown in Fig-3.8. Middle panel shows the impurity location with black dots superposed on the magnetic correlation. Right panel shows the corresponding charge density $\langle n_i \rangle$ for the same impurity configuration. Ferromagnetic regions are present in the impurity free region and corresponding FM-CD regions (of electron density 0.6) map to the corresponding ferromagnetic regions shown in the right panel of the figure.

B site disorder effects are interesting because the final state is necessarily inhomogeneous, with possibly huge magnetoresistance (MR). For example if the PS is between

FM-M and AF-CO-I the randomly located B ions fragment the PS state and the FM-M domains in such a situation are weakly linked to each other at zero field. Fig-3.11 shows ferromagnetic peak and resistivity variation with various $\eta$ value. For $\eta = 0.06$, the ferromagnetic peak in close to 0.1 and shows downward turn in the resistivity at low temperature. At larger $\eta$ the ferromagnetic peak increases and metallicity increases at low temperature. This shows that dilute repulsive scatterers, unlike homogeneous disorder, lead to FM-M behaviour at low temperature.

Let us consider smaller $\eta$. For $\eta = 0.04$, the ferromagnetic peak is small and the system is insulating. In this case of $\eta = 0.04$, there are definite FM patches formed but not connected to each other like that in $\eta = 0.08$. Due to poor connectivity, the ferromagnetic domains are aligned randomly. The large 'moments' of the FM-M domains, can be aligned by a small field leading to enormous increase in conductance as shown in the Fig-3.11 (c) and (d). This large susceptibility and MR are key signatures of a PS state.

## 3.5 Conclusions

At hole doping $x = 0.5$ we explored the 'bicritical' regime where the energy of a ferromagnetic metal and a charge and orbital ordered (CO-OO) CE state are closely balanced, and compared the impact of weak homogeneous disorder to that of a low density of strong scatterers. We explained the difference between the impact of A type and B type disorder and compared to the experiments.

The introduction of A type disorder does not lead to phase coexistence while dilute strongly repulsive scatterers leads to coexistence of large FM-M and AF-CO-OO clusters. The FM clusters can survive and percolate since at low $\eta$ there can be *large connected patches*. One can tune the low temperature resistivity with small external field.

# Chapter 4

# Results: valence change effects

## 4.1 Background

As we have discussed, A site disorder originates from the size mismatch of the A and A′ ions in a manganite $A_{1-x}A'_xMnO_3$. This leads to local distortions and tilting of the $MnO_6$ octahedra, modulating hopping amplitudes and superexchange couplings, while the different charge states of the randomly located A and A′ ions lead to a weak random potential at the Mn sites. These specific effects apart, we need to remember the three main contrasts between A and B site disorder:

1. At typical doping levels, $x \sim 0.3 - 0.5$, the proportion of A′ to A is $\sim 1$, so the disorder is 'homogeneous' over the system, not confined to any special sites.

2. The A and A′ ions are away from the crucial $MnO_6$ network that controls the conduction and magnetism.

3. The valence change on Mn associated with the presence of A′ is controlled simply by $x$. So, in comparing disorder effects in a family of the form $A_{1-x}A'_xMnO_3$, we need to worry only about the mean cation radius and the variance, and not about differing carrier densities.

A model for B dopants will differ in that (i) they will be present only on a few percent of Mn sites, (ii) the associated perturbation can be large since they are directly on the conduction path, and (iii) they will in general lead to a modification of the effective carrier density from $x$.

Before we embark on a detailed modelling of B dopants let us explore the qualitative effects of (i)-(iii) above based on our experience with the CE phase in Chapter.3. We start with a discussion of the manganite phases, within our 2D model, in the absence of disorder.

## 4.2 Phases in the absence of disorder

We have discussed the reference manganite model in Chapter.3, so we recapitulate it only briefly here. It includes competing double exchange (DE) and antiferromagnetic (AF) superexchange, and Jahn-Teller (JT) coupling. We ignore the Hubbard interaction between the $e_g$ electrons, and the quantum dynamics associated with the phonon and spin degrees of freedom. These approximations have been discussed in Chapter.1 and are not discussed again.

The experimental control parameters are hole doping $x$, $r_A$ (controlling the bandwidth) and $\sigma_A$ (because of the A site mismatch). The variation of $r_A$ and $\sigma_A$ impact on several parameters in the real system but to capture the essential variation after neglecting the disorder, we vary only a couple of model parameters. We write down the model, already presented in earlier chapters, for completeness.

$$\begin{aligned} H_{ref} &= \sum_{\langle ij \rangle \sigma}^{\alpha\beta} t_{\alpha\beta}^{ij} c_{i\alpha\sigma}^{\dagger} c_{j\beta\sigma} - J_H \sum_i \mathbf{S}_i . \boldsymbol{\sigma}_i + J \sum_{\langle ij \rangle} \mathbf{S}_i . \mathbf{S}_j \\ &\quad - \lambda \sum_i \mathbf{Q}_i . \boldsymbol{\tau}_i + \frac{K}{2} \sum_i \mathbf{Q}_i^2 \end{aligned}$$

We study manganite states at different doping $(x)$, different (inverse) bandwidth $(\lambda/t)$, and AF strength $(J)$. Fig-4.1 shows the phases in $H_{ref}$ for varying 'hole density' $x = 1 - n$. The different phases at $T = 0$, in increasing order of $x$, are an orbital ordered insulator at $x = 0$ [77], a charge-orbital ordered FM insulator at $x = 0.25$, a FM-M window between $x \sim 0.30 - 0.42$, the CE-CO insulator at $x = 0.50$, and a magnetic phase (two dimensional A type 'A-2D'), with structure factor peaks at $\mathbf{q} = \{0, \pi\}$ or $\{\pi, 0\}$, between $x \sim 0.55 - 0.60$. Between these phases are the shaded windows of phase separation (PS). If the carrier density is fixed to be in one of these PS windows, the system would break up into coexisting patches of the two adjacent phases.

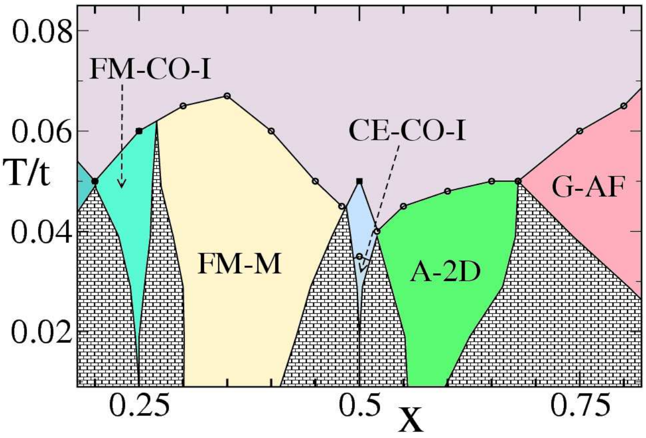

Figure 4.1: The $x-T$ phase diagram of our reference model in 2D at $\lambda/t = 1.6$ and $J/t = 0.1$. The true 3D transition temperatures can be estimated roughly as $3/2$ times the 2D scales indicated here. The phases of interest to us are the ferromagnetic CO insulator at $x = 0.25$, the ferromagnetic metal for $x \sim 0.3 - 0.42$, and the CE-CO phase at $x = 0.50$. Shaded regions indicate phase separation.

The interesting regimes for exploring phase coexistence are those where an insulating phase adjoins a metal. Most of the experiments on B site doping are on the $x = 0.5$ CE-CO insulator and the FM-M between $x \sim 0.3 - 0.4$. Based on our $x - T$ phase diagram we have concentrated mostly on three phases, $x = 0.4$, $x = 0.5$, and $x = 0.25$. Each of these have a window of PS adjoining it.

The density field $n_{\mathbf{r}}$ and the nearest neighbour $\mathbf{S}_i.\mathbf{S}_j$ in the ground state at these three doping are shown in Fig-4.2. Fig-4.3 shows a few more physical indicators for $x = 0.50,\ 0.40,\ 0.25$ and we discuss them as we go along.

### 4.2.1 The CE-CO-I at $x = 0.50$

The CE-CO-OO-I phase is stable only at $x = 0.50$ with windows of PS on either side. To the left is the FM-M while to the right is the A-2D phase. For half doping, there are as many $\mathrm{Mn}^{3+}$ as $\mathrm{Mn}^{4+}$ ions, and the charge order forms a checkerboard pattern with high densities and low densities in the alternative sites. In our calculation, for $\lambda = 1.6$, the CO is a checkerboard with charge density 0.8 and 0.2 on alternate sites (and not quite $1,\ 0$). The pattern is shown in the Fig-4.2 (1st row and 1st column). Hereafter we will refer to charge density $n_i = 0.8$ as $\mathrm{Mn}^{3+}$ and $n_i = 0.2$ as $\mathrm{Mn}^{4+}$ for simplicity.

The $\mathrm{Mn}^{3+}$ and $\mathrm{Mn}^{4+}$ alternate in the (a,b) plane. Mainly the $\mathrm{Mn}^{3+}$ sites (with $n_i \sim 1$)

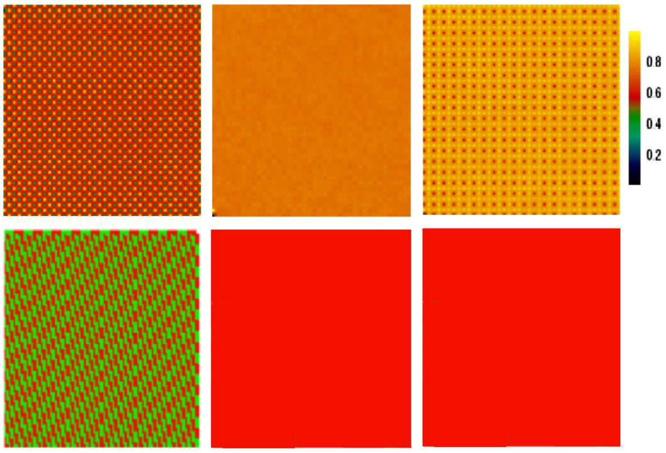

Figure 4.2: Top row: density field $n_{\mathbf{r}}$ at low temperature and bottom row: nearest neighbour $\mathbf{S}_i.\mathbf{S}_j$ from MC snapshots Left to right: $x = 0.50$ CE-CO phase, $x = 0.40$ FM-M, and $x = 0.25$ FM-CO-I.

participate in orbital order and the orbital degree of freedom on the Mn$^{4+}$ sites can be ignored. Orbitals of Mn$^{3+}$ are directed toward Mn$^{4+}$ when their spins are ferromagnetically coupled, and they are directed away from them when antiferromagnetically coupled (see Fig-1.9). As a result, the $d_{3x^2-r^2}$ and $d_{3y^2-r^2}$ orbitals order in 'CE type' antiferromagnetic structure, composed of ferromagnetic zig-zag chains, antiferromagnetically coupled to each other within the (a,b) planes. The magnetic spin correlations are shown in Fig-4.2 (2nd row and 1st column). Electrons delocalise along the zigzag chains as spins are coupled ferromagnetically and the orbital arrangement also facilitates hopping. The system overall is insulating.

Fig-4.3 shows a few physical indicators of the CE-CO-I phase. Fig.(a) shows the DOS at low temperature with a large gap at Fermi level indicating insulating behaviour. The gap at Fermi level is dependent on $\lambda$. Fig.(b) shows the two peak structure of $P(Q)$ at low temperature. The two peaks indicate that the distortion in half of the sites are large and are small on the other half. The large distortion sites lead to $n_i \sim 0.8$. Spatial picture of absolute Q value in whole system shows that large and small distortions are in alternative sites.

We have shown three major features in the structure factor in Fig-3.3 indicative of CE ordering. Fig.(c) shows the ferromagnetic feature in the CE-CO-I phase at half doping, which is naturally very small at low temperature. Fig.(d) shows the temper-

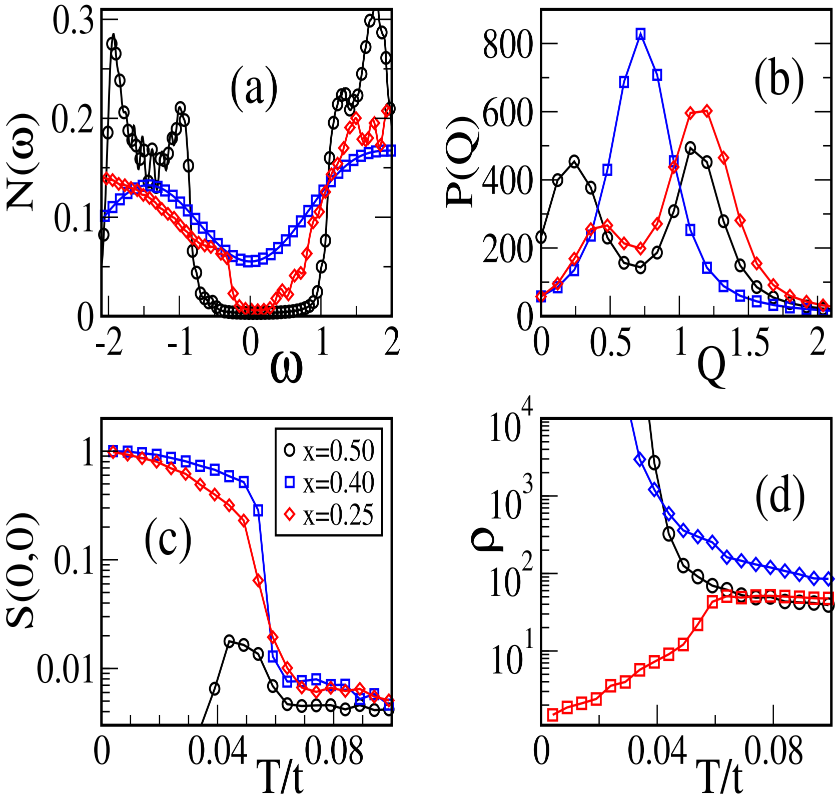

Figure 4.3: Various physical indicators for three states ($x = 0.50$, $x = 0.40$, $x = 0.25$) (a) Density of states at low temperature, (b) $P(Q)$ at low temperature, (c) the FM feature in magnetic structure factor, and (d) the resistivity.

ature dependence of resistivity, with strong insulating behaviour at low temperature. The insulating behaviour is due presence of charge-orbital order, opening a gap in the spectrum.

### 4.2.2 The FM-M at $x = 0.40$

In this case the reference state is a homogeneous metal with density $n = 0.6$ ($x = 0.40$) on the edge of the FM-M window. It is separated from the CE-CO phase on the right by a PS window. At this doping the effective electron-phonon coupling is not strong enough, as compare to the DE interaction, to localize the electrons. In case of hopping between $t_{2g}^3 e_g^0$ and $t_{2g}^3 e_g^1$, the motion of $e_g$ electron is easiest when the $t_{2g}$ spins aligns parallel, and the kinetic energy is progressively suppressed as the spins get out of alignment. Antiparallel spins do not allow any electron hopping.

Fig-4.3 shows a few physical indicators of the FM-M phase. Fig.(a) shows the DOS at low temperature. There is finite DOS at Fermi level ($\omega = 0$) indicating metallic behaviour. Fig.(b) shows the one peak structure of $P(Q)$ at low temperature. The single peak nature indicates that there is equal distortion on all sites. Equal distortion in all sites and finite hole density allow electrons to move from one site to other and in the process there is gain in kinetic energy. The finite distortion at each site ($\bar{Q} = 0.75$) in this case is an artifact of the 2D bandstructure and resulting unequal orbital occupation. Both the e$_g$ levels are partially occupied [78] and the difference in orbital occupation drives a (systemwide homogeneous) distortion in the presence of the Jahn-Teller coupling.

The charge density is uniform and equal to $0.6$, Fig-4.2 (1st row and 2nd column). Fig.(c) shows the ferromagnetic feature in $S(\mathbf{q})$ for the FM-M phase with saturation at low temperature. Fig.(d) shows the temperature dependence of the resistivity and it is metallic at low temperature.

### 4.2.3 The FM-CO-I at $x = 0.25$

In the clean limit the orbital ordered (OO) JT insulator at $x = 0$ is separated from a FM-CO-I at $x = 0.25$ by a wide PS window. It is possible that there could be charge ordered states at lower commensurate hole doping as well, but they probably have very low ordering temperature. The FM-CO-I at $x = 0.25$ can be looked upon as the charge ordering of doped holes with double the lattice periodicity in both $\hat{x}$ and $\hat{y}$ directions. In the 4 site unit cell, three of the sites are of charge density 0.85 while the fourth is 0.45 (Fig-4.2, 1st row and 3rd column). In our phase diagram, Fig-4.1, the phase is stable only at a single hole density.

Fig-4.3 shows physical indicators of the FM-CO-I phase at $x = 0.25$. Fig.(a) is for the DOS at low temperature and shows a gap at Fermi level ($\omega = 0$). The gap at Fermi level is smaller than the half doping case. Fig.(b) shows the two peak structure of $P(Q)$ at low temperature. The two peaks are of different height unlike half doped case and indicate that there are distortions on more than half of the sites. Fig.(c) shows the ferromagnetic peak in $S(\mathbf{q})$ for the FM-CO phase, which is saturated at low temperature. Fig.(d) shows the insulating character in the resistivity at lower temperature.

## 4.3 B doping: general scenario

Before discussing the detailed numerical results it may be helpful to outline the general effects of B doping that one expects given the nature of the clean phase diagram.

### 4.3.1 Valence change and percolation

Consider the simplest model, with no magnetic character of the B dopant. The impurity ions only have a strong repulsive potential, and essentially act as exclusion sites. This is physically too simple to model any real dopants, but conceptually useful. Due to the large $V$, the electron density $n_i$ at the impurity sites is $\ll 1$. Since the total electron count is fixed the effective density, $n_{eff}$, at the Mn sites increases depending on the percentage of B dopants. Consider the $n = 0.5$ reference state. Each impurity increases the electron count, $n_{eff}$, on the Mn background by $0.5$, so $n_{eff} \sim n + 0.5\eta$. For low $\eta$, we will have $0.5 < n_{eff} < 0.6$, which is in the window of phase separation. At the same time B scatterers are still reasonably dilute. In this situation the system breaks up into patches with local densities that are either $n \sim 0.5$ or $n \sim 0.6$, with AF-CO and FM-M correlations respectively as discussed in Chapter.3. It is not hard to see that this principle can be exploited in various parts of the phase diagram.

The valence of the B ions is a crucial factor when classifying B site dopants. Among the usual dopants Zn, Mg, and Co, are divalent, *i.e*, in a $2+$ state, Ni, Cr, Fe, Sc, and Al are trivalent, while Ru, Sn, and Ti are tetravalent. Sometime Co and Ni are found to be in both $2+$ and $3+$ valence state. The valence, $\alpha$, of the dopant affects the effective carrier density on the Mn sites through the charge neutrality requirement on the compound $\mathrm{A}^{3+}_{1-x}\mathrm{A}'^{2+}_{x}\mathrm{Mn}^{3+\nu}_{1-\eta}\mathrm{B}^{\alpha}_{\eta}\mathrm{O}^{2-}_{3}$, where $\eta$ is the % of B site doping, and we write the Mn valence as $3 + \nu$. This yields

$$\nu(\eta, \alpha, x) = (x + \eta(3 - \alpha))/(1 - \eta).$$

The effective $e_g$ electron count on Mn is $n = 1 - \nu$, modified from $n_0 = 1 - x$ at $\eta = 0$.

For a system at the edge of PS *a small valence change driven variation in the carrier density can push it into the PS window.* Fig-4.1 shows many such possibilities. These can be exploited by choosing dopants of suitable valence. The tendency towards PS competes with the fragmenting effect of disorder, leading finally to a percolative state.

### 4.3.2 Magnetic interactions

Dopants with the same valence can have different effects depending on their magnetic character. Non-magnetic dopants only affect the Mn valence, while those with partially filled $d$ shells can have magnetic coupling to the neighboring Mn moments. In fact we will see in the next chapter that there are cases where the magnetic character of a dopant can overcome the valence change effect. Pending a discussion of the microscopic model, we can broadly classify dopants the following way.

1. Most of the dopants with valence $4+$ either do not have $d$ electrons, or have filled 3d/4d shells. We treat these as 'non-magnetic' dopant. We do not consider any superexchange coupling between these ions and neighbouring Mn, and also put a large on site potential so that double exchange effects are suppressed. These enforce 'non-magnetic' character on the site.

2. For dopants with valence $2+$ like Mg, Zn (which are non-magnetic) we use the same principle as above.

3. There are dopants with valence $3+$ like Cr, Ni or Fe. Experiments suggest [100] that Cr has strong AF coupling to the Mn ions, Ni couples ferromagnetically, while Fe, despite its stable magnetic $d^5$ configuration, couples rather weakly.

What decides the superexchange interactions? The superexchange (SE) interaction is dependent on t scale and Hubbard repulsion $U$ as $t^2/U$. In case of Fe$^{3+}$ which is in $t_{2g}^3e_g^2$, the $U$ is large as the next electron will doubly occupy a $t_{2g}$ level. For Cr$^{3+}$ ($t_{2g}^3e_g^0$) the effective $U$ is probably smaller, which is why Cr has a stronger SE coupling to Mn than Fe does.

One can classify magnetic dopants broadly into two classes, one with B-Mn superexchange larger than the Mn-Mn SE, and the other with SE smaller than the Mn-Mn SE. For magnetic dopants the position of the impurity level also makes a difference since it controls double exchange driven ferromagnetic coupling.

Another important aspect is short range Coulomb interaction between the B dopant and the neighbouring Mn site, particularly when charge ordered reference states are considered. In the CE-CO-I state, for example, the Mn alternate (nominally) between Mn$^{3+}$ and Mn$^{4+}$ in a checkerboard pattern. At other filling like $x = 0.25$, out of four sites (which can be taken as unit cell) one is in a low charge state while the other three are in a high charge state. When a B dopant is introduced into a CO-I state the fixed valence (and charge state) of the B ion forces a rearrangement in the valence of the neighbouring Mn to minimize the Coulomb repulsion [101]. For instance, a dopant like Cr which is in $3+$ state is more likely to be surrounded by Mn$^{4+}$ while a $4+$ dopant like Ti would be surrounded by Mn$^{3+}$.

## 4.4 Modelling B site disorder

A model for B dopants in the manganites involves (i) the energy scales and valence of the impurity ion, and (ii) the coupling between the host and the impurity.

The impurity valence in the manganite ought to be determined from *ab initio* calculations or experiments, and we will assume it to be integral. The change in the effective hole density about the reference $x$ is incorporated via the chemical potential. Since the impurity has a well defined valence it would have levels that are far from the Fermi level of the host. If the impurity level were close to $\epsilon_F$ the B ion would be in a mixed valent state, contradicting our assumption about integral valence. Following this reasoning we will usually assume the B ion to have an energy level $V$ such that $(V - \epsilon_F)/t \gg 1$. In addition to the valence state and the energy level, magnetic dopants would be characterised by a local moment and its coupling to neighbouring spins.

The coupling between impurity and host would include hopping from the B ion to Mn (via oxygen), the magnetic coupling between B spin and Mn spin, and short range coulomb interaction. Putting these together the model assumes the form:

$$
\begin{aligned}
H_{tot} &= H_{ref} + H_{imp} + H_{coup} \\
H_{ref} &= \sum_{\langle ij \rangle \sigma}^{\alpha\beta} t_{\alpha\beta}^{ij} c_{i\alpha\sigma}^{\dagger} c_{j\beta\sigma} - J_H \sum_i \mathbf{S}_i . \boldsymbol{\sigma}_i + J \sum_{\langle ij \rangle} \mathbf{S}_i . \mathbf{S}_j \\
&\quad - \lambda \sum_i \mathbf{Q}_i . \boldsymbol{\tau}_i + \frac{K}{2} \sum_i \mathbf{Q}_i^2 \\
H_{imp} &= V \sum_{n\alpha\sigma} d_{n\alpha\sigma}^{\dagger} d_{n\alpha\sigma} \\
H_{coup} &= \sum_{\langle nj \rangle \sigma}^{\alpha\beta} t_{\alpha\beta}^{nj} d_{n\alpha\sigma}^{\dagger} c_{j\beta\sigma} + J' \sum_{\langle nj \rangle} \mathbf{s}_n . \mathbf{S}_j + V_c \sum_{\langle nj \rangle} q_n q_j
\end{aligned}
\tag{4.1}
$$

The reference 'manganite model' $H_{ref}$ involves the nearest neighbour hopping of $e_g$

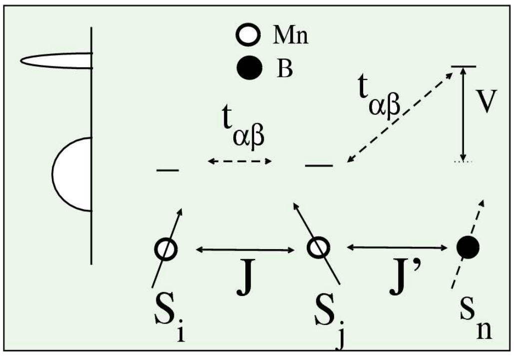

Figure 4.4: Energy levels of the B and Mn ions and the couplings between Mn-Mn and Mn-B. We show a schematic density of states at the left highlighting the primarily Mn band and the broadened B level.

electrons with amplitude $t^{ij}_{\alpha\beta}$, Hunds coupling $J_H$, AF superexchange $J$ between Mn spins, and Jahn-Teller (JT) interaction $\lambda$ between the electrons and the phonon modes $\mathbf{Q}_i$. The stiffness of the JT modes is $K$. We will generally not consider A-A′ cation disorder in $H_{ref}$ but demonstrate towards the end of the chapter that our results are robust to the presence of weak 'A site' disorder. The sites $\mathbf{R}_i, \mathbf{R}_j$ and operator $c, c^\dagger$ refer to Mn locations, and $\mathbf{S}_i$, *etc*, are Mn spins.

The local physics of the B ions is contained in $H_{imp}$ (we have taken electron-phonon coupling to be zero at impurity site but the $J_H$ at impurity site is usually same as the other sites) where $\mathbf{R}_n$ refers to the B locations and the operators $d, d^\dagger$ refer to the B ion $e_g$ states at an energy $V$ above the center of the Mn band. The sites $\mathbf{R}_n$ are random, with only the constraint that two B dopants are not nearest neighbours, to minimize electrostatic repulsion. We have done calculation without this interaction as well, and except for certain dopants on the CE phase it makes no difference to our results.

The coupling $H_{coup}$ between the B ion and the neighbouring Mn involves $(i)$ $e_g$ hopping matrix elements $t_{\alpha\beta}$, which we keep the same as between the Mn, $(ii)$ for magnetic B ions, a superexchange coupling $J'$ between the B moment $\mathrm{s}_n$ and the neighbouring Mn moments, and $(iii)$ a nearest neighbour coulomb repulsion $V_c$ between the B dopant and the neighbouring Mn. The total charge $q_j$ on the Mn ion is $4 - n_j$, where $n_j$ is the $e_g$ occupancy, and $q_n$ is the (fixed) B ion valence. Fig-4.4 is a schematic, showing the relevant levels on Mn and B, and the coupling between these ions.

The overall carrier density is controlled through the chemical potential introduced

| V and J′ | Dopant | Character |
|---|---|---|
| V=5, J′=0.00 | Ga/Mg like dopant | Non-Magnetic |
| V=5, J′=0.05 | Fe like dopant | Magnetic |
| V=5, J′=0.20 | Cr like dopant | Magnetic |
| V=1, J′=0.00 | Ni like dopant | Magnetic |

Table 4.1: Various parameters $V$ and $J'$ in our model which we will use in our calculations.

via: $-\mu(\sum_{i\alpha\sigma} c^{\dagger}_{i\alpha\sigma} c_{i\alpha\sigma} + \sum_{n\alpha\sigma} d^{\dagger}_{n\alpha\sigma} d_{n\alpha\sigma})$. We use the standard limit $J_H/t \gg 1$, and set $K = 1$. In studying magnetic field effects we will use a coupling $H_{mag} = -\mathbf{h}.(\sum_i \mathbf{S}_i + \sum_n \mathbf{s}_n)$, where $\mathbf{h} = \hat{z}h$ is the applied field. We treat all spin and phonon degrees of freedom as classical [87, 88], and measure all energies in units of the Mn-Mn hopping $t$.

The Mn-Mn superexchange in the model is $J = 0.1$, *i.e*, $JS^2/t = 0.1$. This is somewhat larger than the actual value in the manganites but is dictated by our use of $J_H/t \to \infty$ which overestimates the FM exchange.

While the impurity parameters for a particular dopant in a specific manganite host should be estimated from *ab initio* density functional calculations, we have only used rough experimental estimates. However, we calculate a whole range of physical properties to check the validity of our assumption vis-a-vis the experiments. Below is our choice of parameters to characterise the typical B dopants in the manganites.

- For 'Fe like' dopants we have taken $J' = 0.05$ (weak superexchange) and $V = 5$.
- We use $J' = 0$ and $V = 5$ for non-magnetic dopants like Ga or Al.
- For 'Ni like' dopants experiments suggest a *ferromagnetic* coupling to neighbouring Mn. We have used a small $J'$ and small $V$ to ensure that the double exchange ferromagnetism between Ni and Mn remains intact.
- The moment of doped Cr apparently aligns antiferromagnetically to neighbouring Mn, so we have taken $J' = 0.2$ and $V = 5$.

We have taken $V_c = 0.1$ or $-0.1$ [101, 102] between dopant B site and neighbouring Mn depending on the valence of dopant. For $4+$ $(3+)$ dopant we have taken $V_c = -0.1t$

$(0.1t)$ so that Mn ions with valence state $3+$ $(4+)$ sit next to $4+$ $(3+)$ dopant with greater probability. For $2+$ dopant we have considered $V_c = 0.1$. Although one should include Coulomb repulsion between Mn sites themselves and do a self consistent calculation, we have avoided that for computational simplicity. We will discuss more about impact of nearest neighbour Coulomb repulsion for specific B site doping wherever it is relevant. Except for insulating states, the use of $V_c$ makes no difference to our qualitative results.

We use a Monte Carlo (MC) technique based on the 'travelling cluster approximation' (TCA) [97]. It allows ready access to system size $\sim 40 \times 40$ using a moving cluster of size $8 \times 8$, and handles disorder more efficiently. The method, and the associated transport calculation, has been extensively benchmarked and used successfully in several studies [77, 78, 79]. We discuss these in the Appendix.

## 4.5 Doping a ferromagnetic metal

We discussed some recent experiments in Chapter.2 on doping a ferromagnetic metal. These studies [68, 69, 70] reveal that suitable B dopants can convert the FM-M to an insulator with nanoscale charge order. The rise in resistivity with B doping is dramatic. For example, the change in resistivity with 5% Fe doping in $Sm_{1-x}Sr_xMnO_3$ at $x = 0.4$ is huge, almost a factor of $10^8$ [70]. Manganites with larger bandwidth, *e.g*, LSMO and LCMO also show a rise in resistivity, albeit weaker for the same dopant concentration. It is puzzling that even impurities with the same valence, for example Fe and Cr (both supposed to be $3+$ dopants) have different effects when doped into the same ferromagnetic manganite.

### 4.5.1 Nonmagnetic $2+$ dopants

For our parameter choice, $x = 0.40$ is a a ferromagnetic metal, but in proximity to the $x = 0.50$ CE charge ordered insulator. Following the principle in Chapter.3, it is interesting to explore B dopants which drive the hole concentration of the $x = 0.40$ state into the PS window and towards $x = 0.50$. In this chapter we take the correct valence change into consideration. For the magnetic dopants, the magnetic interactions will also have an impact on the resulting state, but, to start with, let us consider non-

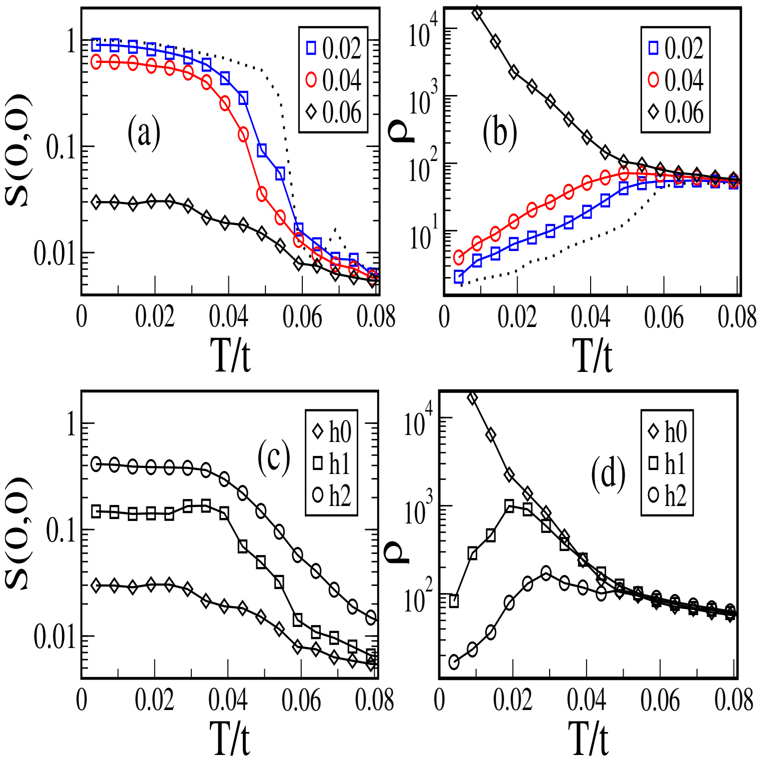

Figure 4.5: Temperature and field dependence of resistivity and the ferromagnetic peak in the structure factor for a 2+ non-magnetic (Mg like) dopant, $V = 5$, $J' = 0$ on the $x = 0.40$ FM-M. (a) FM feature in $S(\mathbf{q})$. (b) $T$ dependence of resistivity for different $\eta$. In (a) and (b) the dotted line is for the reference state, the $x = 0.40$ FM-M. In (c) and (d) we show the field response (h0 = 0, h1 = 0.002, h2 = 0.005) of the FM peak and the resistivity for $\eta = 0.06$.

magnetic $2+$ dopants. This will illustrate the 'valence change' effect.

Dopants with valence $\leq 3+$ shift the effective hole concentration $x_{eff}$ to a higher value. Doping $2+$ ions on the $x = 0.40$ state generates $x_{eff}$ that lies in the phase separated region between $x = 0.40$ and $x = 0.50$. Once the hole density lies in the PS window, the system will tend to phase separate into FM-M and AF-CO-I domains, whose pattern is controlled by the (random) B ion locations.

Fig-4.5(a) shows the ferromagnetic peak in the structure factor for different doping levels $\eta$. The extent of FM order at low temperature decreases slowly as $\eta$ increases and then drops abruptly below 0.05 at $\eta \sim 0.06$. Fig-4.5(b) shows the resistivity for the corresponding $\eta$ as in panel (a), and we observe a metal-insulator 'transition' between $\eta = 0.04$ and $0.06$ at low temperature. The dotted lines in Fig-4.5(a) and (b) shows the

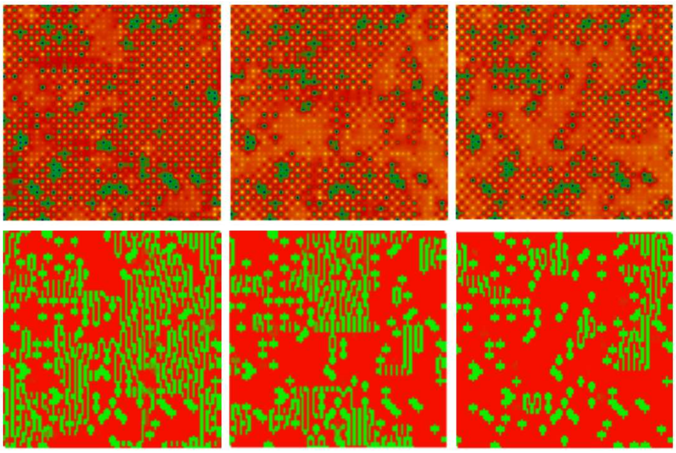

Figure 4.6: Non-magnetic $2+$ dopant on the FM-M, dopant concentration is $\eta = 0.06$. Top row: density field $n_{\mathbf{r}}$, bottom row: nearest neighbour $\mathbf{S}_i.\mathbf{S}_j$, from MC snapshots. The three columns are for applied magnetic fields $h0 = 0,\ h1 = 0.002, h2 = 0.005$.

ferromagnetic peak and resistivity, respectively, for the B undoped $x = 0.40$ state.

From our calculation we observe that the AF-CO-I clusters (here the AF phase is not exactly the CE phase but mixture of CE + A-2D) tend to live in impurity free regions. For a low concentration of dopants the system adjusts and can form AF-CO-I clusters in the large impurity free regions. The critical impurity concentration, for $2+$ dopants to create an insulating state, is $\sim 6\%$. With $6\%$ doping the effective hole density on the Mn sites increases towards the CE-CO state at $x = 0.5$. Because the hole density is very close to a charge ordered insulator a large part of the system becomes AF-CO-I.

Beyond $\eta = 0.06$, FM-M regions remain disconnected from each other although there are finite FM-M regions present as shown in the Fig-4.6 (1st column). At this low dopant concentration there are relatively large patches of impurity free regions which can 'host' a CO-I (micro) phase. These CO-I domains are of course not in phase with each other, so there is no global charge order but only short range correlations.

The effects here mimic the doping of Mg, a $2+$ dopant, on the ferromagnetic metal [69]. Maignan *et al.* measured (see the Fig-4.7) the the change in resistivity with increasing Mg dopant on $Pr_{0.7}Ca_{0.1}Sr_{0.2}MnO_3$ which is ferromagnetic metal. When the Mg concentration increases to $8\%$, the system becomes insulating at low temperature. In Fig-4.7, we compare our result with the experimental data. We notice that the correct trend of doping driven MI transition is captured. The inset shows our result on the rapid rise of the $T = 0$ resistivity with $\eta$.

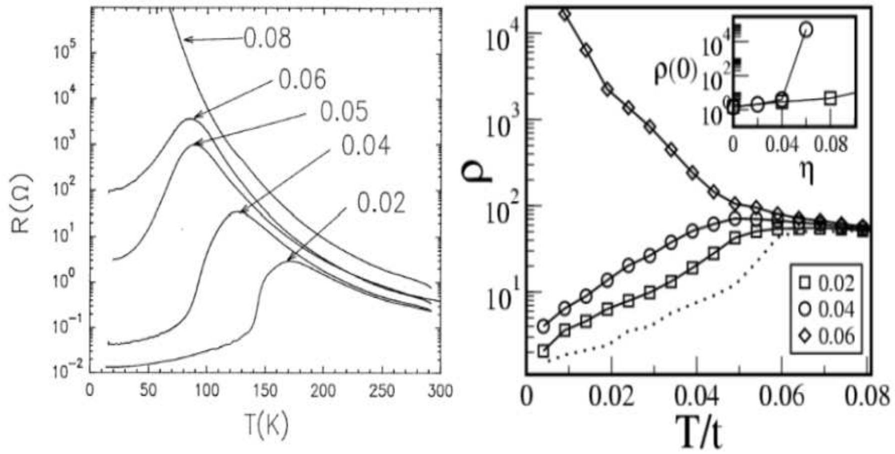

Figure 4.7: Left panel : Experimental curve from [69]: Temperature dependence of resistivity for various concentration Mg dopant on $Pr_{0.7}Ca_{0.1}Sr_{0.2}Mn_3$. Right panel: Temperature dependence of resistivity for various concentration $2+$ dopants on a FM-M ($x$ = 0.5) as in Fig-4.5 to compare with the experimental data. Inset of right panel shows the zero temperature resistivity for $2+$ dopants (circles) to compare that with $3+$ dopants (squares) for various $\eta$ value.

Having seen the zero field metal-insulator transition driven by B dopants, we next explore the effect of a magnetic field in these 'B driven' phase coexistent states. At $\eta = 0.06$, the disconnected FM-M patches strongly respond to an applied field and shows a rapid rise in the ferromagnetic peak and the conductivity. Fig-4.5(c) and (d) shows the field response at $\eta = 0.06$. In Fig-4.5(c), for a small external magnetic field the ferromagnetic peak increases, as more and more FM-M regions get connected, and leads to the metallicity shown in Fig-4.5(d). We opted to show the field response at $\eta = 0.06$ since the insulating state here is not very strong and can be easily transformed to a FM-M. At larger $\eta$ the system is still insulating but hard to metallise compared to $\eta = 0.06$.

The effect of the applied field on the spatial nature of the electronic and magnetic state is shown Fig-4.6 with snapshots from MC calculation. The density field $n_{\mathbf{r}}$ and nearest neighbour $\mathbf{S}_i.\mathbf{S}_j$ at low temperature are shown from MC snapshots in the top and bottom row respectively. At $\eta = 0.06$, and $h = 0$, CO-I regions coexist with FM-M regions. In the 1st column FM-M regions are still visible but not well connected to each other. So, at $h = 0$ the system is insulating as shown in Fig-4.5(b). At small $h$ FM-M patches get connected leading to a (poor) metal. In the bottom row the FM regions

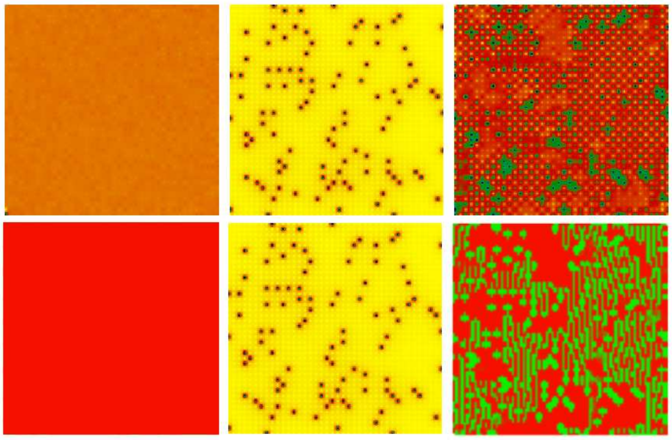

Figure 4.8: Correlation between the charge density field $n_{\mathbf{r}}$ and impurity locations at $x = 0.40$. Left: $n_{\mathbf{r}}$ in the reference FM-M at $\eta = 0$, center: location of the B ions, right: $n_{\mathbf{r}}$ in the presence of the B ions ($\eta = 0.06$, non-magnetic 2+ dopants, $V = 5$, $J' = 0$). The panels at the bottom (left and right) show the corresponding nearest neighbour magnetic correlations.

are at same position as the homogeneous regions in the top row and show one to one correspondence between ferromagnetism and charge homogeneous regions.

Fig-4.8 shows the density field and magnetic correlation for a specific realisation of B dopants. The top left panel shows $n_{\mathbf{r}}$ in the reference state $(\eta = 0)$, center shows the impurity locations, and top right shows $n_{\mathbf{r}}$ in the presence of the B ions. The bottom row shows nearest neighbour $S_{\mathbf{i}}.S_{\mathbf{j}}$ for the same B ion configuration. From the results, one can infer that even with $\eta = 0.06$ and randomly distributed ions, there are large patches for the CO regions to form. Obviously with larger $\eta$ the CO domains will be more fragmented.

The density of states also shows indication of insulating behaviour. We use the DOS at Fermi level as an additional indicator to track the decrease in metallicity with increasing $\eta$. The DOS at $\epsilon_F$ tracks the metal to insulator transition with changing $\eta$ in Fig-4.9(a). The reference DOS for $x = 0.4$ is shown in Fig-4.3(a) with finite value at Fermi Level. With increase of $\eta$, the DOS at Fermi level decreases sharply around $\eta \sim 0.06$.

The low energy local DOS in the FM regions of the lattice will be finite in the FM-M regions and zero for CO regions. This may be useful to identify the FM-M and AF-CO regions via tunneling spectroscopy.

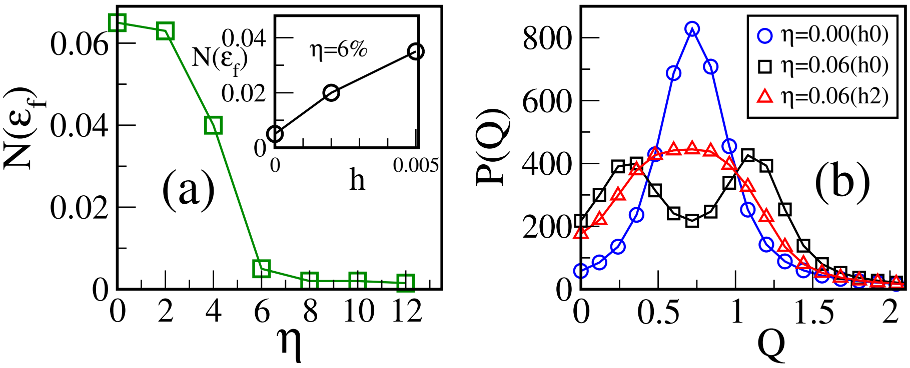

Figure 4.9: The initial state is FM-M at $x = 0.4$ and B site dopant is non-magnetic in $2+$ valence state ($V$=5, $J'$=0). (a) The variation of DOS at Fermi level with various $\eta$. (For $\eta = 0.06$, DOS at Fermi level in presence of magnetic field is also shown in the inset) (b) The P(Q) for $x = 0.4$ in clean limit and for ($\eta = 0.06$). The P(Q) structure with $\eta = 0.06$ with magnetic field $h2 = 0.005$ is also shown.

For $\eta = 0.06$, the DOS at Fermi level is shown in the presence of a magnetic field. The increase in DOS with magnetic field follows the change from insulating to metallic behaviour in the resistivity as shown in Fig-4.5(d).

Another indicator is $P(Q)$, it is bimodal for $\eta = 0.06$, shown in Fig-4.9(b). The bimodal $P(Q)$ (and subsequently measured absolute Q values in all sites) indicates that the system goes into a locally charge ordered state. $P(Q)$ loses the bimodal character on application of the magnetic field. This suggest that the system returns to homogeneous state like the parent $x = 0.4$ phase in presence of small magnetic field. The reference $P(Q)$ for $x = 0.4$ is also shown in Fig-4.9(b).

Till now we have discussed $2+$ dopants like Mg which are non-magnetic. What would be the effect of $3+$ dopants, which should also increase $x_{eff}$ like the $2+$ dopants? Non-magnetic dopants with $3+$ valence lead to $x_{eff}$ in phase separation window but the change in resistivity is not that dramatic at low $\eta$ and the metal-insulator transition occurs at a large impurity concentration, $\eta \geq 0.12$, unlike smaller critical $\eta$ for $2+$ dopant.

The insulating behaviour at larger $\eta$ is due to large amount of impurity scatterers present and not just due to valence change driven charge order. The slower change in valence compared to $2+$ dopants is the principal difference between these two cases. The inset of Fig-4.7(b) shows the low temperature resistivity variation with different $\eta$

value for dopant with $3+$ and $2+$ valence state. The rise in resistivity at low temperature for $2+$ dopants is much faster than the $3+$ dopants in this case. To our knowledge there is no experimental result yet where $2+$ dopants have been compared with $3+$ dopants on the manganite. However, via bandwidth variation one can tune the low temperature resistivity for $3+$ dopants. We discuss details of this in the next section.

### 4.5.2 Magnetic $3+$ dopants

Recent experiments have explored Fe doping into the FM-M state for manganites with various bandwidth. Fe doping is not new and one of the early experiments was on Fe doping in LCMO at $x = 0.40$ in 1997 [68]. The recent work with bandwidth [70] variation in the underlying manganite has yielded a large body experimental data whose trend is unexplained.

Our description of a Fe like dopant involves smaller superexchange and large $V$ ($J'$= 0.05 and $V = 5$). We start our calculation with $\lambda = 1.6$. As shown in Fig-4.10(a), the low temperature resistivity increases with doping but only moderately upto $\eta = 0.12$. By $\eta = 0.16$ the system is essentially insulating. Just as we showed for $2+$ dopants, CO-I patches form with few percent of doping but not throughout the sample. This ensures that the FM-M regions remain connected upto a larger $\eta$ value and the system remains conducting. By $\eta = 0.16$, most of the sample is in a nanoscale CO state and goes insulating at low temperature.

We now discuss the bandwidth dependence of these effects. To mimic bandwidth variation, as previously we change $\lambda/t$ (keeping other electronic parameters fixed). With decreasing bandwidth, the stability of FM-M phase at $x = 0.4$ decreases (the $x = 0.4$ state goes insulating at $\lambda = 1.7$). We ensured that the $\lambda$ value we used retains a FM-M at $x = 0.40$. With increase in $\lambda$, the strength of charge order in the neighbouring $x = 0.5$ CE-CO-I also increases.

We varied the dopant concentration for $\lambda = 1.65$ and $\lambda = 1.68$. Around $\lambda = 1.70$, the system is not a FM-M anymore and we have not considered any value beyond 1.68. At $\lambda = 1.65$, as shown in Fig-4.10(b) the FM-M goes insulating at much lower $\eta$. With $\lambda = 1.68$, the $\eta$ needed to get an insulating state is much lower as shown in the Fig-4.10(c). The critical $\eta$ for the MIT are as follows: $\eta_c \sim 0.16$ for $\lambda = 1.60$ while it is only $0.06$ for $\lambda = 1.68$. This indicates that with decrease in bandwidth (*i.e*, increase in $\lambda$ in

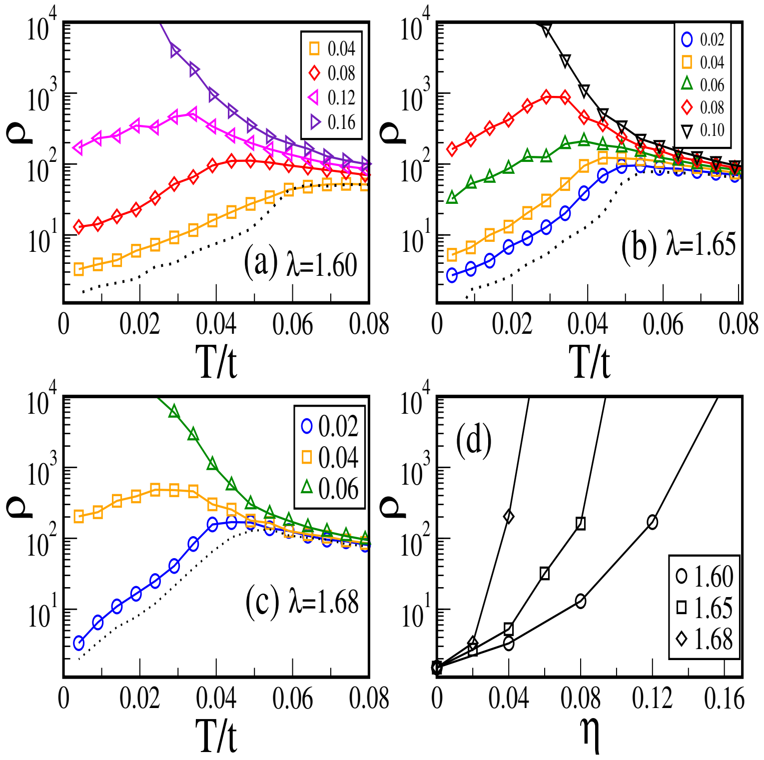

Figure 4.10: (a), (b), (c) : Temperature dependence of resistivity for $3+$ non-magnetic B site dopant ($V$=5, $J'$=0.05 which is Fe like dopant) at reference state $x$=0.40 for different value of $\lambda$ indicated in the panels. (d) low temperature resistivity plotted against $\eta$ for three different value of $\lambda$

our calculation) it is easier to turn FM-M to an insulator. That is what experimentally observed recently [70].

With variation in bandwidth from LaSrMnO$_3$ to SmSrMnO$_3$ at $x = 0.4$, when doped with Fe, the minimal $\eta$ required changes from 0.18 to 0.05 (see Fig-2.7). In Fig-4.10(d), the low temperature resistivity for all three $\lambda$ are plotted for different $\eta$. The increase in the $T = 0$ resistivity is enormous, and is very strongly nonlinear in $\eta$. This is not a simple impurity scattering effect.

We also plotted the ferromagnetic peaks varying the $\eta$ for the three $\lambda$ value (1.60, 1.65, 1.68) in Fig-4.11. We see the same trend for $\eta$ dependence as in resistivity change. For smaller $\lambda$, a large concentration of dopants is required to kill the ferromagnetism while for large $\lambda$, the dopant concentration for same result is quite small.

We compare our result with experiment shown in the lower panel of Fig-4.11. In the experimental figure (Fe doped in the FM-M) the bandwidth of parent material de-

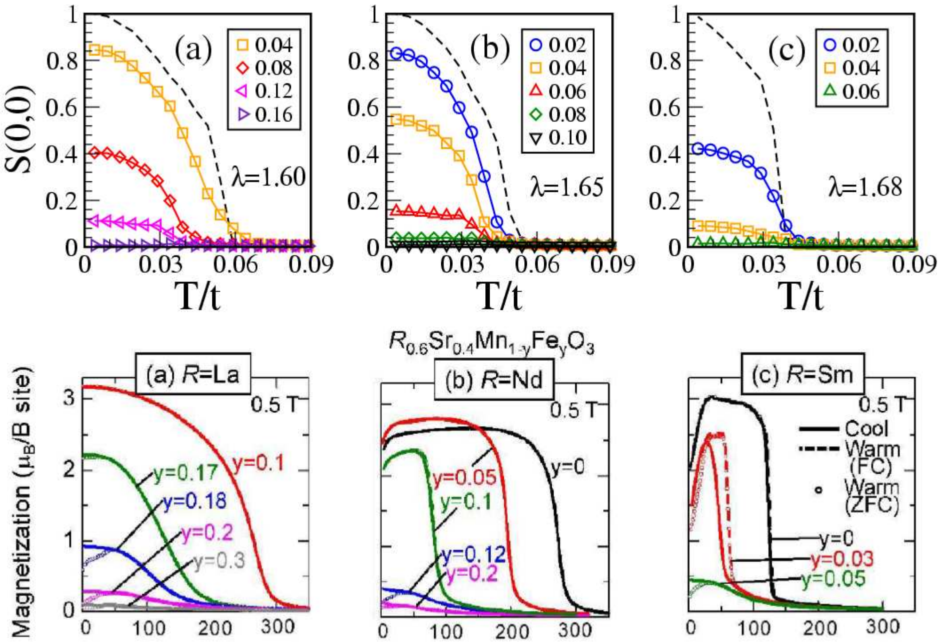

Figure 4.11: (a), (b), (c) : Temperature dependence of ferromagnetic peak for $3+$ magnetic B site dopant ($V$=5, $J'$=0.05 which is Fe like dopant) at reference state $x$=0.40 for different value of $\lambda$ indicated in the panels. Dotted line shows the respective ferromagnetic peak for parent material. Lower panel shows the Fe dopant on $A_{0.6}Sr_{0.4}MnO_3$ for A=La, Nd, Sm which varies the bandwidth of the undoped manganites.

creases from left to right. For the low bandwidth manganite (right) only $5\%$ of Fe is needed to kill the ferromagnetism while for large bandwidth material (left) $\sim 20\%$ of Fe required. Our $\lambda$ variation captures the trend of the experiment.

Dopants with $3+$ valence like Ga or Al behave more or less like Fe in the large bandwidth materials and require large impurity concentration to convert the FM-M to an insulator. On moderate bandwidth materials where few percent of Fe like dopant convert the FM-M state into a CO-I, we can compare the other $3+$ dopants like Ga or Cr. We model non-magnetic Ga with $J' = 0$ and Cr with $J' = 0.2$ and both with large $V$ as shown in Fig-4.12. Non-magnetic $3+$ dopants create an insulating state, like Fe doping, but the concentration required is larger Fig-4.12(a). However, for a Cr like dopant even with $\eta = 0.20$ the system is not quite insulating, and the the low temperature resistivity rise for large $\eta$ may be the result of strong potential scattering. This is not genuine FM-M + CO-I mixed state. When the resistivity is compared for $\eta = 0.08$ for all three $J'$ ($J' = 0.05$ for Fe like dopant, $J' = 0$ for Ga like dopant, $J' = 0.20$ for Cr like dopant)

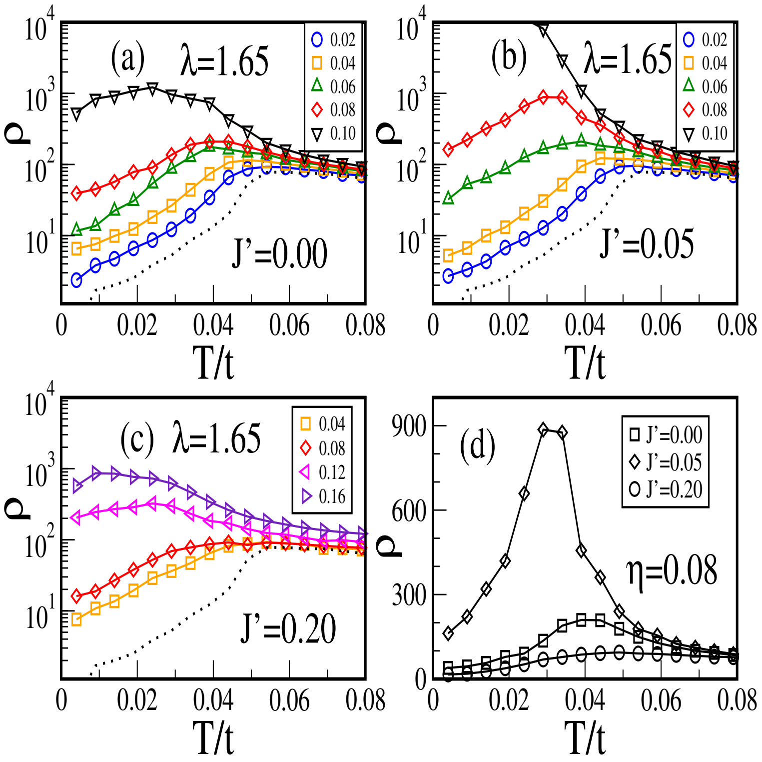

Figure 4.12: Temperature dependence of resistivity with $3+$ dopants at reference state $x$=0.40 and $\lambda = 1.65$ (a) $J'$=0.00 (b) $J'$=0.05 (c) $J'$=0.20 and $V$=5 used in all three case. In (d) with $\eta = 0.08$, the resistivity compared for three values of $J'$ used in (a), (b), and (c)

used, the MI transition at intermediate temperature is quite visible only for $J' = 0.05$ and we also observe that the change in transition temperature for $J' = 0.05$ is much faster than other two $J'$ we have taken. Qualitatively Fe doping on manganites shows the same features and MI around $T_c$ is much more prominent as compare to Ga and Cr [71]. The experimental result from experiments is shown in Fig-2.5.

### 4.5.3 Nonmagnetic $4+$ dopants

With $2+$ and $3+$ dopants, we are able to explain the MI transition with increase in dopant concentration, when the FM-M is doped with a few percent of Fe like dopants and lead to emergence of CO-I correlations. Both $2+$ and $3+$ dopants push the hole density towards phase separation window between $x = 0.4$ and $x = 0.5$. With that in mind, $4+$ dopants behave oppositely and shift the $x$ deeper into the FM-M region. As shown in Fig-4.1, FM-M extends from $x = 0.42$ to $x = 0.3$. With $x_{eff}$ still in the FM-M

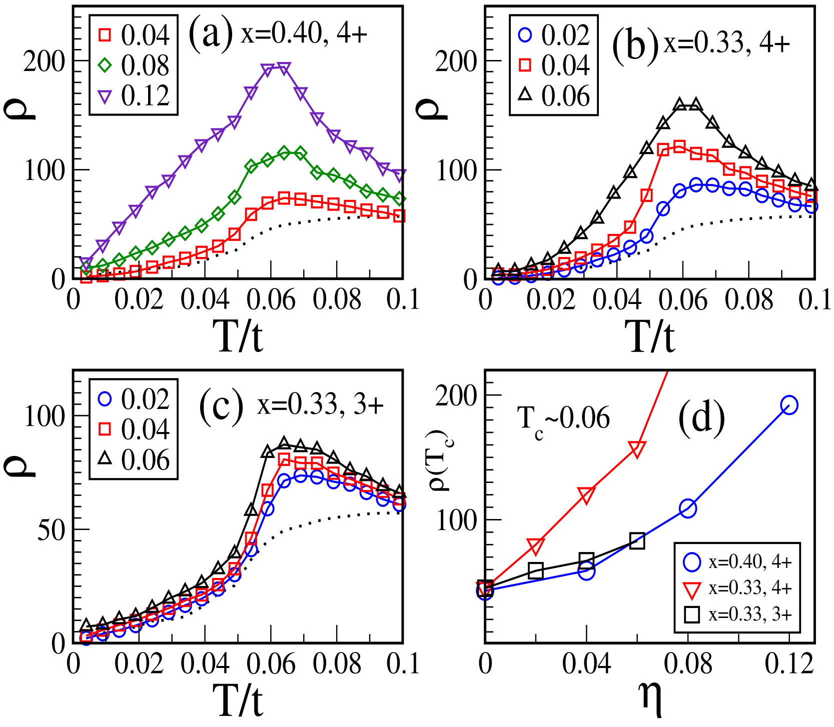

Figure 4.13: Temperature dependence of resistivity with $4+$ non-magnetic B site dopant ($V$=5, $J'$=0, Ti like dopant) at reference state (a) $x$=0.40 and (b) $x$ = 0.33. In (c), temperature dependence of resistivity with $3+$ non-magnetic B site dopant ($V$=5, $J'$=0, Ga like dopant) at reference state $x = 0.33$. In (d), resistivity at T $\sim$ $T_c$ is plotted for all three cases (a), (b) and (c).

window the ferromagnetism and metallicity is only weakly affected by $4+$ dopants. We use non-magnetic $4+$ dopants with $J' = 0$ and large $V$ which is same as any other $2+$ or $3+$ valence non-magnetic dopant used earlier but correct shift in $x_{eff}$ taken into account for $\alpha = 4$. As shown in Fig-4.13(a), when doped with $\eta = 0.12$ and even more the metallicity is still intact and the only change is in resistivity for intermediate temperature.

What about hole density which is close to PS window between FM-M and FM-I, close to $x = 0.3$? Doping $4+$ dopant close to $x = 0.3$ will create CO correlations appropriate to $x = 0.25$. Fig-4.13(b) shows the resistivity change with $4+$ dopants at $x = 0.33$ which is close to the 'lower edge' of the FM-M window. We also plot the change in resistivity for different concentration of same dopants on a FM-M at $x = 0.4$. The change in resistivity at intermediate temperature (around $T_c$) is much more prominent with low $\eta$ for $x = 0.33$ when we compare it with the $x = 0.4$ case (shown in Fig-4.13(d)). In

Fig-4.13(c), we calculated the resistivity change with temperature for $3+$ dopants at $x = 0.33$ to compare the result with $4+$ dopants. The change in resistivity is very slow for $3+$ dopants compared to $4+$ dopants (at $x$ = 0.33). This is because the effective hole density, $x_{eff}$, changes towards the middle of ferromagnetic window for $3+$ dopants (see Fig-4.1), rather than pushing it to the PS window in between FM-M and FM-I.

With suitable B site dopant on a FM-M manganite at $x = 0.33$ the resistivity can be enhanced several fold. The change in resistivity at intermediate temperature arises from the proximity to a CO-I phase. In fact Ti doping on LSMO at $x = 0.3$ [75, 76] shows insulating behaviour, while the change in resistivity for Al doping [76] is very slow. The valence of the dopant plays a key role in this difference. $3+$ dopants push the hole density deeper into the FM regions while $4+$ dopants push the hole density towards the low $x$ ferromagnetic *insulator*.

## 4.6 Doping a ferromagnetic charge ordered insulator

There is a FM-I phase found in real manganites although the window of hole doping varies between manganites. For example La$_{1-x}$Sr$_x$MnO$_3$ has a FM-I phase phase from $x \sim 0.10 - 0.25$, while Pr$_{1-x}$Ca$_x$MnO$_3$ has a FM-I phase from $x \sim 0.15 - 0.30$. Because of A site disorder the FM-I has only short range charge order. A charge ordered state at $x = 0.25$ had indeed been suggested earlier by Hotta *et al.* [103].

At $x$=0.25, the underlying clean phase is ferromagnetic in our calculation, but unlike the window $x \sim 0.30 - 0.42$ it is a charge ordered insulator. We have discussed this state earlier. The CO pattern is not a checkerboard. The state is stable only at a single hole density and is separated from neighbouring phases by windows of phase separation. To the right of it, at higher $x$, we have the FM-M starting at $x = 0.3$, while at lower $x$ we have the $x = 0$ orbital ordered FM-OO-I state. Following the general principle, dopants that increase $x_{eff}$ may be able to metallise the FM-CO-I.

### 4.6.1 Nonmagnetic $2+$ or $3+$ dopants

With $2+$ dopants like Mg or Zn, $x_{eff}$ shifts towards large $x$. The PS window between the FM-CO-I and FM-M is relatively narrow and a low dopant density quickly generates FM-M correlations. As shown in Fig-4.14(a), small doping like $\eta = 0.02$ creates

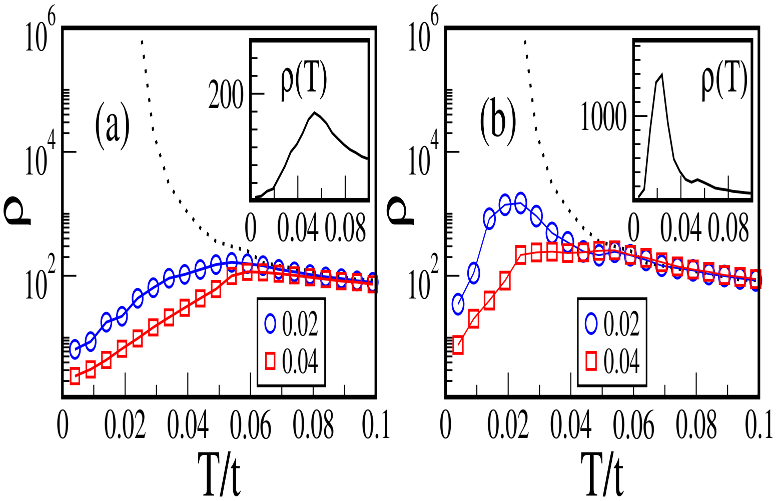

Figure 4.14: Temperature dependence of $\rho(T)$ for dopants on the $x = 0.25$ state. (a). 2+ non-magnetic dopants (Mg like), and (b). 3+ non-magnetic dopants (Ga like). We used $V = 5$, $J' = 0$ in both cases. Inset in both (a) and (b) shows the resistivity change in the linear scale for $\eta = 0.02$ to highlight the MI transition in the intermediate temperature. Dotted lines represent the B undoped state.

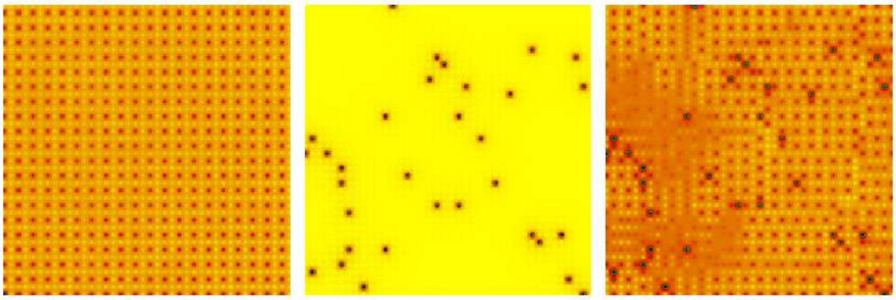

Figure 4.15: The density field $n_{\mathbf{r}}$ at low $T$ and impurity locations for $x = 0.25$. $\eta = 0.02$, 2+ non-magnetic dopants, $V = 5$, $J' = 0$. Left: $n_{\mathbf{r}}$ in the reference state ($\eta = 0$), center: location of the B impurities, right: $n_{\mathbf{r}}$ in the presence of the B ions.

FM-M clusters with $x \sim 0.3$ and promotes a percolative metal. Since both the undoped and the B doped states are ferromagnetic an external field does not have much effect in this case. Fig-4.14(b) shows the resistivity for 3+ dopants, they have an effect similar to 2+ dopants. The insets in Fig-4.14(a)-(b) show the linear scale to highlight the resistivity peak around metal-insulator transition for $\eta$=0.02. The resistivity peak for 3+ dopants is much more prominent. The spatial snapshots reveal that on B doping FM-M correlations show up in 'impurity free' regions as shown in Fig-4.15

The DOS at Fermi level indicate the insulator to metallic crossover with increasing

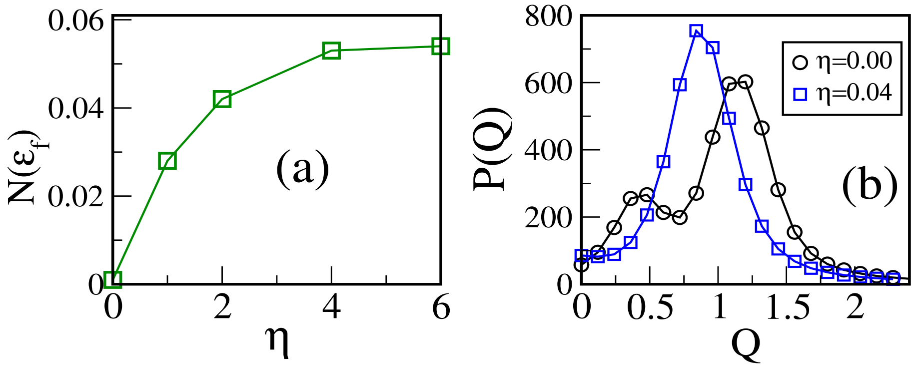

Figure 4.16: DOS at $\epsilon_F$ and $P(Q)$ at $x = 0.25$. (a) The variation of DOS at Fermi level with increasing $\eta$ for 2+ non-magnetic dopants. (b) The $P(Q)$ for $x = 0.25$ in clean limit and for $\eta = 0.06$. $P(Q)$ changes to a one peak structure, typical of a homogeneous phase by the time $\eta = 0.04$.

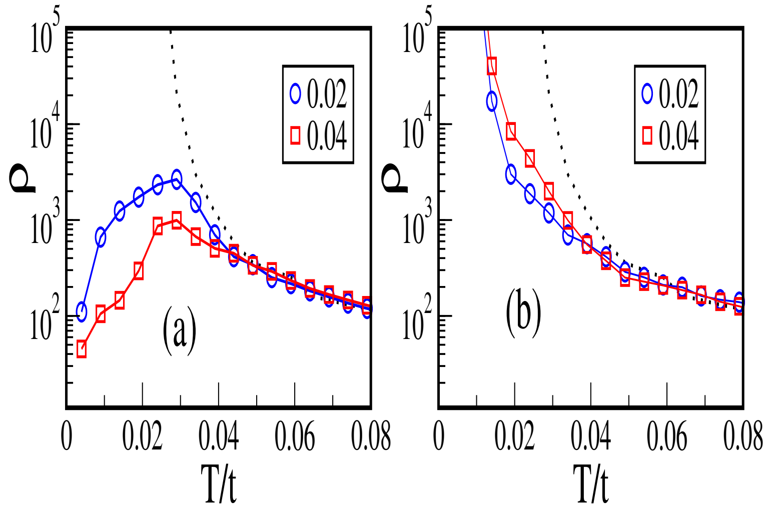

Figure 4.17: Temperature dependence of $\rho(T)$. (a). For 3+ magnetic dopants with $V = 5$, $J' = 0.05$ (Fe like) and (b). $V = 5$, $J' = 0.20$ (Cr like) on $x = 0.25$.

$\eta$. Fig-4.3(a) showed the DOS for $x = 0.25$ in the clean FM-CO-I. Fig-4.16(a) shows DOS at Fermi level with increasing concentration of B site dopants (2+ dopant, $V = 5$, $J' = 0$). With increase in $\eta$, the DOS at Fermi level increases and is significant already at $\eta = 0.02$. The $P(Q)$ distribution is shown in (b) for $\eta = 0.04$ and shows a one peak structure rather than two peaks of the clean FM-CO-I. Once again one peak structure of $P(Q)$ is consistent with homogeneous metallic behaviour.

### 4.6.2 Magnetic $3+$ dopants

$3+$ dopants with small superexchange ($J' = 0.05$, $V = 5$) (like Fe) shows a resistivity change similar to $3+$ non-magnetic dopants. Fig-4.17(a) shows the resistivity with such dopants. At large $J'$, however, there is no such effect in the resistivity as shown Fig-4.17(b). We believe that large $J'$ leads to reconstruction of the magnetic state and 'shifts' the system towards the FM-OO-I ($x$=0.0), and the B doped state remains insulating. We will discuss these effects in the next chapter.

## 4.7 Doping the CE charge ordered insulator

### 4.7.1 Nonmagnetic 4+ dopants

Introducing $4+$ or $5+$ dopants like Ti, Ru, Rh on the half filled CE-CO-I induces both ferromagnetism and metallicity [61, 56, 64, 65, 69]. From our expression for $x_{eff}$, we can see that these dopants lead to a decrease in the effective hole density and pushes the system to a regime of phase separation between the CE-CO-I and the FM-M. A simple version of this considered in Chapter.3. In that simple model we had kept $x$ fixed at $0.50$ and introduced a low concentration of strongly repulsive sites. When the correct valence change is taken into account the IM crossover effects that we observed there can get amplified. The coexistent state that emerges consists mainly of FM-M regions with local density $x \sim 0.4$ and AF-CO-I with $x \sim 0.5$. In what follows we take $V = 5$ and $J' = 0$ for non-magnetic dopants with $4+$ valence.

Fig-4.18 shows the ferromagnetic peaks and resistivity for $4+$ dopants with various $\eta$ values at half filling. Fig-4.18 shows the ferromagnetic feature with increase in $\eta$. Dotted line shows that the ferromagnetic peak which is insignificant in the undoped system. With increase in $\eta$, the ferromagnetic peak increases. With increasing $\eta$ the effective hole doping gets closer to the FM-M regime and the FM peak in the structure factor is quite strong. In Fig-4.18(b) the change in resistivity is shown for corresponding $\eta$ values. From a strong insulator, shown as dotted line, the system goes to a metal for $\eta \sim 0.08$.

These results explain the insulator to metal transition with Rh or Ru like dopants in CE-CO-I and our results do not change even in the presence of nonzero $J'$, i.e, magnetic character in the B dopant. The same change for $J' = J$ was discussed in Chapter.3. To

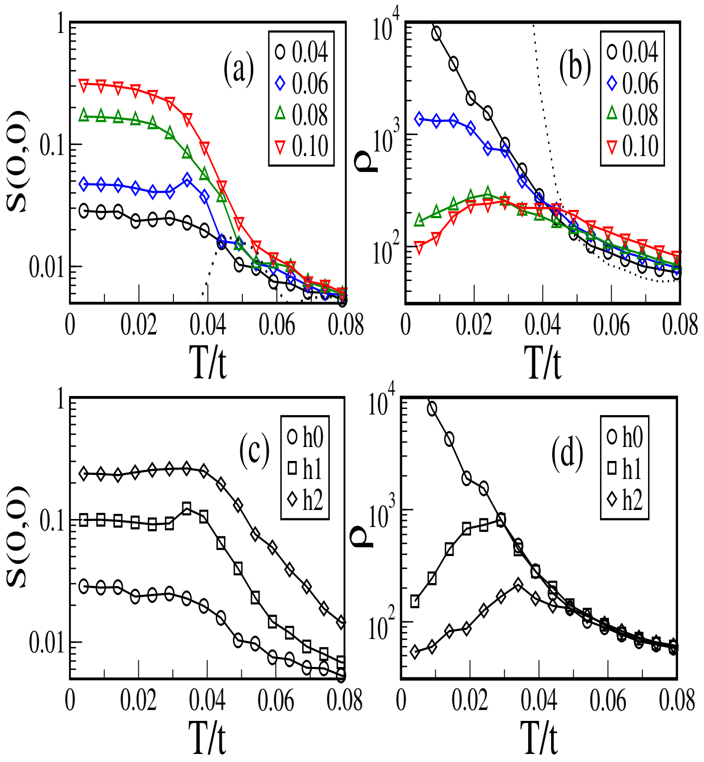

Figure 4.18: Temperature and field dependence of resistivity and ferromagnetic peak for $4+$ non-magnetic dopants (Ti like, say) on $x = 0.50$ using $V = 5$, $J' = 0$. (a). FM peak in $S(\mathbf{q})$, (b). $\rho(T)$ for different $\eta$. In (a) and (b) the dotted line is for the undoped reference state. (c) and (d) shows the field response (h0 = 0, h1 = 0.002, h2 = 0.005) at $\eta = 0.04$ in the ferromagnetic peak and the resistivity.

compare our result with experiment we plotted the resistivity variation with temperature for different $\eta$ and kept $J' = J = 0.1$ in Fig-4.19. Our results show the decrease in resistivity with increasing $\eta$ and capture the qualitative trends in the experimental data, right panel Fig-19. We have not shown data at larger concentration but for $\eta > 0.12$, the large disorder leads to a rise in the low temperature resistivity.

To see the effect of external magnetic field, we choose $\eta$ such that the induced FMM patches are still unconnected. At $\eta = 0.04$ a modest applied field can connect the clusters creating a metallic state. With external field of 0.002, the ferromagnetic peak is order of 0.1 and the system shows metallic behaviour at low temperature. So with a small magnetic field one can tune this B doped insulator to a metal as shown in Fig-4.18, while a large magnetic field is required to metallise the undoped CE-CO-I. As mentioned before, B dopants make it easy to realise colossal magnetoresistance.

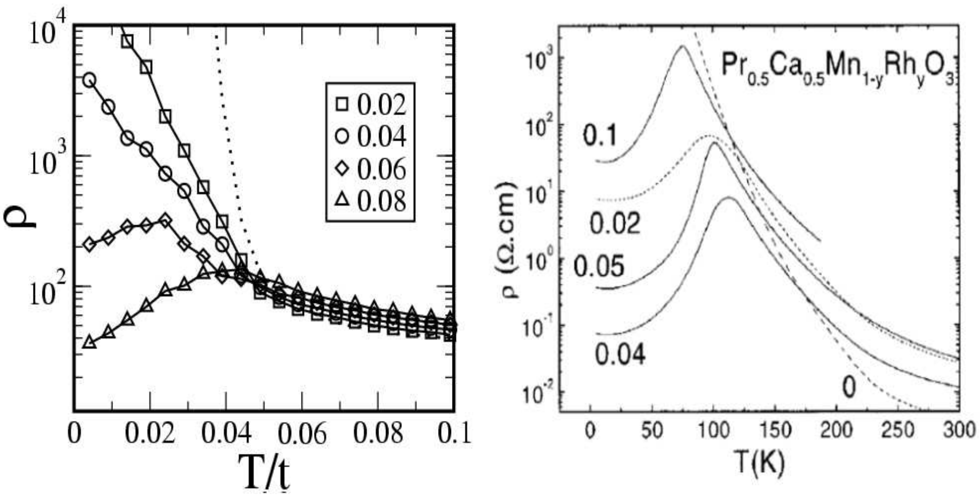

Figure 4.19: Left panel: Temperature dependence of resistivity for $4+$ dopants (V=5, $J' = J = 0.1$) on $x = 0.50$. Right panel : Temperature dependence of resistivity for various concentration of Rh doping on $\text{Pr}_{0.5}\text{Ca}_{0.5}\text{MnO}_3$.

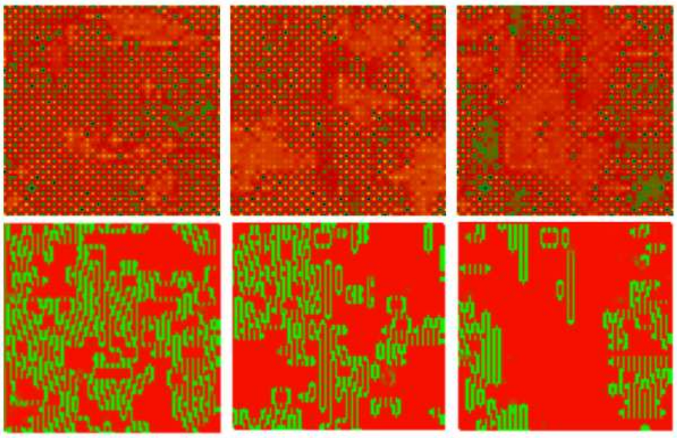

Figure 4.20: Top row: density field $n_{\mathbf{r}}$ at low temperature and bottom row: nearest neighbour $\mathbf{S}_i.\mathbf{S}_j$ from MC snapshots in small applied magnetic field with $(\eta = 0.04)$ for $4+$ dopants as in Fig-4.18 at reference state $x$ = 0.50. Left to right: $h0 = 0.000,\ h1 = 0.002,\ h3 = 0.005$.

Fig-4.20 shows the ferromagnetic correlations for $\eta = 0.04$ for applied magnetic field. We have shown the density field $n_{\mathbf{r}}$ and nearest neighbour $\mathbf{S}_i.\mathbf{S}_j$ at low temperature from MC snapshots in a small magnetic field. The applied field increases from left to right. FM regions in the bottom row map on to CD areas in the top row, and are not connected to each other in absence of applied magnetic field (1st column). With an

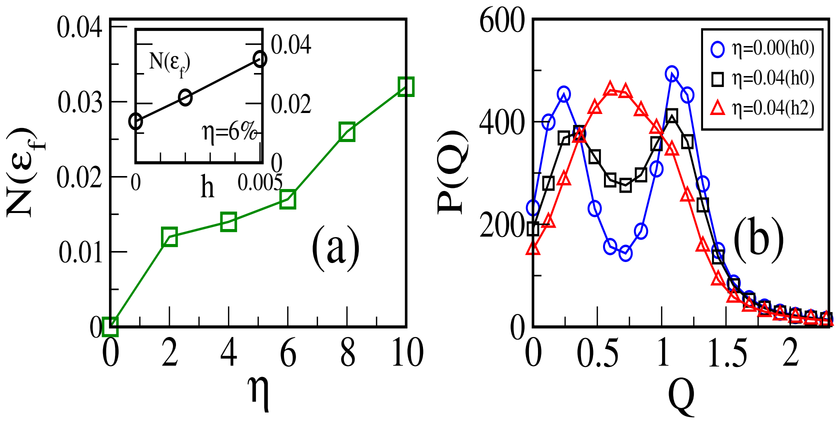

Figure 4.21: DOS at $\epsilon_F$ and $P(Q)$ in the doped $x = 0.5$ state with $4+$ dopants as in Fig-4.18. (a).The variation of DOS at Fermi level with various $\eta$. (For $\eta = 0.04$, DOS at Fermi level in presence of magnetic field is also shown in the inset) (b).The $P(Q)$ for $x = 0.5$ in clean limit and for $\eta = 0.08$. The two peak structure $P(Q)$ changes to a single peak structure by the time $\eta = 0.08$.

applied field as low as 0.002 and 0.005 the FM patches get connected, as seen in 2nd and 3rd column, and turn the system metallic.

The DOS at Fermi level indicates the insulator to metal crossover with low concentration of dopant. Fig-4.3(a) shows DOS for $x$=0.50 for clean limit which is CE-CO-I. We use the DOS at Fermi level as indicator to show the increase in metallicity with increase in dopant concentration, tracking the I-M transition. It tracks the insulator to metal transition with increase in the concentration of $4+$ non-magnetic dopants. Fig-4.21(a) shows DOS at Fermi level with different concentration. Reference DOS for $x = 0.5$ is shown in Fig-4.3(a) with zero value at Fermi Level. With increase of $\eta$, the DOS at Fermi level increases and goes to a finite value. For $\eta \geq 0.06$ the increase in DOS alongwith $\rho(T)$ indicates metallicity. For $\eta = 0.04$, the DOS at Fermi level is shown in the presence of a magnetic field (in the inset) and shows an increase by more than a factor of two. This increase in DOS with magnetic field indicate the change from insulating to metallic behaviour as we shown in Fig-4.18(d). The other indicator, $P(Q)$, is bimodal for $\eta = 0.04$ shown in (b) and becomes single peaked in the finite field case. The reference $P(Q)$ for $x = 0.5$ is also shown in (b).

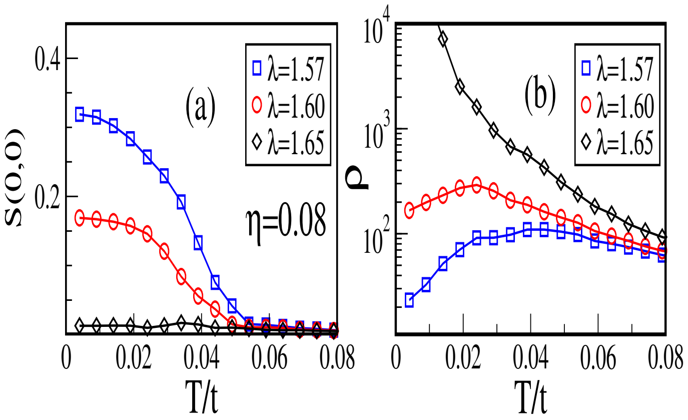

Figure 4.22: Temperature dependence of magnetic peak and resistivity for $4+$ dopants as in Fig-4.18 (V=5, J′=0 which is Ti like dopants) at reference state $x$=0.50 for different value of $\lambda$ indicated in the figure.

### 4.7.2 Dependence on manganite bandwidth

For Fe doping in a FM-M we had discussed the effect bandwidth variation on the MI transition. A similar scenario holds here as well. In Fig-4.22, we shows the ferromagnetic peak and resistivity for different $\lambda$ at $\eta = 0.08$. The experimental parallel is in Fig-2.13 and 2.8.

### 4.7.3 $3+$ dopants

Dopants with valence less than equal to $3+$ obviously change $x_{eff}$ but in a opposite direction to that of $4+$ dopants. With $3+$ doping $x_{eff}$ lies in the PS window between the CE-CO-I ($x = 0.5$) and A-2D phase (at $x = 0.55$). There is no ferromagnetic state in this doping window. Surprisingly, Cr and Ni, with valence state $3+$ manage to create a ferromagnetic state! We will see in the next chapter that 'magnetic reconstruction' takes over to modify the underlying CE type order and overrides the valence change effect.

## 4.8 Robustness of the phase coexistent state

### 4.8.1 A site disorder

Till this point we have neglected A site disorder when we considered B site doping. In this section we quantify the effect of A site disorder in the B doped state. Most B doping experiments are done on systems with weak A site mismatch, e.g, LCMO. Nevertheless it may help to understand the effect of this perturbation.

We reanalyze B site doping with A site disorder, for a non-magnetic $2+$ dopant on the $x = 0.4$ FM-M. Fig-4.23 shows the disorder averaged charge structure factor $D(\mathbf{q})$ at A site disorder $\Delta = 0,\ 0.1,\ 0.2,\ 0.3$ (A site disorder modelling is explained in Chapter.3). The bottom left corner in each panel is $\mathbf{q} = \{0, 0\}$, and the top right corner is the key $\mathbf{q} = \{\pi, \pi\}$. There is noticeable broadening of the CO peak at $\{\pi, \pi\}$, *i.e*, the reduction in CO correlation length, with increasing $\Delta$. For reasonable A site disorder like $\Delta = 0.1$, there is hardly any change in CO peak and our B site calculation is valid when such disorder is present in the manganites.

Fig-4.24(a) shows the D$\{\pi, \pi\}$ peak in the B doped FM-M for increasing A site disorder. The suppression parallels the destruction of CO in the neighbouring $x = 0.5$ CE-CO state, which appears as a player in the B induced phase coexistent state, Fig-4.24(b). By the time $\Delta = 0.2$, the CO state is converted to a nanoscale correlated state.

### 4.8.2 Coloumb effects

We used a nearest neighbour Coulomb repulsion, $V_c$ in all our calculation. However, our results do not crucially depend on this, except for the $x = 0.5$ CE-CO state. For example we have taken metal insulator transition at $x = 0.4$ with $2+$ non-magnetic dopants and show the effect of $V_c$ in Fig-4.25(a). All three values of $V_c$, 0, 0.1, and 0.2 yield similar results. This 'independence' of $V_c$ is visible for doping on the $x = 0.25$ FM-CO phase as well.

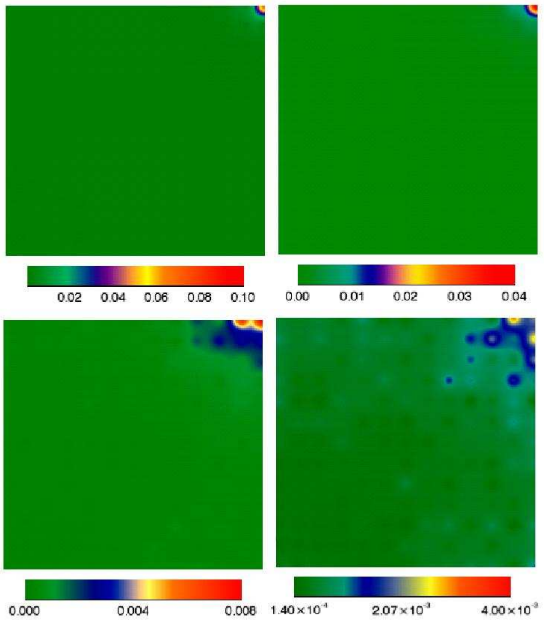

Figure 4.23: Disorder averaged charge structure factor $D(\mathbf{q})$ at $\Delta = 0,\ 0.1,\ 0.2,\ 0.3$ (left to right, top to bottom) in the B doped FM-M state at $x = 0.4$. The bottom left corner in each panel is $\mathbf{q} = \{0, 0\}$, and the top right corner is $\mathbf{q} = \{\pi, \pi\}$. Notice the broadening of the CO peak at $\{\pi, \pi\}$, *i.e*, the reduction in CO correlation length, with increasing $\Delta$.

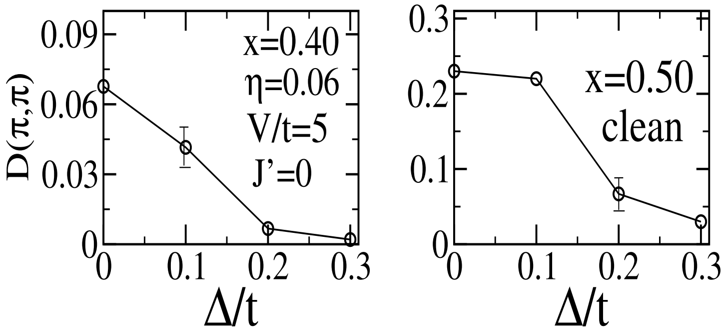

Figure 4.24: Reduction in the $\{\pi, \pi\}$ peak in $D(\mathbf{q})$ with A site disorder.

### 4.8.3 B valence fluctuation

We fixed our impurity valence to $+2$ or $+3$, etc. In principle there can be charge fluctuation and the electron count on the impurity may not be strictly integral. To check the magnitude of impurity valence fluctuation we did our calculation for different impurity level energy $V$. We used $V$=5 in earlier section to show FM-M to FM-M + AFM-CO-I mixed phase when $2+$ dopants doped at $x = 0.4$. In that case, the charge density at impurity side goes to zero to show that impurity valence kept fixed thorough out

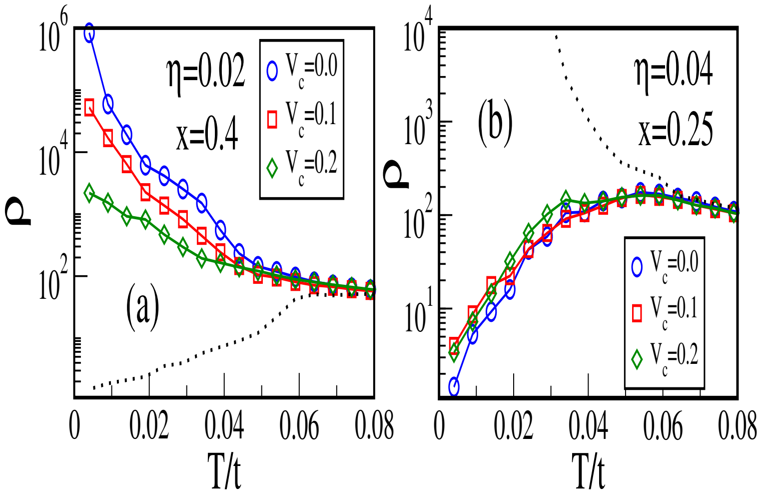

Figure 4.25: Resistivity peaks for non-magnetic 2+ non-magnetic dopants (like in the Fig-4.5) at $x = 0.4$ and $x = 0.25$ with various $V_c$ mentioned ($\eta = 0.06$ for $x = 0.4$ while $\eta = 0.04$ for $x = 0.25$).

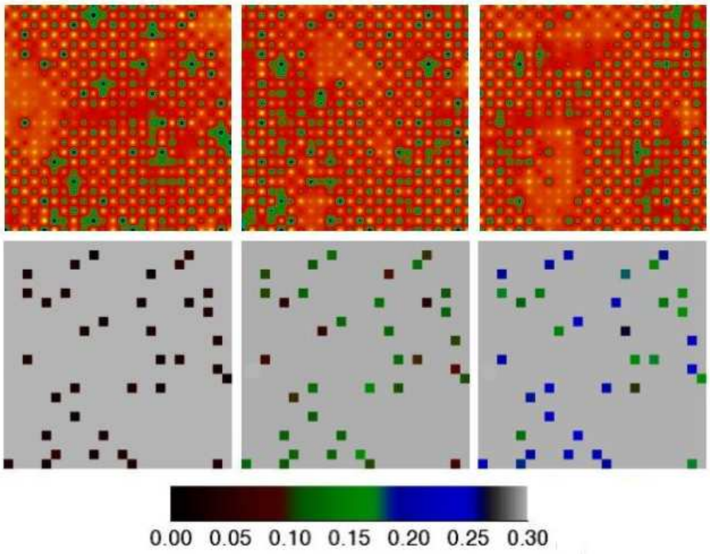

Figure 4.26: Density field $n_{\mathbf{r}}$ at low temperature for various $V$ values. from left: $V$=5, 2, 1 respectively and $J'$=0. Six percent of 2+ dopant with non-magnetic in nature doped in $x = 0.4$ using $\lambda = 1.6$ and $J$ =0.1.

the calculation. When $V$=2 or $V$=1 is used we still get the desired FM-M + AFM-CO-I mixed phase but the charge density in impurity site are no longer strictly zero. Fig-4.26 shows the mixed FM-M + AFM-CO-I phases in top panel while in bottom panel it shows the charge density at impurity site for $V$ = 5, 2, 1 (from left to right).

## 4.9 Conclusions

In this chapter we a more realistic model of B site doping compared to Chapter.3. We also explored a wider variety of reference states and impurity parameters, and compared our results with a wide variety of experiments. The phenomena discussed in this chapter emphasize the 'valence change' driven change in the manganite state, modified by the fragmenting effect of the B disorder. The next chapter will consider how magnetic interactions between the dopant and Mn complicate this reasonably simple scenario.

# Chapter 5

# Results: magnetic reconstruction

## 5.1 Introduction

We successfully explained some of the B site experiments in the manganites in the previous chapter. These include the B doping driven transition from a ferromagnetic metal to a charge ordered insulator, and the reverse transition from a CE charge ordered insulator to ferromagnetic metal. The B dopant driven change of the effective Mn valence was the driving force behind these effects. B dopants can modify the effective valence of Mn, and if this pushes the manganite towards a phase separation window, clusters of the 'neighbouring' phase can appear in the parent phase. With increasing B site doping the manganite can transform from its homogeneous parent phase to a fragmented version of the neighbouring phase.

We have explored this valence effect for several combinations of manganite states and B dopants. Significantly, *not all B doping results* can be explained by the valence change argument, in fact there are prominent cases where the state that emerges seem to be "opposite" to what is expected on grounds of valence change! This requires a non trivial extension of our approach.

It is observed that different B ions of same valence, doped into the same reference manganite, can lead to quite different phases at low temperature. So, apart from the valence of B dopant, other interactions must be at play in deciding the final state of the doped material. This is particularly true where magnetic dopants are concerned, and the interaction between the Mn moment and the B moment becomes a crucial parameter, the 'valence change' effect being relevant only where the B-Mn magnetic interaction is weak. We will work out a classification of these effects in this chapter.

## 5.2 Magnetic 3+ dopants on the CE-CO-I

Let us recapitulate the cases where the magnetic character of the B site dopant plays an important role. For example, the ferromagnetic metallic ground state in Cr doped $La_{0.5}Ca_{0.5}MnO_3$ (LCMO) [56] cannot be explained using valence change arguments. With Cr, a $3+$ dopant, the hole density of the manganite *increases* from the initial $x = 0.50$ but there is no FM-M phase with any hole density greater than $x = 0.50$ [5] in LCMO! $Nd_{0.5}Ca_{0.5}MnO_3$ (NCMO) at half filling is another CE-CO insulator with smaller bandwidth than LCMO. When doped with 3% Cr it shows coexistence of FM-M and CO-I phases at low temperature [56, 65]. There is no FM phase for $x > 0.50$ in NCMO either. Both these manganites have FM-M phases at $x < 0.50$. Dark field images at temperatures below the transition temperature shows that the hole density in the FM domains is less than $x = 0.5$, see Fig-2.9. This is surprising because the valence change on doping $3+$ ions is in a direction opposite to the clean ferromagnetic phase, so Cr doping should not have led to a FM-M.

Not only Cr, but Ni and Co also lead to ferromagnetism at low temperature when doped into NCMO, going against the valence change scenario. Note, however, that $3+$ impurities like Fe, Al, and Sc when doped into the same manganite at $x = 0.50$ do not lead to any sign of ferromagnetism at any temperature, see Fig-2.12, [66, 104].

If we apply our valence change argument discussed in the previous chapter, the effective hole density ($x_{eff}$) shifts to $x > 0.5$ when $3+$ dopants are introduced into the $x = 0.5$ manganite. If that is the case, then a mixture of CE correlations (from $x = 0.5$) and A-2D phase (at $x = 0.55$) is expected at low temperature. The very weak ferromagnetic feature when Fe, Al or Ga (all $3+$ dopants) are introduced into NCMO (see Fig-2.12) is correctly explained by our valence change argument. For us the mystery is why some trivalent/divalent dopants like Cr and Ni convert the CE-CO-I to a FM state, while other $3+$ dopants, including a magnetic one like Fe, is unable to do so.

## 5.3 V-J′ phase diagram for 3+ dopants

The CE-CO-I phase is stable at $x = 0.50$ only for a certain range of electron-phonon coupling, $\lambda$ and AF exchange $J$ in the parent manganite (see Fig-3.1). We work mainly

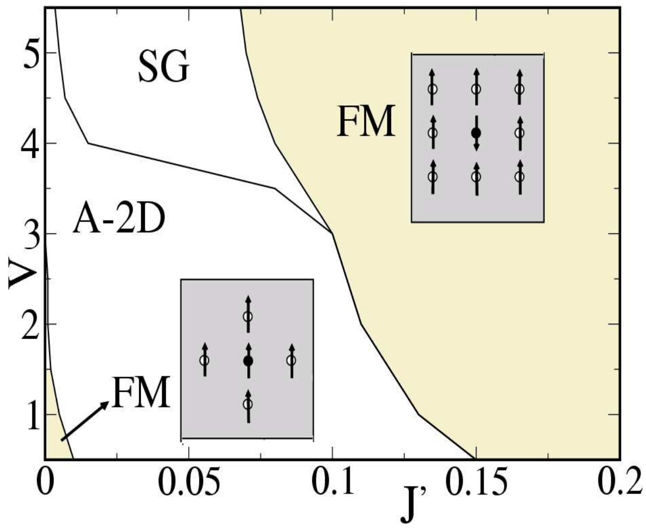

Figure 5.1: Low temperature 'phases' at $x = 0.50$ for varying $V$ and $J'$ in the presence of B site doping for 3+ dopants in presence external magnetic field 0.002. We have taken $\lambda = 1.6$ and $J = 0.1$. There are two windows of ferromagnetism in the phase diagram, the other regions are either spin disordered phase or mostly A-2D phase.

at fixed $\lambda = 1.60$ and $J = 0.1$, and vary $\lambda$ where necessary to mimic bandwidth variation. As we have seen earlier, there is a phase separation window (as shown in Fig-3.9) on both sides of the $x = 0.50$ CE-CO-I. For $x \geq 0.55$ we have the antiferromagnetic A-2D phase and for $x \leq 0.40$, we have the FM-M phase. Dopants with valence $\leq 3+$ change $x_{eff}$ to a larger hole density. A small doping $3+$ ions at $x = 0.50$ will shift the $x_{eff}$ into the PS region between $x = 0.50$ and $x = 0.55$ creating a mixture of A-2D and CE phase.

We indicated earlier that Fe, Ni, Cr magnetically interact with their neighbouring Mn. Experiments suggests that Cr has strong AF coupling to the Mn ions and Ni couples ferromagnetically [100]. Fe is magnetic but interacts weakly with the Mn ions due to its stable $d^5$ configuration and this may be the cause for the absence of ferromagnetism on Fe doping.

There are two parameters that control the Mn-B magnetic interaction in the manganites. One is the superexchange between the Mn and the B ion, the other is the $e_g$ level of the B ion. The strength of superexchange (SE) between a Mn ion and the neighbouring B ion can be different from the Mn-Mn SE interaction. We denote the Mn-B SE coupling as $J'$ and set the B electron level at $V$. $V$ will control possible double exchange based ferromagnetic coupling between the B ion and Mn. The two parameters $J'$ and

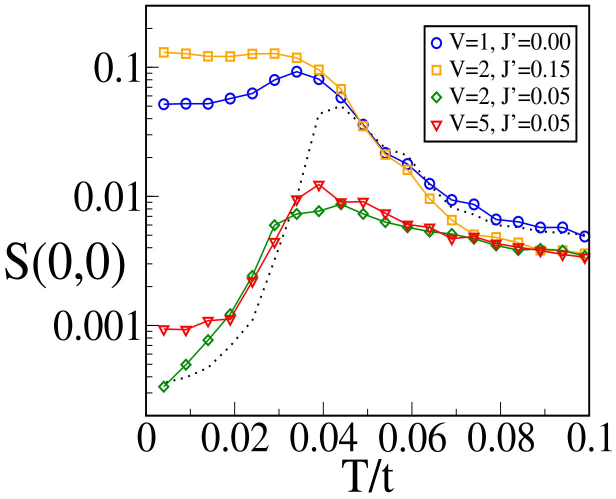

Figure 5.2: Temperature dependence of the ferromagnetic peak in $S(\mathbf{q})$, for parameter points in various parts of the phase diagram(Fig-5.1). The data is shown for four representative points.

$V$ define our minimal set. As usual we will measure these energies in terms of the manganite hopping $t$.

Fig-5.1 shows the phase diagram of the B doped CE-CO-I for different $V$ and $J'$. As before we use $\lambda = 1.6$ and $J = 0.1$, set $\eta = 0.08$, and have used a small field $h = 0.002$. There are two FM regions and one large non-ferromagnetic window in the phase diagram. The non-ferromagnetic region is divided into a phase with A-2D type correlations and a disordered 'spin glass' (SG) like phase. The SG phase is a disordered variant of the A-2D phase and CE phase, with short range stripelike correlations. We find two unexpected FM regions, one at small $J'$ and small $V$, the other at large $J'$ and large $V$.

Fig-5.2 shows the $\mathbf{q} = \{0, 0\}$ ferromagnetic feature in the structure factor plotted against temperature for four combinations of $J'$ and $V$ probing different regions of the phase diagram. We consider the four cases: (a) $J' = 0$, $V = 1$, (b) $J' = 0.15$, $V = 2$, (c) $J' = 0.05$, $V = 2$ and (d) $J' = 0.05$, $V = 5$. Only (a) and (b) shows significant ferromagnetism at low temperature while the other two have negligible ferromagnetic correlation. The dotted line shows the ferromagnetic feature for the reference CE-CO-I, vanishing as $T \rightarrow 0$.

### 5.3.1 Origin of FM correlations

One of the FM region is for large $J'$, and the $J'$ required to observe this phase reduces with increasing onsite energy $V$. At $V \sim 1$, the $J'$ for which we get ferromagnetism is large compared to reference Mn-Mn AF interaction $J = 0.1$. With increase in $V$ the ferromagnetic window shift towards lower $J'$ and to even $J' < J$ for $V > 5$. The change in $J'$ with $V$ is discussed later in this section.

#### Ferromagnetism at large $J'$

As discussed before, the CE phase consists of zigzag ferromagnetic chains coupled to each other. Fig-5.3 shows the schematic view of CE-CO phase. In CO sector nominally Mn$^{3+}$ and Mn$^{4+}$ alternate in the $x - y$ plane. The peculiar property of the CE phase is that each site has two ferromagnetic neighbours and two antiferromagnetic neighbours. In the zigzag magnetic chain of CE phase, the length of linear segments is 3 sites (see Fig-1.9). Mn$^{3+}$ ions always occupy the center of this segment, while Mn$^{4+}$ are on the corner sites. This why in the CE phase, Mn$^{3+}$ ions are sometime known as 'bridge sites' and Mn$^{4+}$ ions as 'corner sites'.

Because of large electron density in the Mn$^{3+}$ site it is orbital ordered due to Jahn-Teller distortion, while the orbital variable is 'inactive' in the Mn$^{4+}$ site due to its low electron density.

- The Mn$^{4+}$ ion has two nearest neighbour (NN) spins parallel and other two NN spins antiparallel to it, while all its next nearest neighbour (NNN) Mn$^{4+}$ spins are antiparallel.
- The Mn$^{3+}$ ion has two NN spins parallel and other two NN spins antiparallel to it. Unlike the Mn$^{4+}$, two of its NNN spins are antiparallel while other two are parallel to it.

In contrast to the reference CE phase with $J = 0.1$, large $J'$ forces all four nearest neighbours of a B spin to be anti-parallel to it. Let us consider one B dopant to start with. In the presence of a large potential at the B site, the electron density in the B site is very small. There is also a large $J'$ which force Mn spins around the B site antiparallel to it. There is negligible gain via DE ferromagnetism in this case.

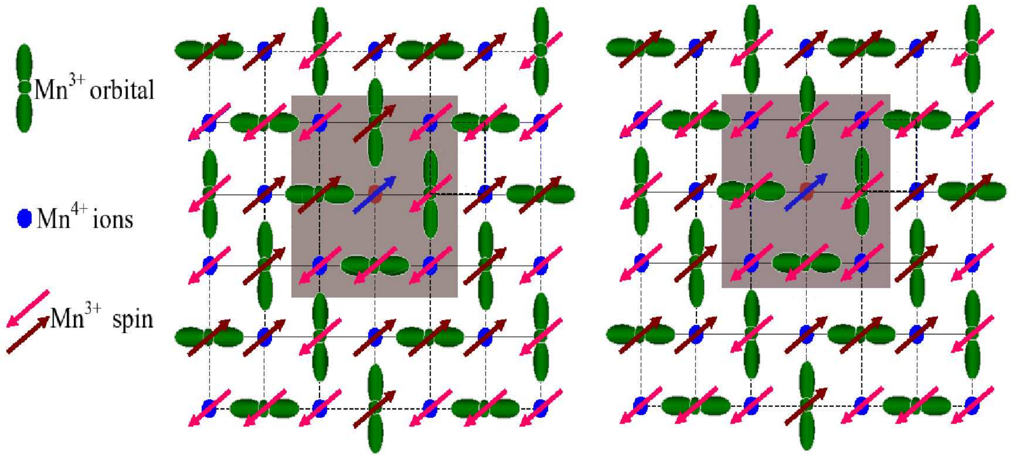

Figure 5.3: Schematic of CE-CO phase with an impurity. The horizontal and vertical lines on the lattice sites represent the positive and negative oxygen octahedra distortions. CE phase consists of FM zigzag chains which are coupled antiferromagnetically. Left panel: One of the bridge site (as the central site) and all its nearest neighbours (NN and NNN) are indicated in shaded region. Two of the NN spins are parallel to the central site and rest two are anti-parallel. All NNN are anti-parallel. Right panel : When B dopant sits on the central site of shaded region, due to large $J'$, all NN spins are forced to align apposite to it for which all 8 spin (4 are NN, 4 are NNN) aligns anti-parallel to the central spin.

The larger the onsite potential, the smaller is the $J'$ required to align the nearest neighbours antiparallel. This is because at large V, the electron density on the impurity site is zero. So even if nearest neighbours are parallel to it, there is no gain kinetic energy as electron can not hop to the impurity site with large V. So even for small antiferromagnetic superexchange, the neighbour spins align anti-parallel to the impurity spin. But for other extreme case when $V$=0.5, large antiferromagnetic superexchange is required to align the nearest neighbour spin anti-parallel to the impurity spin.

Let us discuss the two cases, one when the B dopant goes to Mn$^{4+}$ site, the other when it goes to the Mn$^{3+}$ site:

1. The Mn$^{4+}$ location is the corner site of the zigzag FM chain in the CE phase. Due to large $J'$, all the neighbouring Mn spins align antiparallel to the B moment, while all 4 NNN neighbours are already antiparallel to it. So there is a FM 'ring' of $8$ Mn spins around the B site forming a '$1+8$' structure as shown in the right panel of the Fig-5.4. With large $J'$ the $e_g$ charge density at the B site is small and around it all the four Mn sites are Mn$^{3+}$ as nearest neighbour. This reconstruction

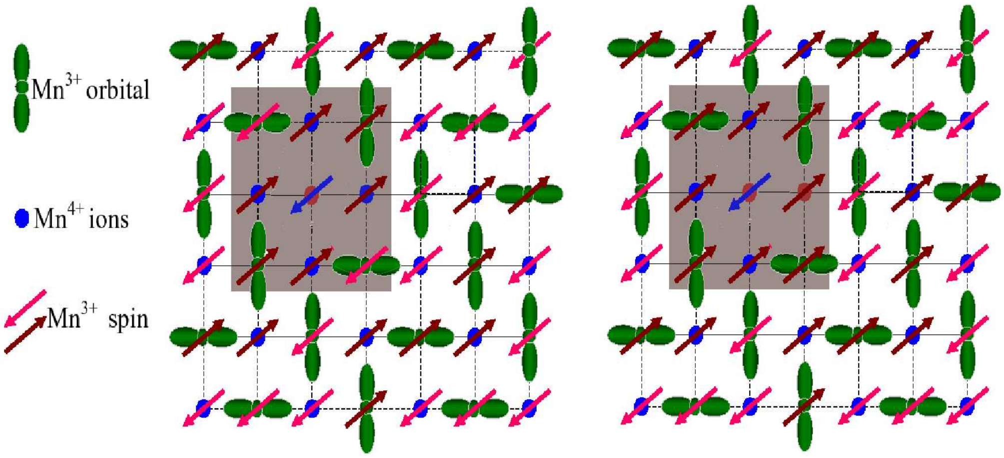

Figure 5.4: Schematic of CE-CO phase with an impurity. The horizontal and vertical lines on the lattice sites represent the positive and negative oxygen octahedra distortions. CE phase consists of FM zigzag chains which are coupled antiferromagnetically. Left panel : We put B site dopant on a corner site. All its nearest neighbours (NN and NNN) are indicated in shaded region. We already changed all the the NN anti-parallel to the B site dopant because of large $J'$. Here out of four NNN spins, two of them are parallel and two of them are anti-parallel to the central spin. Right panel : Those two NNN spins which are anti-parallel to the B site dopant, now sees three of its NN are anti-parallel as shown in left panel. To gain kinetic energy that spin direction changes. This is why all 8 spin (4 are NN, 4 are NNN) align antiparallel to the central spin as in Fig-5.3

has only a local effect on the CE-CO phase, leaving the original order intact far from the B site.

2. The Mn$^{3+}$ location is the bridge site of the zigzag FM chain in the CE phase. Due to large $J'$, all the neighbouring Mn spins align antiparallel to the B moment like the above case. But in this case only 2 NNN are already antiparallel while other two are parallel to it. These two parallel spins also change their direction to create all NNN spin antiparallel to the B site as explained in Fig-5.4

Recently, Martin et al. [72] discussed the Cr-doping effects in terms of the antiferromagnetic spin coupling between Cr$^{3+}$ and Mn$^{3+}$ ions which causes the ferromagnetism and metallicity when a sufficient level of Cr is doped into the system. In our calculation, B$^{3+}$ replaces a Mn$^{4+}$ to help maintain charge order of the $e_g$ electrons.

However, there is also electrostatic interaction between the ions to consider. On that count B$^{3+}$ dopant *should replace the Mn$^{3+}$ ion* to minimize the NN Coloumb repulsion.

We have done our calculation taking the nearest neighbour Coulomb repulsion into account. $B^{3+}$ replaces a $Mn^{3+}$ and the short range Coulomb repulsion self consistently creates $Mn^{4+}$ nearest neighbours around it. This keeps the charge and CE order intact far from the CE dopant. Hereafter all our results are in the presence NN Coulomb repulsion, and this leads to $B^{3+}$ replacing $Mn^{3+}$ to create the '1+8' magnetic moment discussed before, Fig- 5.4.

Now the case of multiple B dopants. These dopants will be randomly located, and they cannot be viewed simply as replacing $Mn^{3+}$ in the original CE-CO checkerboard. Let us consider two B dopants in different sublattice of the checkerboard and far from each other. Locally the B site dopant behaves as if it replaces $Mn^{3+}$ and constructs '$1+8$' magnetic structure. When two dopants are close to each other each '$1 + 8$' magnetic moments gets connected and form a large magnetic cluster around them. This effect reconstructs the charge/magnetic order in the system when large amount of dopants are present in the system.

With a low percentage of dopants, the B site always creates a ring of '$1 + 8$' and the moment of this 'large spin' is aligned randomly if the B dopants are not close to each other. At large enough impurity concentration the FM rings align in the same direction to promote long range FM correlation. Notice this argument did not involve the valence of the dopant.

Along with the AF coupling $J'$, the other crucial effect comes from the (short range) Coulomb repulsion $V_c$ (See Section 4.4 for details). We assume $V_c = 0.1$ in our calculation [101, 102]. Due to this $3+$ B dopants prefer $Mn^{4+}$ ions as nearest neighbours. The effective hole density increases with $3+$ dopant but most of the low electron density (high hole density) sites are close to the B dopants. Some sites with high electron (low hole density) club together in some impurity free patches. These low hole density patches are ferromagnetic in nature, with effective hole density $< 0.50$, as in the parent manganite phase diagram.

Formation of '$1 + 8$' magnetic moment with B site dopant and creating low electron density around B site both go side by side. The overall pattern that emerges is a complex mix of FM-M and AF regions. The overall ferromagnetism emerges from a combination of $(i)$ breakup of the CE pattern by the magnetic dopants, creating tiny FM clusters, and $(ii)$ their coupling via FM-M droplets created by charge pushed out

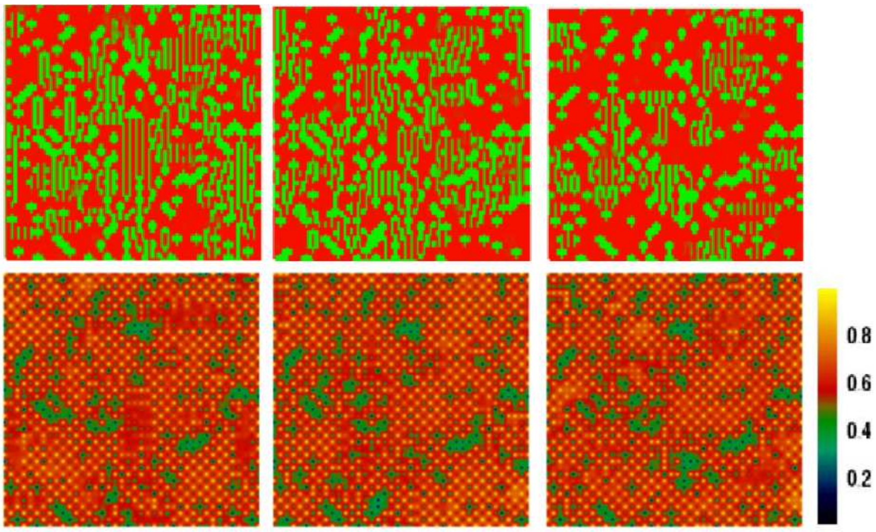

Figure 5.5: Conversion to FM. Top: Nearest neighbour spin correlation $\mathbf{S}_i.\mathbf{S}_j$ from MC snapshots at $\eta = 0.08$, $J' = 0.15$ and $V = 2$ at low temperature. Bottom: corresponding density field $n_r$ at low temperature. Left to right, increasing magnetic field h0 = 0, h1 = 0.002, h2 = 0.005.

due to the Coulomb interaction.

Fig-5.5 shows the nearest neighbour $\mathbf{S}_i.\mathbf{S}_j$ from MC snapshots in magnetic fields $h0,\ h1,\ h2$, from left to right, for $\eta = 0.08$. Throughout the chapter $h0 = 0$, $h1 = 0.002$ and $h2 = 0.005$. The MC snapshot shows ferromagnetic patches and we found that these ferromagnetic patches are of electron density more than 0.5. This explains the coexistence of charge ordered insulating phase with ferromagnetic metallic phase for Cr doping in NCMO [56].

### Ferromagnetism for small $J'$

With small $J'$ and small $V$ there is another ferromagnetic window. Here with smaller $J'$, B site impurity connects to nearest neighbours Mn sites ferromagnetically. The FM alignment is due to the gain in kinetic energy due to double exchange that is now allowed. In the present case clusters of $5$ spins form a magnetic moment, as shown in the inset of Fig-5.1. This '5 site' object is the building block for ferromagnetism in this regime. As the $e_g$ orbital energy ($V$) grows, this phase gets quickly suppressed due to the reduction in double exchange. The electron density for $V$ = 1 (and electron phonon coupling is neglected in impurity site) in our calculation is $\sim$ 0.2 and the impurity valence is $\sim 2.8$ rather than the assumed 3.

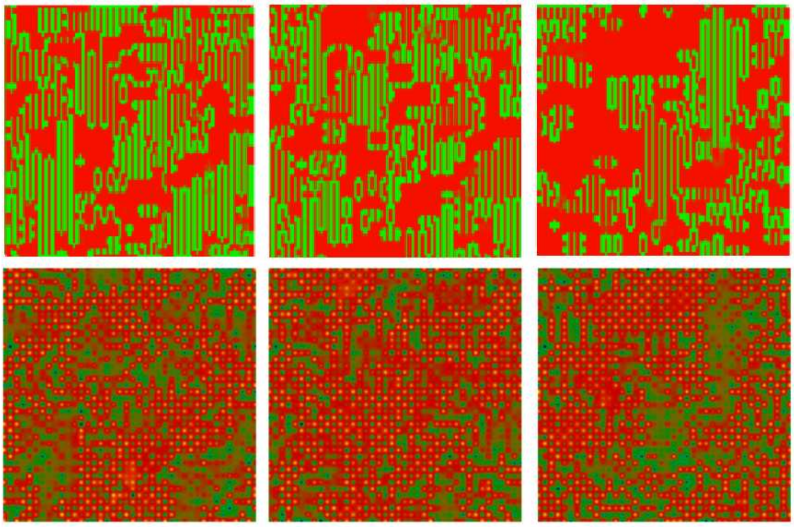

Figure 5.6: Conversion to FM. Top: Nearest neighbour $\mathbf{S}_i.\mathbf{S}_j$ from MC snapshots. Bottom: corresponding density field $n_r$. $\eta = 0.08$, $J' = 0$, and $V = 1$ (Ni like dopant). Left to right, increasing magnetic field, h0 = 0, h1 = 0.002, h2 = 0.005.

Fig-5.6 shows the nearest neighbour $\mathbf{S}_i.\mathbf{S}_j$ from MC snapshots at $\eta = 0.08$ for B site dopants on the CE-CO phase with fields $h0, h1, h2$ from left to right. We use $V = 1$ and $J' = 0$ in this calculation. These snapshots clearly show the FM patches with a small applied magnetic field. The ferromagnetic patches are weakly charge ordered. This ferromagnetism is purely due magnetic reconstruction. There are AF A-2D regions also present alongwith the FM regions.

### 5.3.2 Spin disordered region

In the phase diagram there is no ferromagnetic phase at large $V$ and small $J'$. In this case the system cannot generate either a cluster of five spins, or the '1+8' configuration. Other dominant phase at small $V$ and intermediate $J'$ is the A-2D. The spin disordered region is a complex mixture of A-2D phase and the CE phase. To draw parallel with the experiments, Fe doping on the CE phase leads to this kind of a situation due to the weak magnetic interaction between Fe and Mn.

For non-magnetic $3+$ dopants like Al or Ga the valence change dominates (we are at large $V$ and $J' = 0$) and there is no ferromagnetism, as observed experimentally [66, 104]. Fig-5.7 shows the nearest neighbour $\mathbf{S}_i.\mathbf{S}_j$ from MC snapshots at $\eta = 0.08$ for this category B site dopants at reference state x=0.50, at fields $h0, h1, h2$. We have taken $V =$

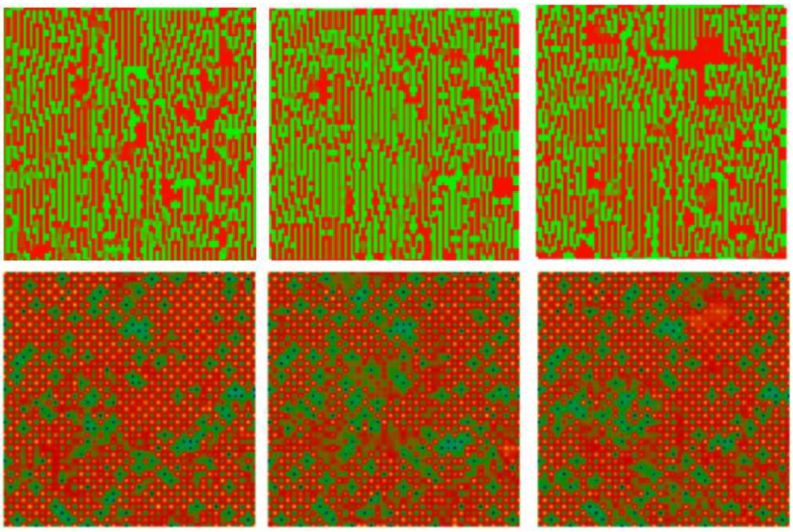

Figure 5.7: No conversion to FM. Top: Nearest neighbour $\mathbf{S}_i.\mathbf{S}_j$ from MC snapshots. Bottom: corresponding density field $n_r$. $\eta = 0.08$, $J' = 0.05$, $V = 5$ (Fe like dopant). Left to right: increasing magnetic field, h0 = 0, h1 = 0.002, h2 = 0.005.

$5$ and $J' = 0.05$ for this calculations. There is no significant ferromagnetic correlation even in an external field. The corresponding density field is also disordered as shown in the bottom panel.

## 5.4 Ferromagnetism and metallicity at large $V$ and $J'$

In previous section we explained the three main regions in the phase diagram. We believe that at large $J'$ regime we get the ferromagnetism due to the complex structure of CE phase. Along with large $J'$, nearest neighbour Coloumb interaction plays a role in this regime in creating ferromagnetic correlations. This highlights the need to go beyond the valence change scenario of the previous chapter.

Fig-5.8 shows the $T$ dependence of ferromagnetic order and resistivity for various $\eta$. We use $J' = 0.2$ and $V = 5$ but our discussion is valid in the large $J'$ region overall in the phase diagram (Fig-5.1). There is no significant ferromagnetic feature for any $\eta$ in absence of external magnetic field as shown in Fig-5.8(a). Corresponding resistivity is shown in the figure (b). For all $\eta$ we find large resistivity at low temperature. If we compare the same calculation for a $4+$ dopant like in Fig-4.18 we get ferromagnetism and metallicity for $\eta = 0.08$.

We get bulk FM order for $3+$ dopants at large $J'$ for small external magnetic field, as

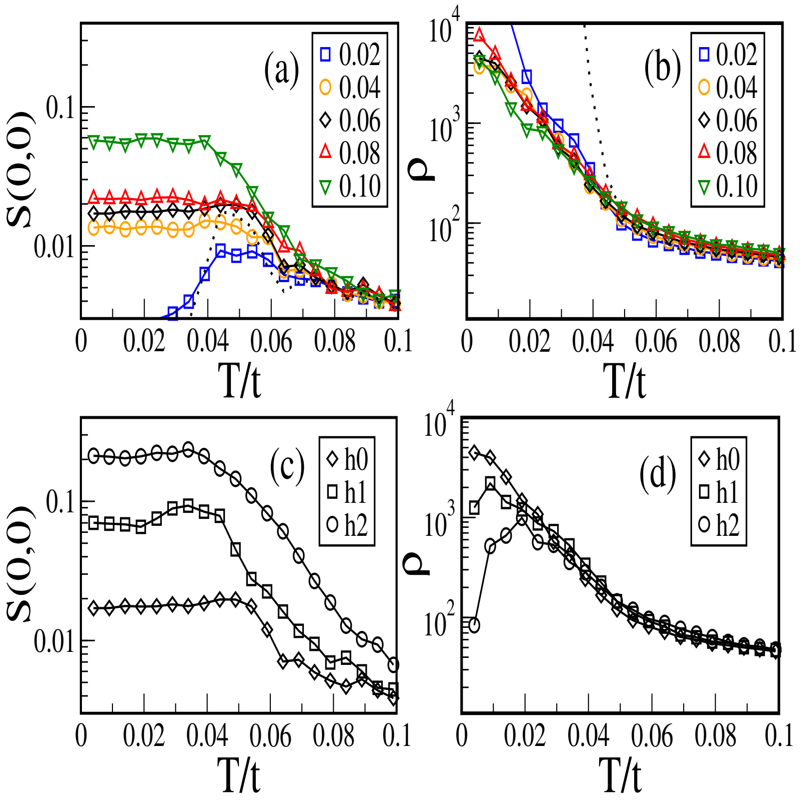

Figure 5.8: Transport and magnetic properties at low temperature with $3+$ dopant with large $J'$. (a). Temperature dependence of the ferromagnetic peak for different $\eta$. (b). Corresponding resistivity in absence of any external field. (c). and (d). show the finite field response. Impurity parameters: $\eta = 0.06$, $J' = 0.2$, $V = 5$.

shown in Fig-5.8(a). Fig-5.9 shows the DOS for various $\eta$ at low temperature. Although there is DOS at Fermi level unlike CE phase in finite B site doping, DOS is not increasing much with $\eta$. With $\eta = 0.08$, the DOS saturates and the DOS decreases after that. This explains the high resistivity at low temperature due to low DOS at Fermi level. Decrease in DOS after $\eta = 0.08$ suggests that the large quenched disorder playing is a role, and it is not easy to tune this state with a small magnetic field. The system is a bad metal at low temperature.

Fig-5.8(c) and (d) shows the effect of external magnetic field on ferromagnetism and resistivity with $\eta = 0.06$. With application of small magnetic field, the ferromagnetic peak enhanced as shown in Fig-5.8(c). Fig-5.8(d) shows the resistivity change with application of external magnetic field. There is turn in resistivity curve at low temperature and it shows that it is at least metallic (a bad metal) at low temperature.

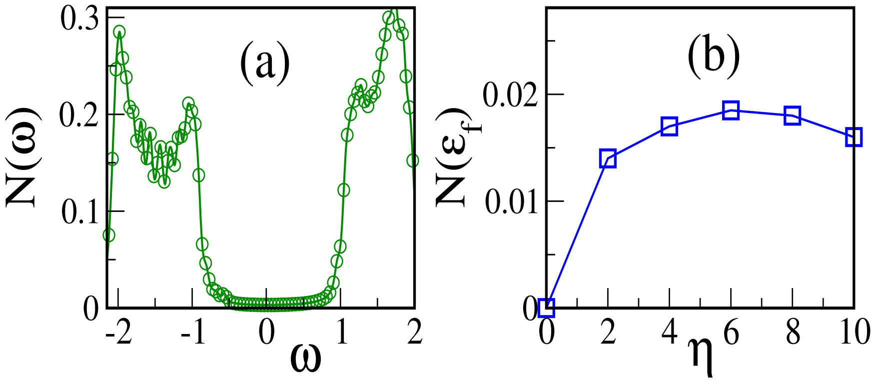

Figure 5.9: (a) DOS for $x$=0.50 at low temperature. (b) DOS at Fermi level for 3+ dopant with various $eta$ value.

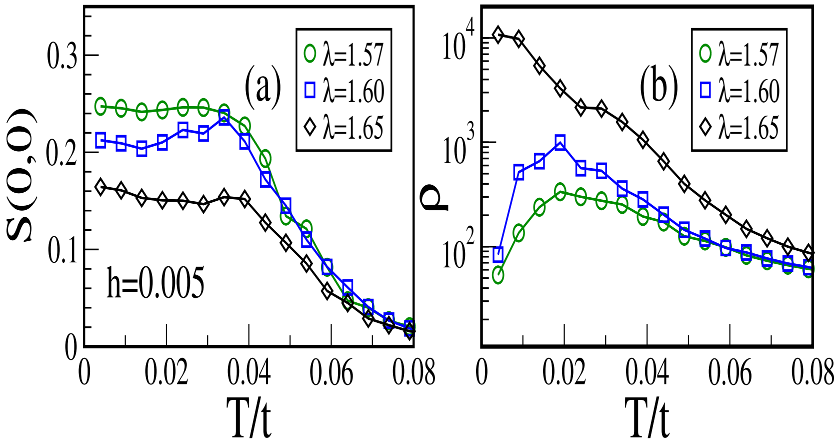

Figure 5.10: (a) Temperature dependence of the magnetization with $J'$ = 0.2 and $V$ = 5 for various $V_c$ at h = 0.005 for $\eta = 0.06$. (b)Temperature dependence of the corresponding resistivity.

For completeness we have calculated the resistivity and ferromagnetic peaks for few $\lambda$ values to mimic the bandwidth dependence. We have calculated both the ferromagnetic peaks and resistivity in presence of finite magnetic field for $6\%$ of dopants. Fig-5.10 shows the ferromagnetic peaks and resistivity with temperature for three $\lambda$ value. The low temperature ferromagnetic peak is smaller for $\lambda = 1.65$ and increases when we go to $\lambda = 1.57$. Resistivity in (b) shows insulating behaviour for $\lambda = 1.65$ and metallic behaviour for other the two $\lambda$. This low temperature resistivity and ferromagnetic peak indicate that the low bandwidth material (large $\lambda$) is not easy to metallise using B site dopants because the CO state is more stable at low bandwidth. For instance, the ferromagnetic peak at low temperature (see Fig-2.13) decreases from $La_{0.5}Ca_{0.5}MnO_3$

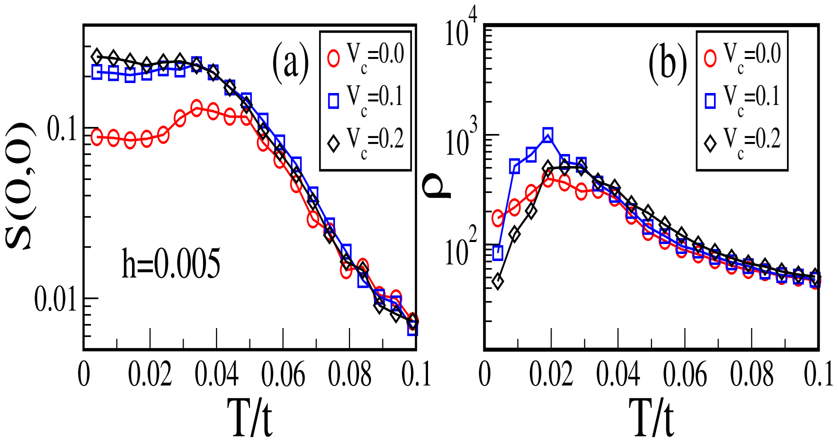

Figure 5.11: (a) Temperature dependence of the magnetization with $J'$=0.2 and $V$ = 5 for various $V_c$ at h=0.005 for $6\%$ dopants. (b)Temperature dependence of the corresponding resistivity.

to Nd$_{0.5}$Ca0.5MnO$_3$ when same amount ($\eta = 0.05$) of Cr is doped into the manganites.

## 5.5 Role of Coulomb repulsion

Nearest neighbour Coloumb repulsion plays an important role while doping the CE-CO state. Fig-5.11(a) shows the effect on the ferromagnetic peak for different $V_c$ at large $J'$ in the presence of a small magnetic field, 0.005. With $V_c$ = 0, for $V$ = 5, $J'$ = 0.2 as shown in (a), ferromagnetic peak is less than 0.1 but there is finite peak. When $V_c$ is 0.1 or 0.2, the ferromagnetic peak is enhanced. Fig-5.11(b) shows the respective resistivity peak for different $V_c$. With increase in the $V_c$, the metallicity at low temperature increases.

The increase in ferromagnetic correlations with the variation of $V_c$ has more impact in the large $J'$ region of the phase diagram. Fig-5.12 shows nearest neighbour $\mathbf{S}_i.\mathbf{S}_j$ from MC snapshots at $(\eta = 0.06)$ for $J'$ = 0.2 and $V$ = 5 for h = 0.005 for various $V_c$. For $V_c$ = 0.1 there are large ferromagnetic patches along with AF-CO. And for $V_c$ = 0.2 ferromagnetic patches are even larger. We show the corresponding density field $n_{\mathbf{r}}$ with same values of $V_c$. There is one to one correspondence between the FM clusters and CD regions of electron density more than 0.5.

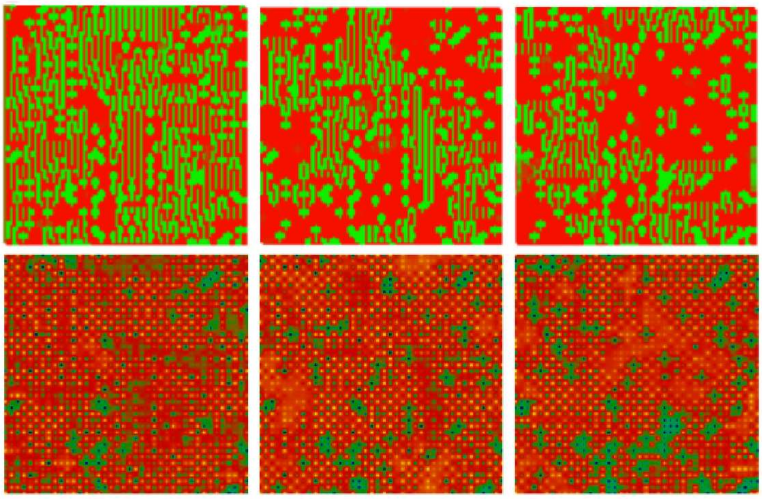

Figure 5.12: Top: Nearest neighbour $\mathbf{S}_i.\mathbf{S}_j$ from MC snapshots at $\eta = 0.06$ for $J' = 0.2$ and $V = 5$ for h=0.005. Columnwise: From left to right with nearest neighbour Coloumb repulsion $V_c$ = 0.0, 0.1, and 0.2. Bottom: corresponding density field $n_r$ at low temperature.

## 5.6 Conclusions

In this chapter we extended our calculation to explain the non trivial effect of few dopants like Cr/Ni on a CE-CO-I. Although valence change is in opposite direction with respect to the FM-M phase, the magnetic reconstruction creates large magnetic patches and leads to ferromagnetism. We highlight the case where dopant (Cr like) has a large AF coupling to the neighbouring Mn compared to the Mn-Mn coupling. The resulting FM-M+AF-CO phase is quite complicated for $3+$ dopants unlike the $4+$ dopant case discussed in the previous chapter. We crudely guessed the SE interaction between B dopant and neighbouring Mn, but we believe one can extract this value from first principle calculations.

# Chapter 6

# Magnetism in the Kondo lattice model

The Kondo lattice model describes local moments on a lattice coupled to an electron band. Such local moments arise from electron correlation and Hunds coupling in the $d$ shells of transition metals or the $f$ shells of rare earths. Although historically the 'Kondo lattice' arose as the lattice version [105] of the Kondo impurity problem, and refers to $S = 1/2$ moments coupled to conduction electrons, there are also systems with local electron-spin coupling where the moment is due to a spin with $2S \gg 1$. In that case the quantum fluctuations of the local moment, and the Kondo effect itself, are not relevant. Such a system can be described by a classical Kondo lattice model (CKLM). This limit is relevant for a wide variety of materials, *e.g*, the manganites [5, 7], where $S = 3/2$ moments couple to itinerant electrons via Hunds coupling, or $4f$ metals [106, 107, 108, 109, 110], *e.g*, Gd with $S = 7/2$, or the Mn based dilute magnetic semiconductors [111] where $S = 5/2$. In some of these materials, notably the manganites, the coupling scale is known to be large, while in the $f$ metals they have been traditionally treated as being weak. Other materials like in the magnetic semiconductors, coupling scale varies from intermediate range to large scale like that in manganite.

The Kondo lattice model is given by

$$H = -\sum_{\langle ij\rangle\sigma} t_{ij} c^{\dagger}_{i\sigma} c_{j\sigma} - \mu \sum_i n_i - J_H \sum_i \vec{\sigma}_i.\mathbf{S}_i \tag{6.1}$$

We will use $t = 1$ as the nearest neighbour hopping amplitude, and explore a range of $t'$, the next neighbour hopping, on a cubic lattice. Changing $t'$ will allow us to explore changes in the (bare) Fermi surface, and particle-hole asymmetry. $\mu$ is the chemical potential, and $J_H > 0$ is the local electron-spin coupling. We assume the $\mathbf{S}_i$ to be classical unit vectors, and absorb the magnitude of the core spin into $J_H$ wherever necessary. $\vec{\sigma}_i$ is the electron spin operator. We work with $\mu$, rather than electron density $(n)$, as the control variable so that regimes of phase separation (PS) can be detected, and study the magnetic properties for varying $n$, $t'/t$, $J_H/t$, and temperature $T/t$.

The CKLM involves the ordering of 'classical' spins, but the effective interaction between spins is mediated by electron delocalisation and cannot be described by a short range model. In fact the major theoretical difficulty in analysing these systems is the absence of any simple classical spin model. Nevertheless, there are two limits where the CKLM is well understood. (a). When the electron-spin coupling is small, one can perturbatively 'integrate out' the electrons and obtain the celebrated Ruderman-Kittel-Kasuya-Yosida (RKKY) model [112]. The effective spin-spin interaction in this limit is oscillatory and long range, controlled by the free electron susceptibility, $\chi_0(\mathbf{q})$, and the magnetic ground state is generally a spiral. (b). When the electron-spin coupling is very large compared to the kinetic energy, the 'double exchange' (DE) limit, the electron spin is 'slaved' to the orientation of the core spin and the electronic energy is minimised by a ferromagnetic (FM) background [13, 23, 24]. This leads intuitively to a spin polarised ground state.

In many materials the ratio of coupling to hopping scale is $\geq 1$, but not quite in the double exchange limit. In that case one has to solve the coupled spin-fermion model from first principles. Doing so, particularly in three dimensions and at finite temperature, has been a challenge. We study this problem using a combination of variational calculation and full spin-fermion Monte Carlo.

Our principal results are the following: (i) We are able to map out the magnetic ground state all the way from the RKKY limit to double exchange, revealing the intricate evolution with coupling strength. (ii) We demonstrate that the phase boundaries depend sensitively on electronic hopping parameters. This is not surprising in the RKKY regime, but the dependence at stronger coupling is unknown. (iii) We use our results to revisit the classic $4f$ magnets, widely modelled as RKKY systems, and suggest that with increasing $4f$ moment, the effective coupling in these systems pushes them beyond the RKKY regime. We work out the signatures of this 'physics beyond RKKY'.

## 6.1 Earlier work

Although there have been many studies in the 'double exchange' ($J_H/t \rightarrow \infty$) limit [113, 114], the attempts to explore the full $n - J_H - T$ phase diagram have been limited. $(a)$ An effective action obtained from the CKLM via gradient expansion [115] has been analysed. This mapped out some of the commensurate and spiral phases in two dimensions, where the phases are fewer. It did not explore the finite temperature physics, *e.g*, the $T_c$ scales, and seems to be inaccurate when handling commensurability effects near $n = 1$. $(b)$ The model has been studied within dynamical mean field theory [116] (DMFT), and the broad regimes of ferromagnetism, antiferromagnetism (AFM), and incommensurate order have been mapped out. Unfortunately the effective 'single site' character of DMFT does not allow a characterisation of the incommensurate phases and misses out on the richness of the phase diagram. The loss of information about spatial fluctuations also means that critical properties, either in magnetism or transport, cannot be correctly captured. $(c)$ An 'equation of motion' approach [117] has been employed to study general *finite S* spins coupled to fermions, and results have been obtained in the classical limit as well. However, except the ferro and antiferromagnetic phases other magnetic states do not seem to have been explored. $(d)$ The full spin-fermion Monte Carlo, using exact diagnolisation, has been employed [87] in one and two dimensions but severe size limitations prevent access to non trivial ordered states.

## 6.2 Methods

The problem is technically difficult because it involves coupled quantum and classical degrees of freedom, and there is in general no equivalent classical spin Hamiltonian. The probability distribution for spin configurations is given by $P\{\mathbf{S}\} \propto Tr_{c,c^\dagger} e^{-\beta H}$, so the 'effective Hamiltonian' is $H_{eff}\{\mathbf{S}\} = -\frac{1}{\beta} log \ Tr_{c,c^\dagger} e^{-\beta H}$, the fermion free energy in an arbitrary background $\{\mathbf{S}_i\}$. It cannot be analytically calculated except when $J_H/t \ll 1$.

### 6.2.1 Analytic limits

When $J_H/t \ll 1$, the (free) energy calculated perturbatively to $\mathcal{O}(J_H^2)$ leads to the RKKY spin Hamiltonian [112], $H^{eff}_{RKKY} = \sum_{ij} J_{ij}\mathbf{S}_i.\mathbf{S}_j$, where $J_{ij} \sim J_H^2 \chi^0_{ij}$ and $\chi^0_{ij}$ is the non local susceptibility of the free $(J_H = 0)$ electron system. $\chi^0_{ij}$ is long range and oscillatory. We will analyse this model to understand the weak coupling phases. At strong coupling, $J_H/t \to \infty$, there is no exact analytic $H_{eff}$ but we can construct approximate self consistent models [118] of the form $H^{eff}_{DE} = -\sum_{\langle ij \rangle} D_{ij}\sqrt{1 + \mathbf{S}_i.\mathbf{S}_j}$, with the $D_{ij}$ related to the electronic kinetic energy. Unfortunately, when $J_H \sim \mathcal{O}(t)$ neither the RKKY model nor the DE approximation are valid. This regime requires new tools and we will use a combination of (i) variational calculation (VC) [119, 120] for the magnetic ground state, and (ii) spin-fermion Monte Carlo using a 'travelling cluster' approximation [97] (TCA-MC) at finite temperature in 3 dimension.

### 6.2.2 Variational approach

For the variational calculation we choose a simple parametrisation [1] for the spin configuration: $S_{iz} = \alpha$, $S_{ix} = \sqrt{1-\alpha^2}\, cos\mathbf{q}.\mathbf{r}_i$ and $S_{iy} = \sqrt{1-\alpha^2}\, sin\mathbf{q}.\mathbf{r}_i$. This encompasses the standard ferromagnet and antiferromagnet, as well as planar spiral phases, canted ferromagnets, and A and C type antiferromagnets. For a fixed $\mu$ and $J_H$ we compute the electronic energy $\mathcal{E}(\alpha, \mathbf{q}, \mu)$ and minimise it with respect to $\alpha$ and $\mathbf{q}$. The electronic density at the chosen $\mu$ is computed on the minimised state. Since the magnetic background only mixes electronic states $|\mathbf{k}, \uparrow\rangle$ and $|\mathbf{k} - \mathbf{q}, \downarrow\rangle$ the electronic eigenvalues $\epsilon^{\pm}(\mathbf{k}, \mathbf{q})$ are simple, and only an elementary numerical sum is required to calculate $\mathcal{E}(\alpha, \mathbf{q}, \mu) = \sum_{\mathbf{k},\pm} \epsilon^{\pm}(\mathbf{k}, \mathbf{q})\Theta(\mu - \epsilon^{\pm}(\mathbf{k}, \mathbf{q}))$.

### 6.2.3 Monte Carlo method

While the VC provides a feeling for the possible ground states, it has the limitation that (i) it samples only one family of (periodic) functions in arriving at the ground state, and (ii) finite temperature properties, *e.g*, the magnetisation and the critical temperature are not accessible. For this we 'anneal' the system towards the equilibrium distribution $P\{\mathbf{S}\} \propto Tr_{c,c^\dagger} e^{-\beta H}$ using the TCA based Monte Carlo. In this method the acceptance

---

[1] Our choice corresponds to a periodically varying azimuthal angle, $\phi_i$. The most general periodic state involves periodic variation in the polar angle $\theta_i$ as well [119, 120].

of a spin update is determined by diagonalising a cluster Hamiltonian constructed around the update site, and avoids iterative diagonalisation [87] of the full system. We can access system size $\sim 10^3$ using a moving cluster of size $4^3$.

The TCA captures phases with commensurate wavevector $\mathbf{Q}$ quite accurately, but access to the weak coupling incommensurate phases is poor. To get an impression of the ordering temperature for these phases we compute the energy difference $\Delta\mathcal{E}(n, J_H) = \frac{1}{N}(\mathcal{E}_{disord} - \mathcal{E}_{ord})$, between the ordered state and a fully spin disordered state in a large system. $\mathcal{E}_{ord}$ is calculated from the variational ground state, and $\mathcal{E}_{disord}$ by diagonalising the electron system in a fully spin disordered background on a large lattice. $\Delta\mathcal{E}(n, J_H)$ is the 'condensation energy' of the ordered state, and provides a crude measure of the effective exchange and $T_c$ and we could compare the trend to MC data, the agreement was reasonable.

## 6.3 Ground state: particle-hole symmetry

The results of the variational calculation in the 'symmetric' ($t' = 0$) case are shown in Fig-6.1. We employed a grid with upto $40^3$ $\mathbf{k}$ points, and have checked stability with respect to grid size. Let us analyse the weak and strong coupling regimes first before getting to the more complex intermediate coupling regime.

**(i)** *RKKY limit:* The key features for $J_H/t \to 0$ are: (i) the occurrence of 'commensurate' planar spiral phases, with wavenumber $\mathbf{Q}$ which is $\{0, 0, 0\}$, or $\{0, 0, \pi\}$, *etc*, over *finite* density windows, (ii) the presence of planar spirals with incommensurate $\mathbf{Q}$ over certain density intervals, (iii) the absence of any phase separation, *i.e*, only second order phase boundaries, and (iv) the presence of a 'G type', $\mathbf{Q} = \{\pi, \pi, \pi\}$, antiferromagnet at $n = 1$. Although the magnetic state is obtained from the variational calculation, much insight can be gained by analysing the $H^{eff}_{RKKY}$. Since the spin-spin interaction is long range it is useful to study the Fourier transformed version $H^{eff}_{RKKY} \equiv \sum_{\mathbf{q}} \tilde{J}_{\mathbf{q}} |\mathbf{S}_{\mathbf{q}}|^2$, where $\tilde{J}_{\mathbf{q}} = \sum_{ij} J_{ij} e^{i\mathbf{q}\cdot\mathbf{R}_{ij}}$ and $\mathbf{S}_{\mathbf{q}} = \sum_i \mathbf{S}_i e^{i\mathbf{q}\cdot\mathbf{R}_i}$. The coupling $\tilde{J}_{\mathbf{q}} = J_H^2 \chi_0(\mathbf{q}, n)$ is controlled by the spin susceptibility, $\chi_0(\mathbf{q}, n)$, of the $J_H = 0$ tight binding electron system. For our choice of variational state the minimum of $H^{eff}$ corresponds to the wavevector at which $\chi_0(\mathbf{q}, n)$ has a maximum. We independently computed $\chi_0(\mathbf{q}, n)$ and confirmed that the wavevector $\mathbf{Q}(n)$ obtained from the VC closely matches the wavevector

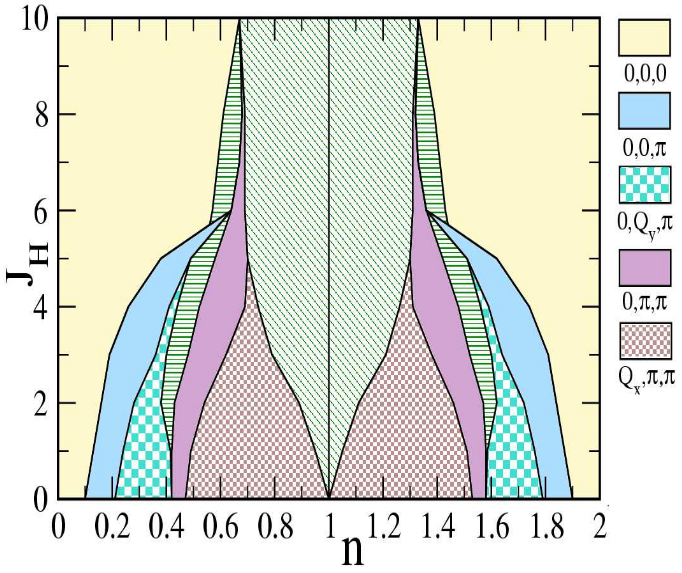

Figure 6.1: Magnetic ground state for the particle-hole symmetric model $(t' = 0)$ for varying electron density $(n)$ and electron-spin coupling $(J_H)$. The phases are characterised by their ordering wavevector **Q**, indicated by the colour code in the legend to the right, and their net magnetisation $\alpha$ (if any). Among the 'commensurate' phases, $\mathbf{Q} = \{0, 0, 0\}$ is the usual ferromagnet, $\{0, \pi, \pi\}$ and $\{\pi, \pi, \pi\}$ are antiferromagnets with no net magnetisation, while the $\{0, 0, \pi\}$ antiferromagnet has $\alpha = 0$ for $J_H \rightarrow 0$ but picks up finite magnetisation with increasing $J_H$. At $n = 1$ the system is always a $\mathbf{Q} = \{\pi, \pi, \pi\}$ antiferromagnet. The incommensurate phases have ordering wavevectors $\{Q_x, Q_y, Q_z\}$ of which at least one component is neither $0$ nor $\pi$. For such phases the exact wavevector depends on the value of $n$ and $J_H$. For example, for $J_H \rightarrow 0$ the (blue) checkerboard region in the left hand corner, to the right of $\mathbf{Q} = \{0, 0, \pi\}$, has wavevector $\mathbf{Q} = \{0, Q_y, \pi\}$, where $Q_y$ varies from $0$ to $\pi$ as one moves left to right. The (green) shaded regions in the phase diagram, *not indicated* in the legend, are windows of phase separation. No homogeneous phases are allowed in these regions. The results in this figure are based on a variational calculation using a $20^3$ **k** point grid, and cross-checked with data on $40^3$.

$\mathbf{q}_{max}(n)$ of the peak in $\chi_0(\mathbf{q}, n)$ apart from numerical inaccuracy between $\mathbf{q} = \{0, 0, 0\}$ and $\{0, 0, q\}$ [121]. The absolute maximum in $\chi_0(\mathbf{q}, n)$ remains at $\mathbf{q} = \{0, 0, 0\}$, as the electron density is increased from $n = 0$, and at a critical density $\mathbf{q}_{max}$ shifts to $\{0, 0, \pi\}$. With further increase in density $\mathbf{q}_{max}$ evolves through $\{0, q, \pi\}$ to the C type $\{0, \pi, \pi\}$, then $\{q, \pi, \pi\}$, and finally the G type AFM with $\{\pi, \pi, \pi\}$, where the Fermi surface is nested. The absence of 'conical' phases, with finite $(\alpha)$ and a spiral wavevector, is consistent with what is known in the RKKY problem. The variation of $\chi_0(\mathbf{q}, n)$ is plotted in Fig-6.2 for two dimensional KLM as we can do large size calculation up to $200^2$ **k**

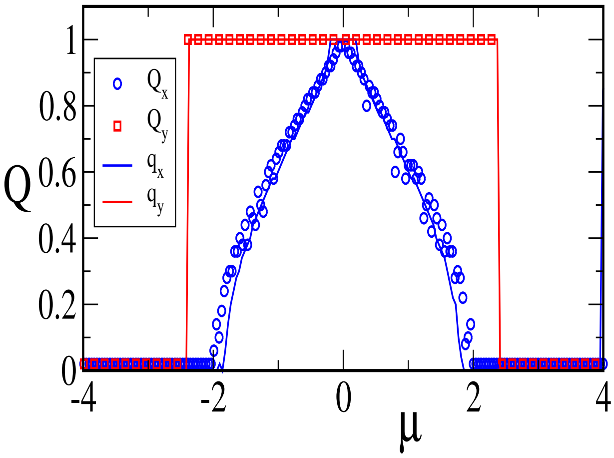

Figure 6.2: The variation of $\chi_0(\mathbf{q}, n)$ is plotted for two dimensional KLM in 2D for a $\sim 200^2$ **k** point grid. The ordering wavevector **Q** from the variational calculation is plotted with open circles for comparison.

grid point. This illustrate the accuracy of $\chi_0(\mathbf{q}, n)$ and $\mathbf{Q}(n)$ with line and small circles respectively. We have taken $Q_y$ as $0$ and $\pi$ only to avoid inaccuracy between $\mathbf{q} = \{0, 0\}$ and $\mathbf{q} = \{0, q\}$ [121], while $Q_x$ scans all values from $0$ to $\pi$ in steps small wave vector and looks continuous due large system size. With increase in the $\mu$ value, $Q_y$ goes from $0$ to $\pi$ for the same $\mu$ value where maximum value of $\chi_0(\mathbf{q}, n)$ is shifted to $\{0, \pi\}$ rather than $\{0, 0\}$. Similarly there is quite good match between $Q_x$ and $\chi_0(\mathbf{q})$ as $\mu$ increases up to $0$. Right hand side is same due to particle-hole symmetry model.

There is no phase separation, *i.e*, discontinuities in $n(\mu)$, for $J_H/t \to 0$ since the $\mu - n$ relation is that of the underlying tight binding system and free of any singularity. The phase transitions with changing $n$ are all *second order*. With growing $J_H/t$, however, some phase boundaries become first order and regimes of PS will emerge.

**(ii)** *Strong coupling:* For $J_H/t \to \infty$, it makes sense to quantise the fermion spin at site $\mathbf{R}_i$ in the direction of the core spin $\mathbf{S}_i$, and project out the 'high energy' unfavourable state. This leads to an effective spinless fermion problem whose bandwidth is controlled by the average spin overlap $\langle \mathbf{S}_i . \mathbf{S}_j \rangle$ between neighbouring sites. The overlap is largest for a fully polarised state, and the FM turns out to be the ground state at all $n \neq 1$. At $n = 1$ 'real hopping' is forbidden so the fermions prefer a G type AFM background to gain kinetic energy $\mathcal{O}(t^2/J_H)$ via virtual hops.

The FM and G type AFM have a first order transition between them with a window of phase separation, easily estimated at large $J_H/t$. The fully polarised FM phase has a density of states (DOS) which is simply two 3D tight binding DOS with splitting $J_H$ between the band centers. If we denote this DOS as $N_{FM}(\omega, J_H)$ then the energy of the FM phase is $\mathcal{E}_{FM}(\mu, J_H) = \int_{-\infty}^{\mu} N_{FM}(\omega, J_H)\omega d\omega$, and the particle density is $n(\mu, J_H) = \int_{-\infty}^{\mu} N_{FM}(\omega, J_H) d\omega$. There will be corresponding expressions when we consider electrons in the $\{\pi, \pi, \pi\}$ AFM background, with DOS $N_{AFM}(\omega, J_H)$. Once we know $\mu = \mu_{AFM}^{FM}$ that satisfies $\mathcal{E}_{FM}(\mu, J_H) = \mathcal{E}_{AFM}(\mu, J_H)$ we can determine the PS window from the density equations. Since the FM phase has a dispersion $\epsilon_{\mathbf{k}}^{FM} = \epsilon_{0,\mathbf{k}} \pm J_H/2$, where $\epsilon_{0,\mathbf{k}} = -2t(cosk_x a + cosk_y a + cosk_z a)$, and the AFM phase has dispersion $\epsilon_{\mathbf{k}}^{AFM} = \pm\sqrt{\epsilon_{0,\mathbf{k}}^2 + (J_H/2)^2}$, it is elementary to work out $\mu_{AFM}^{FM}$. The analysis can be extended to several competing phases. It is significant that even at $J_H/t = 10$, which might occur for strong Hunds coupling in some materials, the FM phase occurs only between $n = \{0, 0.7\}$.

**(iii)** *Intermediate coupling:* The intermediate coupling regime is where one is outside the RKKY window, but not so large a coupling that only the FM and G type AFM are possible. Towards the weak coupling end it implies that the planar spirals begin to pick up a net magnetisation, $\alpha$, and now become 'conical' phases. Windows of phase separation also appear, particularly prominent between the $\{Q_x, \pi, \pi\}$ and G type AFM (near $n = 1$), and suggest the possibility of inhomogeneous states, *etc*, in the presence of disorder. The prime signature of 'physics beyond RKKY', however, is that the RKKY planar spirals now pick up a net magnetisation and much of the phase diagram starts to evolve towards the ferromagnetic state.

## 6.4 Impact of particle-hole asymmetry

Till now we have looked at the particle-hole symmetric case where $t' = 0$. The tight-binding parametrisation of the *ab initio* electronic structure of any material usually requires a finite $t'$, in addition, possibly, to multiple bands. We will use the $t - t'$ parametrisation of band structure due to its simplicity. It will also allow us to mimic the physics in the $4f$ metals.

The results of the variational calculation in the 'asymmetric' ($t' = 0.1$ and $t' = 0.2$) case are shown in Fig-6.3. We employed a grid with upto $40^3$ **k** points, and have checked stability with respect to grid size like that in symmetric case. For electron

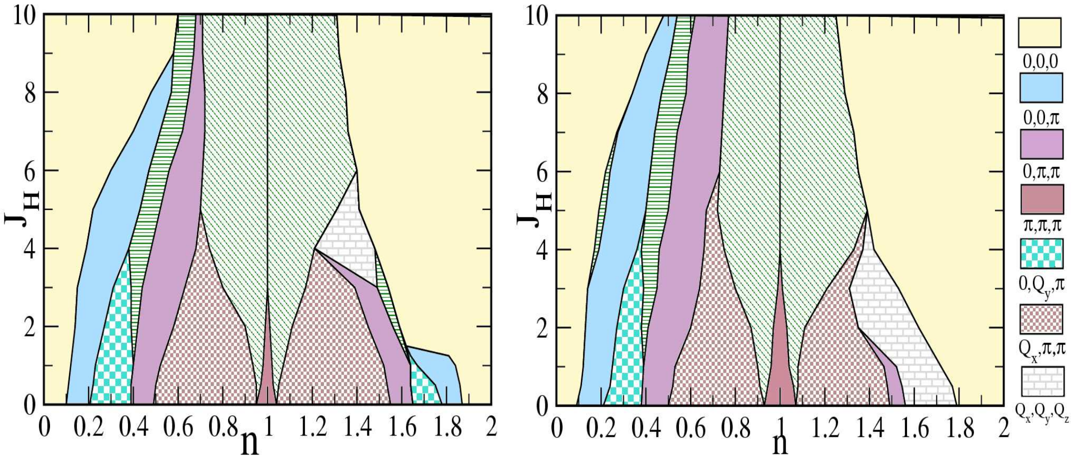

Figure 6.3: Magnetic ground state for the particle-hole asymmetric model ($t' = 0.1$ and $t' = 0.2$) for varying electron density $(n)$ and electron-spin coupling $(J_H)$. Phases are described as in Fig-6.1 with same colour code. Apart from ordering wavevectors $\mathbf{Q} = \{0, Q_y, \pi\}$ and $\mathbf{Q} = \{Q_x, \pi\, \pi\}$ in the incommensurate phases, we have $\mathbf{Q} = Q_x, Q_y, Q_z$ with all components different from $0$ and $\pi$ The results in this figure are based on a variational calculation using a $20^3$ $\mathbf{k}$ point grid, and cross-checked with data on $40^3$.

density less than one, all the phases are present like that in symmetric model. In symmetric model, we have only ferromagnetic phase for electron density less than 0.7 and G-AFM phase at $n = 1$ for $J_H = 10$. With $t'$, spiral phases are found even for $J_H = 10$ or above $J_H = 10$ depending on the value of $t'$. Incontrast, in the electron density range more than 1, only FM phase found for $J_H = 5$ or even below $J_H = 5$. Spiral phase found in low coupling limit for electron density more than 1. So depending on the nearest neighbour interaction, the phase changes in all three coupling limit as compare to $t' = 0$.

At weak coupling the magnetic order is controlled as usual by the band susceptibility, $\chi_0(\mathbf{q}, n)$ which, now, also depends on $t'$. At fixed $n$ the magnetic order can change simply due to changes in the underlying electronic structure. Our Fig-6.4 illustrates this dependence, where we use $J_H = 0.5$ to stay in the RKKY regime and explore the variation of magnetic order with $n$ and $t'$. The range of $t'$ variation is modest, $\sim \{0 - 0.3\}$, but can lead to phase changes (at fixed $n$) in some density windows. We have cross checked the phases with the peak in $\chi_0(\mathbf{q})$.

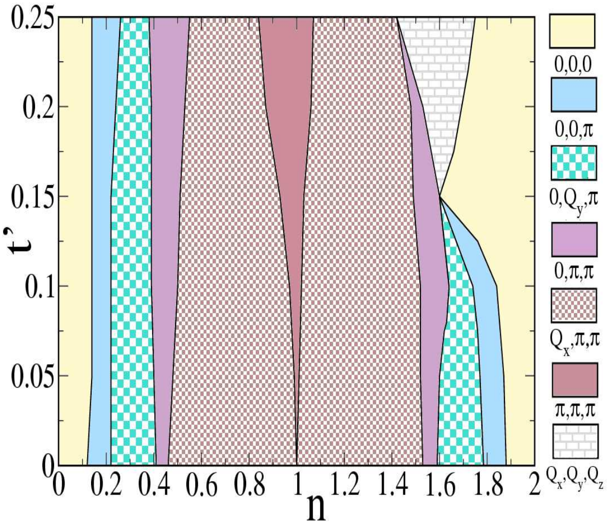

Figure 6.4: The magnetic ground state in the RKKY limit, showing the dependence of the ordering wavevector **Q** on electron density and particle-hole asymmetry (via $t'$). The legend for the various states is shown on the right. The calculations were done at weak coupling, $J_H = 0.5$. Note the growing asymmetry of the phases (about $n = 1$) as $t'$ increases. It is also clear that if the hopping parameter $t'$ changes (due to pressure, *etc.*) the magnetic ground state can change even if the electron density remains fixed, as discussed for $4f$ systems in [122]. This is particularly prominent in the top right hand corner of the figure. In constructing this phase diagram we have ignored a narrow sliver of phase separation near $n = 1$.

## 6.5 Revisiting the $4f$ metals

A complicated and more realistic version of this has been demonstrated recently [122] in the $4f$ family for the heavy rare earths from Gd to Tm. These elements all have the same hcp crystal structure, and the same conduction electron count, $5d^1 6s^2$, so nominally the same band filling. However, the electronic structure and Fermi surface changes due to variation in the lattice parameters and unit cell volume (lanthanide contraction) across the series. It has been argued [122] that this changes the location $\mathbf{q}_{max}$ of the peak in $\chi_0$, and explains the change in magnetic order from planar spiral (in Tm) to ferromagnetism in Gd. A similar effect is visible in our Fig-6.4 where at $n = 1.7$, say, the ordering wavevector changes from a spiral to FM as $t'$ changes from zero to $0.15$. In this scenario, $J_H$ does not affect the magnetic order but merely sets the scale for $T_c$. The RKKY interaction strength scales as $J_{eff}^2 \sim J_H^2 S(S+1)$, and a similar scaling of the experimentally measured $T_c$ is taken as ‘confirmation’ of the RKKY picture.

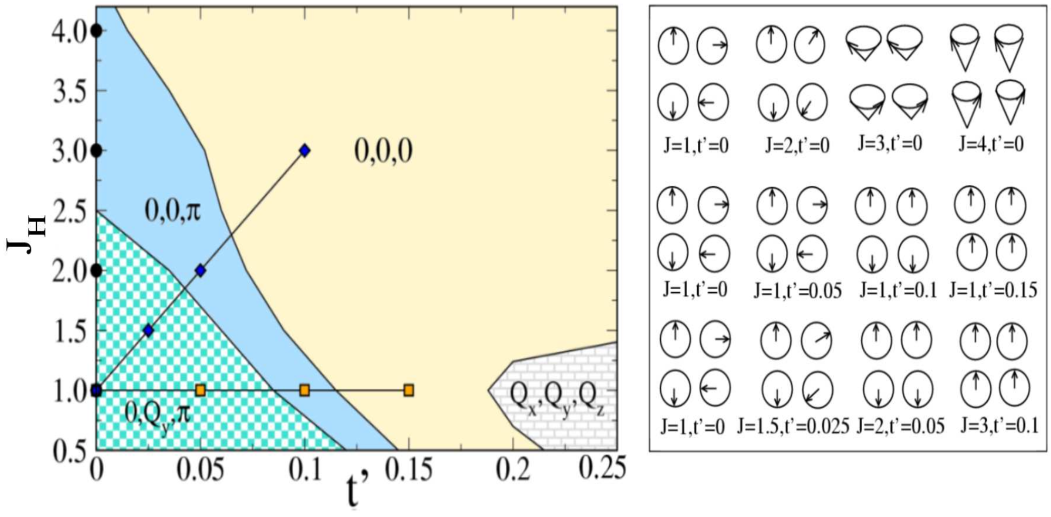

Figure 6.5: **Left:** the magnetic ground state at $n = 1.7$ for varying $t'$ and $J_H$. The ordering wavevector is marked on the phases. The magnetic order has a pronounced dependence on *both* the 'bandstructure' (through $t'$) and the electron-spin coupling. We highlight three kinds of parameter variation. (i) Varying $J_H$ at fixed $t'$, the points on the $y$ axis, shows how changing electron-spin coupling can change the ground state. (ii) Varying $t'$ at weak coupling, $J_H = 1$, illustrates how bandstructure affects the RKKY magnetic order. (iii) In the $4f$ elements we think what happens is a combination of (i) and (ii) above, as shown by points on the diagonal. **Right:** An impression of the real space spin configuration for the three parameter sets (i)-(iii) in the top panel. Each $2 \times 2$ pattern is for a $t'$, $J_H$ combination. The bottom left spin in each pattern is set on the reference site $\mathbf{R} = \{0, 0\}$, say. The neighbouring three spins are at $\{\hat{x}, 0\}$, $\{0, \hat{y}\}$, and at $\{\hat{x}, \hat{y}\}$, where $\hat{x}$ and $\hat{y}$ are unit vectors on the lattice. There is no variation in the $z$ direction so we only show the in-plane pattern. Top row: scan (i) above, changing $J_H$ at $t' = 0$. Middle row: scan (ii), changing $t'$ at $J_H = 1$. Bottom row: scan (iii), simultaneous change in $t'$ and $J_H$.

Should we not also worry about the effect of the growing $J_{eff}(S)$ on the *magnetic order itself*? If the maximum $J_{eff}$, for Gd with $S = 7/2$, were smaller than the effective hopping scale $t$, then we need not - the RKKY scheme would be valid for the entire $4f$ family. However, measurements and electronic structure calculations [106] in Gd suggest that $J_H \sim 0.3$eV and $J_{eff}(7/2) \sim 1$eV. The effective $t$ is more ambiguous, since there are multiple bands crossing the Fermi level, but the typical value is $\sim 0.3$eV. This suggests $J_{eff}/t \sim 3$, clearly outside the RKKY window! What is the consequence for magnetic order, and physical properties as a whole?

Fig-6.5 shows the $t' - J_H$ magnetic phase diagram at $T = 0$ for $n = 1.7$. At $t' = 0$,

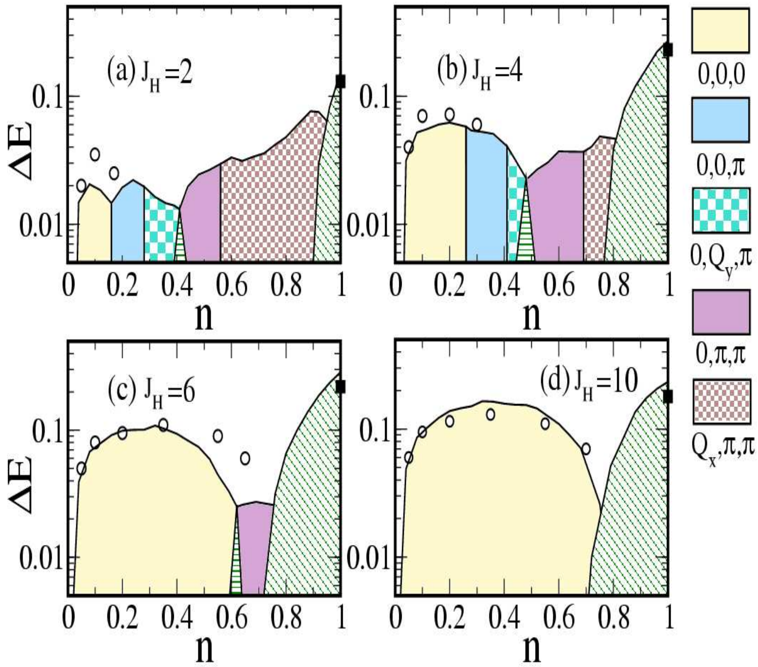

Figure 6.6: The finite temperature phase diagram in the particle-hole symmetric case, for various $J_H$. Panels (a)-(d) show the different ordered phases and their estimated transition temperature as we move from the weak coupling to the double exchange limit. The legend for the phases is shown on the right. The transition temperatures are based either on Monte Carlo results (shown as symbols), or the $\Delta\mathcal{E}$ estimate (firm lines) described in the text. Notice that the $T_c$ for the ferromagnetic, $\mathbf{Q} = \{0,0,0\}$, phase increases (and saturates) with increasing $J_H$. At $n = 1$ the order is at $\mathbf{Q} = \{\pi,\pi,\pi\}$ and the corresponding $T_c$ initially increases with increasing $J_H$ and then decreases. Except for $\mathbf{Q} = \{0,0,0\}$ and $\{\pi,\pi,\pi\}$ other phases vanish by the time $J_H/t = 10$. The Monte Carlo estimate of ferromagnetic $T_c$ are shown as circles, while that of the antiferromagnet is marked on the $n = 1$ axis by a square symbol.

the *vertical* scan, changing $J_H$ reveals how the ordered state changes with increasing $J_H$ even with electronic parameters (and hence $\chi_0$ and FS) fixed. We have already seen this in Fig-6.1. The spirit of RKKY is to assume $J_H \to 0$, and move *horizontally*, changing $t'$ across the series so that one evolves from a planar spiral to a ferromagnet. We suggest that in the $f$ metals, the parameter points are actually on a 'diagonal', with increasing $t'$ (our version of changing electronic structure) being accompanied by increase in $J_{eff}$. To capture the trend we set, $t' = 0$ and $J_{eff} = 1.0$ for $S = 1$, where the system is known to be a spiral, and $t' = 0.1$ and $J_{eff} = 3.0$ for $S = 7/2$ (the case of Gd), and explore the linear variation shown in Fig-6.5. This parametrisation is only meant to highlight the qualitative effect of changing electronic structure and $J_{eff}$ and since real $t'$ values, *etc*, would need to be calculated from an *ab initio* solution.

Within this framework, while the small $S$ result is same for both RKKY and explicit inclusion of $J_{eff}$, the order obtained at intermediate $S$ depends on whether one ignores $J_{eff}$ (as in RKKY) or retains its effect. For a given $t'$ the phase on the diagonal is quite different from the phase on the horizontal line.

In fact there is evidence from earlier *ab initio* calculations [123] that in addition to unit cell volume and $c/a$ ratio, *the strength of the* $4f$ *moment* (and so $J_{eff}$) also affects the magnetic order. As an illustrative case, the optimal spiral wavevector in Ho evolves towards $\mathbf{Q} = \{0, 0, 0\}$ as the effective moment is (artificially) varied from $2\mu_B$ to $4\mu_B$ (Fig-2 in Nordstrom and Mavromaras [123]). If magnetism in this element, and the $4f$ family in general, were completely determined by RKKY there would be *no dependence on* $J_{eff}$. In fact the authors suggested that one should re-examine the basic assumptions of the 'standard model' of $4f$ magnetism [109], which gives primacy to the RKKY interaction (and magnetoelastic effects) since the *ab initio* results suggest a role for the effective exchange in the magnetic order. Our aim here has been to clarify the physics underlying such an effect within a minimal model Hamiltonian. This approach would be useful to handle non collinear phases in complex many band systems, *without any weak coupling assumption*, once a tight binding parametrisation is available

## 6.6 Finite temperature phase diagram

The TCA based MC readily captures the FM and $\{\pi, \pi, \pi\}$ AFM phases at all coupling. However, it has difficulty in capturing the more complex spiral, A, and C type phases when we 'cool' from the paramagnetic phase. In the intermediate $J_H$ regime it usually yields a 'glassy' phase with the structure factor having weight distributed over all **q**. In our understanding this is a limitation of the small cluster based TCA, and the energies yielded by VC are better than that of 'unordered' states obtained via MC. To get a feel for the ordering temperature we have calculated the energy difference $\Delta\mathcal{E}$, defined earlier, as often done in electronic structure calculations. This provides the trend in $T_c$ across the phases, Fig-6.6, and wherever possible we have included data about actual $T_c$ (symbols) obtained from the MC calculation. Broadly, with increasing $J_H$ the $\Delta\mathcal{E}$

and $T_c$ scales increase but the number of phases decrease. The $T_c$ of the G type AFM is expected to fall at large $J_H$ but even at $J_H/t = 10$ it is larger than the peak FM $T_c$.

## 6.7 Conclusions

We have examined the Kondo lattice model with large $S$ spins and established the ground state all the way from the RKKY regime to the strong coupling limit. The intermediate coupling window reveals a competition between RKKY effects, which tend to generate a planar spiral, and the tendency to gain exchange energy via ferromagnetic polarisation. This generally leads to a 'conical' helix, giving way at strong coupling to the double exchange ferromagnet. Using these results we re-visited the classic $4f$ magnets to demonstrate how the magnetic phases there are probably controlled non RKKY spin-fermion effects. One can add anisotropies and magneto-elastic couplings to our model to construct a more comprehensive description of $4f$ magnetism.

# Chapter 7

# Conclusions

Disorder is recognised as a key player in the manganites. In the doped manganites, $A_{1-x}A'_xMnO_3$, 'A site' disorder seems to affect the physical properties through several mechanisms: (i) In a regime of possible phase separation, disorder, along with Coulomb interaction, promotes a cluster coexistence state. If the A site disorder is large the resulting state is just a nanoscale correlated glass. (ii) In the low bandwidth manganites, with large electron-phonon (EP) interaction, disorder promotes polaron formation, strongly enhancing the resistivity in the metallic state, and suppresses the ordering temperature.

We discuss both A and B site disorder, but the focus is mainly on B site doping, classifying the wide variety of results in terms of the reference manganite state and the valence and magnetic character of the dopant. The impact of 'B site' (Mn site) dopants, *i.e*, materials of the form $A_{1-x}A'_xMn_{1-\eta}B_\eta O_3$, present several puzzles. For example, a low density (a few %) of B dopants can convert an insulator to a metal or a metal to an insulator, simultaneously affecting the underlying magnetic state.

There are a variety of striking but apparently unconnected results on B doping in the manganites. For example, magnetic dopants like Cr, Co or Ni (but not Fe) on the Mn site in a $x = 0.5$ charge ordered insulating (CO-I) manganite promote a percolative ferromagnetic metal (FM-M), while non magnetic dopants of the same valence do not. The orbital ordered A type antiferromagnet (AF) at $x = 0$ is destabilised in favour of a ferromagnetic state by *both* magnetic and non magnetic dopants. In contrast to the cases above, where charge-orbital order is *suppressed*, doping Fe on a ferromagnetic metal at $x \sim 0.4$ *promotes* a charge ordered insulating state! This promotion of a competing ordered phases has no equivalent in the case of A site disorder. On spatial imaging most of these systems reveal phase separation (PS) and many of them also exhibit enormous magnetoresistance. The work in this thesis uncovers the organising principle behind these diverse effects, and suggest how B site disorder could be exploited as a tool for electronic phase control.

The problem above includes multiple strong couplings in the reference manganite model, to capture the phase competition, and the presence of dilute strong scatterers on some Mn sites. We use the 'travelling cluster' (TCA) variant of exact diagonalisation based Monte Carlo to solve this problem.

We provide an overview of the manganites in Chapter.1 and follow it with an experimental survey in Chapter.2. This is followed in Chapter.3 by a discussion of our results on the impact of weak homogeneous (A site) disorder and strong dilute (B site) scattering on the $x = 0.5$ CE charge ordered manganites is first of its kind. We use a suitable 'reference' model for the clean manganite - involving $e_g$ electron hopping, Hunds and Jahn-Teller coupling, and weak antiferromagnetic superexchange between the Mn $t_{2g}$ spins. The modelling of B site disorder in this effort is crude, incorporating only a strong repulsive potential, but leads to results which capture (one family of) key experimental effects, including the percolative metallisation of the CE insulator.

In Chapter.4 we considered a more 'realistic' but still minimal model of B dopants in the manganites. The impurities are modelled in terms of their valence in the manganite, the position of the impurity level with respect to the manganese $e_g$ levels, and the exchange and hopping interactions between the dopant and neighbouring Mn atoms. The principal parameters in the problem are hole doping $x$, the manganite bandwidth, mimicked by the ratio of hopping and Jahn-Teller coupling in our theory, and the impurity valence $\alpha$ and concentration $\eta$. The impurity potential $(V)$ and exchange coupling $(J')$ to Mn, for magnetic dopants, are also relevant in some cases.

Our results are described in two chapters, the first focusing on situations where valence change on Mn due to B impurities is the key effect, while the second studies the impact of magnetic dopants. Our principal results are the following: **(i)** We discover that the following hierarchy of effects arise in all B doping cases: (a) change of the effective valence on the Mn sites, (b) percolation of the metallic phase through impurity free regions, and (c) 'reconstruction' of the background magnetism and charge order

---

by magnetic dopants. **(ii)** By exploring the prominent manganite states, and different B dopants, we are able to explain most of the outstanding experimental results.

# Appendix 1 (Travelling Cluster Approximation)

The finite size real space approach uses the Metropolis algorithm to generate equilibrium configurations of the spins at a given temperature. Monte Carlo calculations on classical systems with short range interactions involve a cost $\mathcal{O}(zN)$ for a system update, with z being the coordination number on the lattice and N the system size. In the spin-fermion problem, however, the cost of a spin update at a site has to be computed from the fermion free energy. If one uses direct exact diagonalisation (ED) of the Hamiltonian to accomplish this, the cost per site is $\mathcal{O}(N^3)$, the cost for a system update is a prohibitive $N^4$.

The annealing of the classical variables (spin and phonon) is done by choosing a random spin-phonon background at high temperature. At each temperature, one needs to anneal the system sufficiently, at least larger than 2000 system sweeps, by visiting every site of the lattice sequentially and update the system using metropolis algorithm. For each system sweep the cost of computation is $\mathcal{O}(N^4)$ and adding to that 1000's of system sweep to anneal the system at various temperature is really a tedious job.

In a 2-dimensional square lattice $L \times L$ ($N = 2L^2$, 2 comes from the fact that we have two states at each site) in real space with periodic boundary conditions, computational cost is $\mathcal{O}(N^4)$ for each system sweep. The traditional ED montecarlo (ED-MC) allows us to access small cluster size up to $\sim 10^2$.

However, Kumar *et al.* [97] developed a moving cluster method which takes into account each and every step one usually do in ED-MC but employed smartly to update spin-phonon variables without diagonalizing the full Hamiltonian. The method is as follows: In original ED-MC, one need to diagonalise the full system every time one updates a spin and/or phonon variable. But the same update can be done using

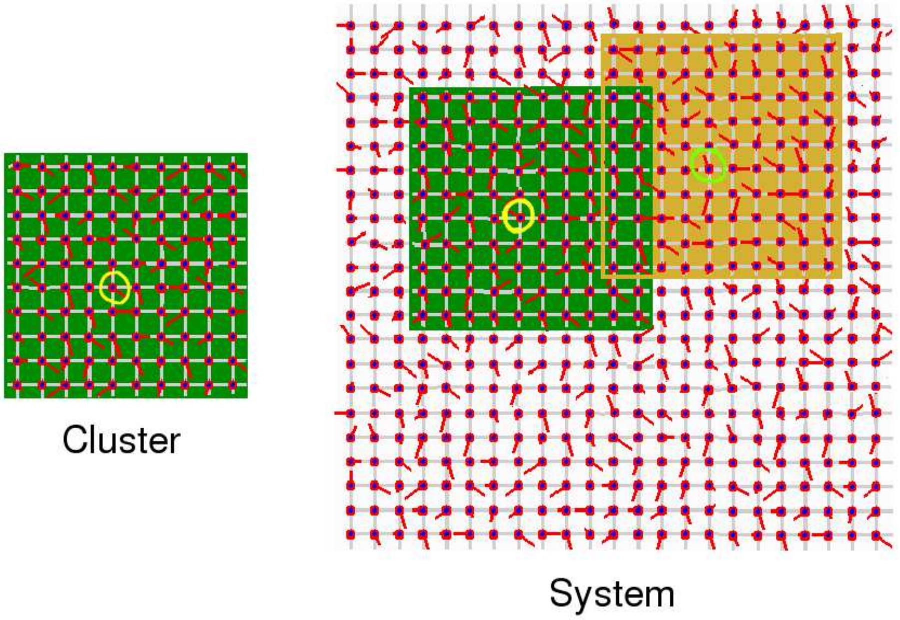

Figure 7.1: A schematic to show the Travelling Cluster Approximation. When we update spin and/or phonon at a site, we construct a cluster of size $L_c$ in a L size lattice and update our site by diagonalising the cluster of size $L_c$.

choosing an area sorrounding the site to be updated (see Fig-7.1), lets say a square of size $L_c$ (less than L). This reduces the size of the Hamiltonian to diagonalise for each update but comes with a fact that for each site to be updated, one needs to construct a Hamiltonian of the $L_c^2$ around it. Computational cost decreases to $\mathcal{O}(NN_c^3)$ and allow us to calculate system sizes upto $40^2$, when we employed a moving cluster of size $8^2$. The method is well benchmarked by the authors.

# Appendix 2 (Conductivity Calculation)

We pursue the Kubo approach, indirectly, through a calculation of the low frequency optical conductivity. The advantage of calculating the conductivity in this way is, $(i)$ it ties in with diagonalisation that one may have to do for the magnetic problem, and $(ii)$ it allows access to the optical conductivity, without added effort, and can reveal the significantly non Drude nature of $\sigma(\omega)$ at strong disorder.

For disordered non interacting systems, the Kubo formula, at $T = 0$, is:

$$\sigma(\omega) = \frac{A}{N} \sum_{\alpha,\beta} (n_\alpha - n_\beta) \frac{|f_{\alpha\beta}|^2}{\epsilon_\beta - \epsilon_\alpha} \delta(\omega - (\epsilon_\beta - \epsilon_\alpha)),$$

with $A = \pi e^2/\hbar a_0$, $a_0$ being the lattice spacing, and $n_\alpha = \theta(\mu - \epsilon_\alpha)$. $f_{\alpha\beta}$ are matrix elements of the current operator $j_x = it \sum_{i,\sigma}(c^\dagger_{i+xa_0,\sigma} c_{i,\sigma} - h.c)$, between exact single particle eigenstates $|\psi_\alpha\rangle$, $|\psi_\beta\rangle$, *etc*, and $\epsilon_\alpha$, $\epsilon_\beta$ are the corresponding eigenvalues.

The conductivity above is prior to disorder averaging. Notice that the $\delta$ function constraint cannot be satisfied for arbitrary frequency in a finite system. So we can neither calculate the d.c. conductivity, $\sigma_{dc}$, directly, nor estimate $\sigma(\omega)$ at some arbitrary externally specified frequency. However, we can still calculate the 'average' conductivity over a frequency interval $\Delta\omega$, defined below, and we use the following strategy to extract $\sigma_{dc}$.

The average of $\sigma(\omega)$ over the interval $[0, \Delta\omega]$ is defined as

$$\sigma_{av}(\Delta\omega, \mu, N) = \frac{1}{\Delta\omega} \int_0^{\Delta\omega} \sigma(\omega, \mu, N) d\omega$$

$\Delta\omega$ can be set independent of $N$, but we will relate them by fixing: $\Delta\omega = BW/N$ where BW is the bandwidth. We fix $BW$ by setting $\Delta\omega = 0.04$ for $N = 1000$. The mean finite size gap is $8/1000 \sim 0.01$, in 2 dimension, much smaller than $\Delta\omega$. $\sigma_{av}$ is thermal averaged over 500 times in each temperature. Addition to that we have taken minimum 10 copies of disorder realisation as we do A site or B site disorder.

We calculate conductivity for 24×24 lattice size. We show many results which are disordered assisted metal in low temperature. Our disordered metal would indeed show weak localization but at very large L×L as compare to 24 ×24 used in our calculations.

# Appendix 3 (Physical Quantities Calculation)

We track various physical quantities in real space and momentum space which provide information about the correlations of (and between) the various degrees of freedom of the system. Here we briefly discuss these indicators. These are further backed up with real space snapshots of the lattice.

We compute the 'one point' distribution of lattice distortions, $P(Q) = \sum_i \delta(Q - Q_i)$, where $Q_i = |\mathbf{Q}_i|$, spatial $Q-Q$ correlations $D_Q(\mathbf{q}) = \sum_{ij} \langle \mathbf{Q}_i \mathbf{Q}_j \rangle e^{i\mathbf{q}\cdot(\mathbf{r}_i - \mathbf{r}_j)}$, and spin-spin correlations $S(\mathbf{q}) = \sum_{ij} \langle \mathbf{S}_i . \mathbf{S}_j \rangle e^{i\mathbf{q}\cdot(\mathbf{r}_i - \mathbf{r}_j)}$. Here angular bracket represent thermal average. Further, the spatial snapshots also directly provide visual information on the various phases. While the indicators above measure the correlations and spatial evolution, the metallic or insulating character is tracked via (low frequency) conductivity [118] (see Appendix 2), $\sigma_{dc}$, and the density of states (DOS), $N(\omega) = \langle \frac{1}{N} \sum_n \delta(\omega - \epsilon_n) \rangle$, where $\epsilon_n$ are the electronic eigenvalues in some background in the MC.

# Bibliography

[1] Masatoshi Imada, Atsushi Fujimori, and Y. Tokura, Rev. Mod. Phys. **70**, 1039 (1998).

[2] E. Dagotto, Rev. Mod. Phys. **66**, 763 (1994).

[3] Myron B. Salamon, and Marcelo Jaime, Rev. Mod. Phys. **73**, 583 (2001).

[4] H. Alloul, J. Bobroff, M. Gabay, and P. J. Hirschfeld, Rev. Mod. Phys. **81**, 45 (2009).

[5] *Colossal Magnetoresistive Oxides*, edited by Y. Tokura (Gordon and Breach, New York, 2000).

[6] Y. Tokura, Rep. Prog. Phys. **69**, 797 (2006).

[7] *Colossal Magnetoresistive Manganites*, edited by T. Chatterji (Springer 2004).

[8] S. Jin, T. H. Tiefel, M. McCormack, R.A. Fastnacht, R. Ramesh, and L.H. Chen, Science **264**, 413 (1994).

[9] M. N. Baibich, J. M. Broto, A. Fert, F. Nguyen Van Dau, F. Petroff, P. Etienne, G. Creuzet, A. Friederich, and J. Chazelas, Phys. Rev. Lett. **61**, 2472 (1988).

[10] G. Binasch, P. Grunberg, F. Saurenbach, and W. Zinn, Phys. Rev. **B 39**, 4828 (1989).

[11] J. H. van Santen and G. H. Jonker, Physica **16**, 599 (1950).

[12] G. H. Jonker and J. H. van Santen, Physica **16**, 337 (1950).

[13] C. Zener, Phys. Rev. **82**, 403 (1951).

[14] J. Volger, Physica **20**, 49 (1954).

[15] R von Helmoltz, J. Wecker, B. Holzapfel, L. Schultz and K. Samwer, Phys. Rev. Lett. **71**, 2331 (1993).

[16] G. C. Xiong, Q. Li, H. L. Ju, S. M.Bhagat, S. E. Lofland, R. L. Green, and T. Venkatesan, Appl. Phys. Lett. **67**, 3031, (1995).

[17] A. J. Millis, P. B. Littlewood, and B. I. Shraiman, Phys. Rev. Lett. **74**, 5144 (1995).

[18] A. Urushibara, Y. Moritomo, T. Arima, A. Asamitsu, G. Kido, and Y. Tokura, Phys. Rev. **B 51**, 14103 (1995).

[19] V. M. Goldschmidt, *Goechemistry*, Oxford University Press (1958).

[20] R. D. Shannon and C. T. Prewitt, Acta Crystallogr. **B 25**, 725 (1969).

[21] W. E. Pickett and D. J. Singh, Phys. Rev. **B 53**, 1146 (1996).

[22] H. A. Jahn and E. Teller, Proc. Roy. Soc. London A **161**, 220 (1937).

[23] P. W. Anderson and H. Hasegawa, Phys. Rev. *ibid.* **100**, 675 (1955).

[24] P. G. de Gennes, *ibid.* **118**, 141 (1960).

[25] A. J. Millis, B. I. Shraiman, and R. Mueller, Phys. Rev. Lett. **77**, 175 (1996).

[26] C. P. Adams, J. W. Lynn, Y. M. Mukovskii, A. A. Arsenov, and D. A. Shulyatev, Phys. Rev. Lett. **85**, 3954 (2000).

[27] J. Kanamori, J. Appl. Phys. Suppl. **31**, 14S (1960).

[28] T. Mizokawa, D. I. Khomskii, and G. A. Sawatzky, Phys. Rev. **B 60**, 7309 (1999).

[29] Y. Yamada, Y. Hino, S. Nohdo, R. Kanao, T. Inami, and S. Katano, Phys. Rev. Lett. **77**, 904 (1996).

[30] F. Moussa, M. Hennion, F. Wang, P. Kober, J. Rodriguez-Carvajal, P. Reutler, L. Pinsard, and A. Revcolevschi, Phys. Rev. **B 67**, 214430 (2003).

[31] R. Kajimoto, H. Yoshizawa, Y. Tomioka, and Y. Tokura, Phys. Rev. **B 66**, 180402 (2002).

[32] Indu Dhiman, A. Das, P. K. Mishra, and L. Panicker, Phys. Rev. **B 77**, 094440 (2008).

[33] R. Mallik, E. S. Reddy, P. L. Paulose, S. Majumdar, and E. V. Sampathkumaran, J. Phys.: Condens. Matter **11**, 4179 (1999).

[34] E. O. Wollan, and W. C. Koehler, Phys. Rev. **100**, 545 (1955).

[35] M. Uehara, S. Mori, C. H. Chen, and S. W. Cheong, Nature **399**, 560 (1999).

[36] Liuwan Zhang, Casey Israel, Amlan Biswas, R. L. Greene, Alex de Lozann, Science **298**, 805 (2002).

[37] M. Fath, S. Freisem, A. A. Menovsky, Y. Tomioka, J. Aarts, J. A. Mydosh, Science **285**, 1540 (1999).

[38] A. M. Balagurov, V. Yu. Pomjakushin, D. V. Sheptyakov, V. L. Aksenov, N. A. Babushkina, L. M. Belova, A. N. Taldenkov, A. V. Inyushkin, P. Fischer, M. Gutmann, I. Keller, O. Yu. Gorbenko, and A. R. Kaul, Phys. Rev. **B 60**, 383 (1999).

[39] A. M. Balagurov, V. Yu. Pomjakushin, D. V. Sheptyakov, V. L. Aksenov, P. Fischer, L. Keller, O.Yu. Gorbenko, A.R. Kaul, and N.A. Babushkina, Phys. Rev. **B 64**, 024420 (2001).

[40] P. Woodward, D. Cox, T. Vogt, and A. Cheetham, Chem. Mater. **11**, 3528 (1999).

[41] C. Ritter, R. Mahendiran, M. Ibarra, B. Morellon, A. ans Raveau, and C. Rao, Physical Review **B 61**, R9229 (2000).

[42] M. N. Iliev, M. V. Abrashev, H. G. Lee, Y. Y. Sun, C. Thomsen, R. L. Meng, and C. W. Chu, Phys. Rev. **B 57**, 2872 (1998).

[43] Z. Popovic and S. Satpathy, Phys. Rev. Lett. **88**, 197201 (2002).

[44] Y. Okimoto, T. Katsufuji, T. Ishikawa, A. Urushibara, T. Arima, and Y. Tokura, Phys. Rev. Lett. **75**, 109 (1995).

[45] A. Machida, Y. Moritomo, and A. Nakamura, Phys. Rev. **B 58**, R4281 (1998).

[46] J. H. Park, C. T. Chen, S. W. Cheong, W. Bao, G. Meigs, V. Chakarian, and Y. U. Idzerda, Phys. Rev. Lett. **76**, 4215 (1996).

[47] T. G. Perring, G. Aeppli, Y. Moritomo, and Y. Tokura, Phys. Rev. Lett. **78**, 3197 (1997).

[48] R. Maezono, S. Ishihara, and N. Nagaosa, Phys. Rev. **B 58**, 11583 (1998).

[49] H. Y. Hwang, S. W. Cheong, P. G. Radaelli, M. Marezio, and B. Batlogg, Phys. Rev. Lett. **75**, 914 (1995).

[50] L. M. Rodriguez-Martinez and J. P. Attfield, Phys. Rev. **B 54**, R15622 (1996).

[51] L. M. Rodriguez-Martinez and J. P. Attfield, Phys. Rev. **B 58**, 2426 (1998).

[52] L. M. Rodriguez-Martinez and J. P. Attfield, Phys. Rev. **B 63**, 024424 (2001).

[53] J. P. Attfield, Int. J. Inorg. Mater. **3**, 1147 (2001).

[54] G. L. Liu, J. S. Zhou, and J. B. Goodenough, Phys. Rev. B 70, 224421 (2004).

[55] S. Kumar, and P. Majumdar, Phys. Rev. Lett. **96**, 016602 (2006).

[56] Y. Moritomo, A. Machida, S. Mori, N. Yamamoto, and A. Nakamura, Phys. Rev. B **60**, 9220 (1999).

[57] C. H. Chen, S. W. Cheong, and H. Y. Hwang, J. Appl. Phys. **81**, 4326 (1997).

[58] G. C. Milward, M. J. Calderon, and P. B. Littlewood, Nature **433** , 607 (2005).

[59] F. Millange, V. Caignaert, B. Domenges, B. Raveau, and E. Suard, Chem. Mater. **10**, 1974 (1998).

[60] T. Nakajima, H. Kageyama, and Y. Ueda, J. Phys. Chem. Solids **63**, 913 (2002).

[61] B. Raveau, A. Maignan, and C. Martin, J. Solid State Chem. **130**, 162 (1997).

[62] D. Akahoshi, M. Uchida, Y. Tomioka, T. Arima, Y. Matsui, and Y. Tokura, Phys. Rev. Lett. **90**, 177203 (2003).

[63] R. Mathieu, D. Akahoshi, A. Asamitsu, Y. Tomioka, and Y. Tokura, Phys. Rev. Lett. **93**, 227202 (2003).

[64] B. Raveau, S. Hebert, A. Maignan, R. Fresard, M. Hervieu, and D. Khomskii, J. Appl. Phys. **90**, 1297 (2001).

[65] T. Kimura, R. Kumai, Y. Okimoto, and Y. Tomioka, Phys. Rev. B **62**, 15021 (2000).

[66] A. Machida, Y. Moritomo, K. Ohoyama, T. Katsufuji, and A. Nakamura, Phy. Rev. **B 65**, 064435 (2002).

[67] C. Martin, A. Maignan, M. Hervieu, C. Autret, B. Raveau, and D. I. Khomskii, Phy. Rev. **B 63**, 174402 (2001).

[68] K. H. Ahn, X. W. Wu, K. Liu, and C. L. Chien, J. Appl Phys. **81**, 5505 (1997).

[69] A. Maignan, and B. Raveau, Z. Phys. **B 102**, 299 (1997).

[70] H. Sakai, K. Ito, T. Nishiyama, Xiuzhen Yu, Y. Matsui, S. Miyasaka, and Y. Tokura, J. Phys. Soc. Jpn. **77**, 124712 (2008).

[71] H. Sakai, K. Ito, R. Kumai, and Y. Tokura, Phy. Rev. **B 76**, 155112 (2007).

[72] C. Martin, A. Maignan, M. Hervieu, B. Raveau, and J. Hejtmanek, Phys. Rev. **B 63**, 100406 (2001).

[73] J. H. Park, S. W. Cheong, and C. T. Chen, Phys. Rev. **B 55**, 11072(1997).

[74] J. van Elp, Phys. Rev. **B 60**, 7649 (1999).

[75] M. S. Kim, J. B. Yang, Q. Cai, X. D. Zhou, W. J. James, W. B. Yelon, P. E. Parris, D. Buddhikot, and S. K. Malik, Phys. Rev. **B 71**, 014433 (2005).

[76] D. N. H. Nam, L. V. Bau, N. V. Khiem, N. V. Dai, L. V. Hong, N. X. Phuc, R. S. Newrock, and P. Nordblad, Phys. Rev. **B 73**, 184430 (2006).

[77] Sanjeev Kumar, Arno P. Kampf, and Pinaki Majumdar, Phys. Rev. Lett. **97**, 176403 (2006).

[78] Sanjeev Kumar, Arno P. Kampf, and Pinaki Majumdar, Phys. Rev. **B 75**, 014209 (2007).

[79] Sanjeev Kumar and Arno P. Kampf, Phys. Rev. Lett. **100**, 076406 (2008).

[80] Cengiz Sen, Gonzalo Alvarez, Horacio Aliaga, and Elbio Dagotto, Phys. Rev. **B 73**, 224441 (2006).

[81] Cengiz Sen, Gonzalo Alvarez, and Elbio Dagotto, Phys. Rev. Lett. **98**, 127202 (2007).

[82] Yukitoshi Motome and Nobuo Furukawa, Phys. Rev. **B 68**, 144432 (2003).

[83] A. Barnabe, A. Maignan, M. Hervieu, F. Damay, C. Martin, and B. Raveau, Appl. Phys. Lett. **71**, 3907 (1997).

[84] T. Kimura, Y. Tomioka, R. Kumai, Y. Okimoto, and Y. Tokura, Phys. Rev. Lett. **83**, 3940 (1999).

[85] H. Oshima, Y. Ishihara, M. Nakamura, and K. Miyano, Phys. Rev. **B 63**, 094420 (2001).

[86] S. Mori, R. Shoji, N. Yamamoto, T. Asaka, Y. Matsui, A. Machida, Y. Moritomo, and T. Katsufuji, Phys. Rev. **B 67**, 012403 (2003).

[87] E. Dagotto, S. Yunoki, A. L. Malvezzi, A. Moreo, J. Hu, S. Capponi, D. Poilblanc, and N. Furukawa, Phys Rev **B 58** 6414 (1998).

[88] A. C. Green, Phys. Rev. **B 63**, 205110 (2001).

[89] J. van den Brink, G. Khaliullin, and D. Khomskii, Phys. Rev. Lett. **83**, 5118 (1999).

[90] Seiji Yunoki, Takashi Hotta, and Elbio Dagotto, Phys. Rev. Lett. **84**, 3714 (2000).

[91] L. Brey, Phys. Rev. **B 71**, 174426 (2005).

[92] O. Cepas, H. R. Krishnamurthy, and T. V. Ramakrishnan, Phys. Rev. Lett. **94**, 247207 (2005).

[93] S. Dong, S. Dai, X. Y. Yao, K. F. Wang, C. Zhu, and J. M. Liu, Phys. Rev. **B 73**, 104404 (2006).

[94] H. Aliaga, D. Magnoux, A. Moreo, D. Poilblanc, S. Yunoki, and E. Dagotto, Phys. Rev. **B 68**, 104405 (2003).

[95] Y. Motome, N. Furukawa, and N. Nagaosa, Phys. Rev. Lett. **91**, 167204 (2003).

[96] G. Alvarez, H. Aliaga, C. Sen, and E. Dagotto, Phys. Rev. **B 73**, 224426 (2006).

[97] S. Kumar and P. Majumdar, Eur. Phys. J. **B 50**, 571 (2006).

[98] A. Moreo, M. Mayr, A. Feiguin, S. Yunoki, and E. Dagotto, Phys. Rev. Lett. **84**, 5568 (2000).

[99] S. Kumar and P. Majumdar, Phys. Rev. Lett. **92**, 126602 (2004).

[100] F. studer, O. Toulemonde, J. Goedkoop, A. Barnabe, and B. Raveau, Jpn. J. Appl. Phys. **38**, 377 (1999).

[101] S. Fratini, D. Feinberg, and M. Grilli, Eur. Phys. J. **B 22**, 205110 (2001).

[102] Vijay B. Shenoy, Tribikram Gupta, H. R. Krishnamurthy, and T. V. Ramakrishnan, Phys. Rev. Lett. **98**, 097201 (2007).

[103] Takashi Hotta and Elbio Dagotto, Phys. Rev. **B 61**, R11879 (2000).

[104] Y. Moritomo, K. Murakami, H. Ishikawa, M. Hanawa, A. Nakamura, and K. Ohoyama, Phys. Rev. B **69**, 212407 (1999).

[105] A. C. Hewson, *The Kondo Problem to Heavy Fermions*, Cambridge University Press (1997).

[106] C. Santos, and W. Nolting and V. Eyert, Phys. Rev. **B 69**, 214412 (2004).

[107] M. Heinemann and W. M. Temmerman, Phys. Rev. **B 49**, 4348 (1994).

[108] S. Legvold, *Ferromagnetic Materials*, Vol. 1, Chap. 3., (North Holland, Amsterdam, 1980).

[109] J. Jensen and A. K. Mackintosh, *Rare Earth Magnetism*, (Clarendon, Oxford, 1991).

[110] R. J. Elliott, Phys. Rev. **124**, 346 (1961).

[111] T. Jungwirth, J. Sinova, J. Masek, J. Kucera, and A. H. Macdonald, Rev. Mod. Phys. **78**, 809 (2006).

[112] M. A. Ruderman and C. Kittel, Phys. Rev. **96**, 99 (1954), Kasuya, Prog. Theor. Phys. **16**, 45 (1956), K. Yosida, Phys. Rev. **106**, 893 (1957).

[113] M. J. Calderon and L. Brey, Phys. Rev. **B 58**, 3286 (1998).

[114] Y. Motome and N. Furukawa, J. Phys. Soc. Jpn. **69** 3785, (2000).

[115] D. Pekker, S. Mukhopadhyay, N. Trivedi, and P. M. Goldbart, Phys. Rev. **B 72**, 075118 (2005).

[116] A. Chattopadhyay, A. J. Millis, and S. Das Sarma, Phys. Rev. **B 64**, 012416 (2001).

[117] J. Kienert and W. Nolting, Phys. Rev. **B 73**, 224405 (2006).

[118] S. Kumar and P. Majumdar, Eur. Phys. J. **B 46**, 237 (2005).

[119] M. Hamada and H. Shimahara, Phys. Rev. **B 51**, 3027 (1995).

[120] J. L. Alonso, J. A. Capitan, L. A. Fernandez, F. Guinea, and Martin V. Mayor, Phys. Rev. **B 64**, 054408 (2001).

[121] W. E. Evenson and S. H. Liu, Phys. Rev. **178**, 783 (1969).

[122] I. D. Hughes, M. Dane, A. Ernst,W. Hergert, M. Luders, J. Poulter, J. B. Staunton, A. Svane, Z. Szotek, and W. M. Temmerman, Nature **446**, 650 (2007).

[123] L. Nordstrom and A. Mavromaras, Europhys. Lett. **49**, 775 (2000).